Spare

# ESSA Technical Memorandum ERLTM-NHRL 89

**U.S. DEPARTMENT OF COMMERCE**
ENVIRONMENTAL SCIENCE SERVICES ADMINISTRATION
Research Laboratories



## A Diagnostic Model of the Tropical Cyclone in Isentropic Coordinates

RICHARD ALLEN ANTHES

National Hurricane
Research Laboratory
MIAMI, FLORIDA
April 1970

U.S. DEPARTMENT OF COMMERCE
Environmental Science Services Administration
Research Laboratories

ESSA Technical Memorandum ERLTM-NHRL 89

# A DIAGNOSTIC MODEL OF THE TROPICAL CYCLONE IN ISENTROPIC COORDINATES

Richard Allen Anthes



National Hurricane Research Laboratory
Miami, Florida
April 1970

TABLE OF CONTENTS

LIST OF FIGURES

LIST OF TABLES

TABLE OF SYMBOLS

| | |
|---|---|
| $p$ | pressure |
| $p_o$ | reference pressure = 1000 mb |
| $R_d$ | gas constant of dry air |
| $C_p$ | specific heat at constant pressure |
| $\varkappa$ | $R_d/C_p$ |
| $g$ | acceleration of gravity |
| $\sigma$ | area |
| $\theta$ | potential temperature |
| $\Delta\theta$ | vertical grid increment |
| $\theta_e$ | equivalent potential temperature |
| $\theta_o$ | coldest $\theta$ in domain |
| $\theta_t$ | top isentropic surface in model |
| $r$ | radial distance |
| $\Delta r$ | horizontal grid increment |
| $\lambda$ | tangential direction |
| $\mathbf{V}$ | horizontal wind vector |
| $v_\lambda$ | tangential wind component |
| $v_r$ | radial wind component |
| $\Delta t$ | time (iteration) step |
| $z$ | height |
| $j,J$ | horizontal grid index, maximum index |
| $i,I$ | vertical grid index, maximum index |

$( )_s$ subscript s denoting surface, $\sigma=0$

$\overline{( )}$ operator denoting area average

$( )_r$ subscript r denoting reference atmosphere

$\nabla_\theta$ del operator on isentropic surface

$\nabla^2$ operator = $\frac{\partial^2}{\partial r^2} + \frac{1}{r}\frac{\partial}{\partial r}$

$\dot{Q}$ heating rate per unit mass

A available potential energy

k specific kinetic energy = $\frac{1}{2}(v_\lambda^2+v_r^2)$

K total kinetic energy

T absolute temperature

$\Psi$ Montgomery potential = $C_pT + gz$

$R, R_j$ maximum radial distance of domain, horizontal boundary

f Coriolis parameter

$K_H$ horizontal coefficient of eddy viscosity

$K_z$ vertical coefficient of eddy viscosity

$K_T$ horizontal coefficient of thermal diffusion

$C_D$ drag coefficient

$\Delta z$ depth of boundary layer (assumed constant)

$\varsigma$ air density

$q_s$ saturation specific humidity

$T_s$ moist-adiabat temperature

$\omega$ "vertical p velocity" = dp/dt

$\zeta_a$ absolute vorticity

u path length

$\gamma(u)$ transmissivity

R(u) absorptivity

ABSTRACT

A diagnostic axisymmetric model in isentropic coordinates is developed to study the effect of differential heating on the dynamics and energetics of the steady-state tropical cyclone. From the thermal forcing specified by various heating distributions, slowly varying solutions for the mass and momentum fields are obtained by an iterative technique.

The theory of available potential energy for open systems is utilized to study the energy budget for the hurricane. In the slowly varying state, the gain of available potential energy by diabatic heating and lateral boundary processes balances the conversion of potential to kinetic energy which, in turn, offsets frictional dissipation. For a domain of radius 500 km, the boundary flux of available potential energy is about 40 percent of the generation by diabatic heating. For a domain of radius 1000 km, however, the boundary flux is about 15 percent of the generation.

The conversion of available potential to kinetic energy closely follows the generation of available energy as the slowly varying state is reached. This close correlation suggests that changes in the available energy generation result in nearly simultaneous changes in kinetic energy conversion rather than a change in the store of available potential energy.

Horizontal and vertical mixing are studied through the use of constant exchange coefficients. As the internal mixing is decreased, the maximum surface wind increases and moves closer to the center.

Several horizontal and two vertical distributions of latent heating are investigated. The maximum surface wind is dependent primarily on heating within 100 km. The transverse (radial) circulation is closely related to the heat release beyond 100 km. In experiments in which the vertical variation of heating is pseudoadiabatic, the temperature and outflow structures are unrealistic. A vertical distribution which releases a higher proportion of heat in the upper troposphere yields results that are more representative of the hurricane.

The effects of differential cooling by infrared emission are investigated. In one experiment, cooling is computed from 300 to 1000 km from the storm center, a region assumed to be cloud-free. The vertical variation of the cooling profile is determined from several cooling profiles computed using Sasamori's (1968) model for various clear air tropical atmospheres. Cooling in the environment causes a 1.5 m/sec increase in maximum wind and a 6 percent increase in the generation of available potential energy. The total heat loss by infrared radiation for a domain of radius 1000 km is about one half the total heat addition.

Key Words: Hurricane, cyclone, model, steady-state, energetics, dynamics

# A DIAGNOSTIC MODEL OF THE TROPICAL CYCLONE IN ISENTROPIC COORDINATES

Richard Allen Anthes

## 1. INTRODUCTION

Since the early synoptic studies by Redfield (1831) and Reid (1841), much effort has been directed toward understanding the formation and maintenance of tropical cyclones. By the 1920s, the release of latent heat had been identified as the tropical cyclone's prime energy source (Cline, 1926). Subsequently, much effort was directed toward estimating the magnitude of the heating and understanding the mechanism of its release for the large scale. The magnitude is readily estimated from observed precipitation rates. However, the process of large scale warming of the environment by latent heat release in convection is quite complex, and involves interactions between cumulus and cyclone scales of motion (Charney and Eliassen's, 1964, "conditional instability of the second kind").

Within the last decade, numerical modeling has become a powerful tool for investigating the life cycle of tropical cyclones. The first numerical models (e.g., Kasahara, 1961; Kuo, 1965; Syōno, 1962; Rosenthal, 1964) were unsuccessful, primarily because the latent heating was appropriate to the cloud scale rather than the hurricane scale. The circulations

in these experiments developed extremely rapidly and eventually became unstable through the growth of small scale disturbances. With a more realistic parameterization of latent heat release, the models of Yamasaki (1968 a,b), Ooyama (1969) and Rosenthal (1969) have been successful in duplicating many observed features of tropical storms. The practical limitations of computer size and speed, however, have restricted these models to two dimensions and have forced parameterization of other important physical processes such as vertical and horizontal mixing and sea-air interactions.

In the parameterization of the heat imparted to the environment by the cumulus convection attempted by Kuo (1965), Rosenthal (1969), and others, large scale heating is a function of the cloud-environment temperature difference and the net moisture convergence in a column. These models release a much larger proportion of heat in the upper troposphere than the heat released by earlier models based on a pseudo-adiabatic process.

The importance of latent heat release within the warm core for the production of kinetic energy was recognized by Palmén (1948) and reemphasized by Yanai (1964). In simplest terms, the release of latent heat maintains the baroclinicity that drives the transverse radial circulation. The horizontal kinetic energy is produced in both the inward and outward flowing branches by accelerations toward lower pressure.

This production of kinetic energy, in turn, offsets surface and internal frictional dissipation.

The conversion of potential to kinetic energy through cross-isobar flow has been examined in several diagnostic studies, e.g., Palmén and Jordan (1955), Palmén and Riehl (1957), Riehl and Malkus (1961), Miller (1958), and Hawkins and Rubsam (1968). Recently, employing the concept of available potential energy, Anthes and Johnson (1968) estimated the generation of available potential energy by diabatic heating in Hurricane Hilda, 1964 and concluded that the generation within a 1000 km region was sufficient to balance the conversion to kinetic energy. Thus, on this scale, it was possible to consider that the hurricane was a self-sustaining system.

The importance of differential heating and cooling is emphasized in the theory of available potential energy. Anthes and Johnson's (1968) results showed that the generation was sensitive to horizontal and vertical variations in latent heating and that infrared cooling in the hurricane environment could account for 17 percent of the total generation.

The sensitivity of the generation to different horizontal and vertical distributions of heating suggests investigating the effect of differential heating on the dynamics as well as the energetics of tropical storms. In particular, the

relation between generation of available energy and conversion to kinetic energy within the storm system should be studied to clarify the role of thermal versus mechanical forcing. This relationship has important implications in storm modification experiments in which the heating, generation, and possibly the conversion is altered in some manner.

Although interactions between temperature and momentum structure and large scale heating certainly exist, the hurricane may be considered a direct consequence of thermal forcing. It makes sense, therefore, to study the direct response of the hurricane to differential heating by specifying steady heating distributions. The steady-state mass and momentum fields that develop in response to the steady forcing functions are useful in interpreting transient stages in results of hurricane forecast models as well as in testing of various heating parameterizations. Indeed, it is important to determine whether realistic steady-state solutions exist at all.

In previous steady-state models, Krishnamurti (1961, 1962) and Barrientos (1964) have calculated the transverse circulations required to maintain specified (observed) tangential circulations. Although these models have yielded interesting results for synoptic cases, difficulties arise from the assumption of constant tangential winds (Anthes, 1970). Therefore, in the present study, the tangential

circulations are investigated as functions of heating, rather than vice-versa.

The dynamics and energetics of the hurricane's response to thermal forcing are studied through a two dimensional model in isentropic coordinates. An iterative technique is utilized to obtain steady-state solutions of mass and momentum for different vertical and horizontal latent heating distributions, for infrared radiative cooling, and sensible heat addition at the earth's interface. The effects of vertical and horizontal mixing are also considered.

It is well to note that the comparative performances of numerical models under different physical processes or under varying parameters may yield more insight into important atmospheric processes than the values computed in any one experiment. For example, variations between solutions under different heating functions should indicate, at least qualitatively, how the atmosphere might react to similar changes. This argument stems from the supposition that by varying only one parameter at a time the errors introduced by other approximations will tend to cancel, in spite of the complicated non-linear interactions.

## 2. AVAILABLE POTENTIAL ENERGY OF LIMITED REGIONS

The concept of separating that part of the energy which might be converted to kinetic energy from the total internal and potential energy of a thermodynamic system was introduced by Margules (1903), who called the former "available kinetic energy." In an explanation of the maintenance of the general circulation, Lorenz (1955) applied Margules' concept to the entire atmosphere and defined available potential energy as the difference between the sum of internal and potential energies of the atmosphere and the sum of these energies that would exist after an adiabatic mass redistribution to a statically stable horizontal density stratification. In their review, Dutton and Johnson (1967) reemphasized the importance of heating at high pressure and cooling at low pressure in the generation of available potential energy.

The theory of avilable potential energy has historically been applied to the entire atmospheric system. In diagnostic studies, however, the concept of available potential energy over limited atmospheric regions has been utilized to estimate contributions to the global available potential energy budget by processes within the region, (see Smith and Horn 1969). To define the available potential energy of a storm and its time rate of change, Johnson (1969)

has developed the theory for an open system. In this manner the generation of available potential energy within synoptic features such as extratropical cyclones has been studied by Bullock and Johnson (1969) and Gall and Johnson (1969).

One appealing aspect of applying the theory of available potential energy to a tropical cyclone is the condition that, as a first approximation, the hurricane may be considered an isolated baroclinic disturbance superimposed on the nearly flat and horizontal barotropic tropics. Thus one might reasonably expect the available potential energy generated on the tropical cyclone scale to be converted to kinetic energy within the same scale. This may not be true in the middle latitudes where the flux of energy across the boundaries of systems will be large.

## 2.1 Available Potential Energy Equations for the Model

Following Johnson (1969), the total internal and potential energy, E, of any region in hydrostatic balance is

$$E = \frac{C_p}{P_o^{\kappa} g(1+\kappa)} \int_{\sigma}\int_{0}^{\infty} P^{1+\kappa}\, d\theta\, d\sigma \qquad (1)$$

and that of the reference state, $E_r$, is

$$E_r = \frac{C_p}{P_o^{\kappa} g(1+\kappa)} \int_{\sigma}\int_{0}^{\infty} P_r^{1+\kappa}\, d\theta\, d\sigma \qquad (2)$$

The available potential energy, A, of the region equal to $E - E_r$ is then

$$A = \frac{C_p}{p_o^{\kappa} g(1+\kappa)} \int_{\sigma} \int_{0}^{\infty} (p^{1+\kappa} - p_r^{1+\kappa})\, d\theta\, d\sigma \qquad (3)$$

Dividing the vertical integration into three parts, (3) becomes

$$A = \frac{C_p}{p_o^{\kappa} g(1+\kappa)} \left[ \int_{\sigma} \int_{0}^{\theta_o} (p^{1+\kappa} - p_r^{1+\kappa})\, d\theta\, d\sigma + \int_{\sigma} \int_{\theta_o}^{\theta_t} (p^{1+\kappa} - p_r^{1+\kappa})\, d\theta\, d\sigma + \int_{\sigma} \int_{\theta_t}^{\infty} (p^{1+\kappa} - p_r^{1+\kappa})\, d\theta\, d\sigma \right] \qquad (4)$$

In (4), $\theta_o$ is the coldest potential temperature in the region, and $\theta_t$ is the isentropic surface above which the atmosphere is assumed to be barotropic. The third integral vanishes by the barotropic assumption. Following Lorenz' convention that the pressure on isentropes which intersect the ground equals the surface pressure, the available potential energy for the model is

$$A = \frac{C_p}{p_o^{\kappa} g(1+\kappa)} \left[ \int_{\sigma} (p_s^{1+\kappa} - \bar{p}_s^{1+\kappa})\, d\sigma + \int_{\sigma} \int_{\theta_o}^{\theta_t} (p^{1+\kappa} - \bar{p}^{1+\kappa})\, d\theta\, d\sigma \right] \qquad (5)$$

In (5) we have used the conditions that for hydrostatic atmospheres $p_r(\theta)$ equals $\bar{p}(\theta)$ and $p_{s_r}$ equals $\bar{p}_s$.

In this model in which heating vanishes on the upper boundary, the time rate of change of A (after Johnson, 1969)

is

$$\frac{dA}{dt} = G + C + B \ , \tag{6}$$

where

$$G = -\frac{1}{g}\int_{\sigma}\int_{\theta_0}^{\theta_t}\left[1 - \left(\bar{P}/p\right)^{\chi}\right] \dot{Q}\,\frac{\partial p}{\partial \theta}\, d\theta\, d\sigma, \tag{7}$$

$$C = -\frac{1}{g}\int_{\sigma}\int_{\theta_0}^{\theta_t}(\mathbf{V}\cdot\nabla_{\theta}\psi)\,\frac{\partial p}{\partial \theta}\, d\theta\, d\sigma \ , \tag{8}$$

$$B = \frac{1}{g}\int_{\sigma}\int_{\theta_0}^{\theta_t}\nabla_{\theta}\cdot\frac{\partial p}{\partial \theta}\,(\psi - \psi_r)\mathbf{V}\, d\theta\, d\sigma \ . \tag{9}$$

The generation, G, by diabatic heating is positive for heating at high pressure and cooling at low pressure. The conversion, C, is the production of kinetic energy by cross-isobar flow. The last term, B, represents the change of A by mass flux across the lateral boundary. In closed systems such as the entire atmosphere, B vanishes. On the axisymmetric assumption for the model, B becomes simplified to

$$B = \frac{2\pi R}{g}\int_{\theta_0}^{\theta_t} v_r\,(\psi - \psi_r)\,\frac{\partial p}{\partial \theta}\, d\theta \ . \tag{10}$$

For the hurricane, the surface pressure at the outer boundary will be greater than the mean surface pressure, so that $\psi > \psi_r$ . From the low level inflow, the covariance of $\left(\frac{\partial p}{\partial \theta}\ v_r\right)$ and $(\psi - \psi_r)$ will be positive. In the outflow region $(\psi - \psi_r)$ tends to vanish; thus the integral B usually provides a positive contribution to d A/dt.

## 2.2 Budget Equations for Volume

In this section the time dependent budget equations are developed for a stationary cylindrical volume. If f is any specific quantity, such as water vapor per unit mass, the total amount of the property in the volume is

$$F = \int_0^{2\pi}\int_0^{R}\int_{\theta_0}^{\theta_t} r\rho\frac{\partial z}{\partial\theta} f \, d\theta \, dr \, d\lambda \quad . \tag{11}$$

With the aid of Leibnitz' rule and the hydrostatic assumption, the time rate of change of F is

$$\frac{dF}{dt} = -\frac{1}{g}\int_0^{2\pi}\int_0^{R}\int_{\theta_0}^{\theta_t}\left[\frac{\partial}{\partial t}\left(r\frac{\partial p}{\partial\theta}f\right) + \frac{\partial}{\partial\lambda}\left(r\frac{\partial p}{\partial\theta}f\frac{d\lambda_B}{dt}\right) + \frac{\partial}{\partial r}\left(r\frac{\partial p}{\partial\theta}f\frac{dr_B}{dt}\right) + \frac{\partial}{\partial\theta}\left(r\frac{\partial p}{\partial\theta}f\frac{d\theta_B}{dt}\right)\right] d\theta \, dr \, d\lambda \,, \tag{12}$$

where the subscript B identifies the arbitrary moving boundaries. The addition of the continuity equation and the relation

$$r\frac{\partial p}{\partial\theta}\frac{df}{dt} = r\frac{\partial p}{\partial\theta}\left[\frac{\partial f}{\partial t} + v_r\frac{\partial f}{\partial r} + \frac{v_\lambda}{r}\frac{\partial f}{\partial\lambda} + \frac{d\theta}{dt}\frac{\partial f}{\partial\theta}\right] \tag{13}$$

yields

$$\frac{\partial}{\partial t}\left(r\frac{\partial p}{\partial\theta}f\right) = -\frac{\partial}{\partial\lambda}\left(\frac{\partial p}{\partial\theta}fv_\lambda\right) - \frac{\partial}{\partial r}\left(r\frac{\partial p}{\partial\theta}fv_r\right) - \frac{\partial}{\partial\theta}\left(r\frac{\partial p}{\partial\theta}f\frac{d\theta}{dt}\right) + r\frac{\partial p}{\partial\theta}\frac{df}{dt} \,. \tag{14}$$

From the substitution of (14) into (12), the time rate of change of F is

$$\frac{dF}{dt} = \frac{1}{-g} \int_0^{2\pi} \int_0^{R} \int_{\theta_0}^{\theta_t} \left( - \frac{\partial \frac{\partial P}{\partial \theta} f\left(v_\lambda - dt \frac{d\lambda_B}{r}\right)}{\partial \lambda} - \frac{\partial r \frac{\partial P}{\partial \theta} f \left(v_r - dt \frac{dr_B}{}\right)}{\partial r} \right.$$

$$\left. - \frac{\partial r \frac{\partial P}{\partial \theta} f \left(\frac{d\theta}{dt} - \frac{d\theta_B}{dt}\right)}{\partial \theta} + r \frac{\partial P}{\partial \theta} \frac{df}{dt} \right) d\theta \, dr \, d\lambda. \tag{15}$$

Equation (15) is greatly simplified for the stationary axisymmetric volume of this study in which all tangential derivatives vanish and $dr_B/dt$ equals zero. Thus

$$\frac{dF}{dt} = \frac{-2\pi}{g} \int_0^{R} \int_{\theta_0}^{\theta_t} \left( - \frac{\partial r \frac{\partial P}{\partial \theta} f v_r}{\partial r} - \frac{\partial r \frac{\partial P}{\partial \theta} f \left(\frac{d\theta}{dt} - \frac{d\theta_B}{dt}\right)}{\partial \theta} \right. \tag{16}$$

$$\left. + r \frac{\partial P}{\partial \theta} \frac{df}{dt} \right) d\theta \, dr \quad .$$

The upper and lower boundary conditions are

$d\theta_B/dt = d\theta_s(r, \theta_s, t)/dt$ and $d\theta_t/dt = d\theta_B/dt = 0$.

With these conditions

$$\frac{dF}{dt} = - \frac{2\pi}{g} \int_0^{R} \int_{\theta_0}^{\theta_t} \left( - \frac{\partial r \frac{\partial P}{\partial \theta} f v_r}{\partial r} + r \frac{\partial P}{\partial \theta} \frac{df}{dt} \right) d\theta \, dr \, , \tag{17}$$

and, upon integration, the final budget equation becomes

$$\frac{dF}{dt} = \frac{2\pi R}{g} \int_{\theta_0}^{\theta_t} \left( \frac{\partial P}{\partial \theta} f v_r \right)_R d\theta - \frac{2\pi}{g} \int_0^{R} \int_{\theta_0}^{\theta_t} r \frac{\partial P}{\partial \theta} \frac{df}{dt} \, d\theta \, dr \quad . \tag{18}$$

The first term is the change of F caused by transport of f across the lateral boundary while the second term is the change due to sources, or sinks, e.g., evaporation or condensation within the volume of a water vapor budget.

The generalized budget and available potential engery equations provide integrated parameters for the hurricane volume, which are studied as the mass and momentum fields seek steady-state conditions for the applied thermal forcing.

## 3. THE DIAGNOSTIC MODEL

One of the appealing aspects of numerical modeling in isentropic coordinates is the absence of a "vertical velocity" in the equations of motion for isentropic flows. Such a model should have less truncation error than models in pressure or height coordinates that must include vertical advection terms. Even under diabatic conditions it is probable that the vertical truncation is less in isentropic coordinates, because the adiabatic part of the vertical motion should be free of error.

Besides the reduction in vertical truncation error, there are several other possible advantages of modeling in isentropic corrdinates:

(1) The theory of available potential energy is exact in isentropic coordinates (Dutton and Johnson, 1967).

(2) Johnson and Dutton (1970) stress that mean energy and momentum transport processes of the general circulation are explicity coupled with thermal forcing.

(3) Horizontal and vertical resolution is higher in the energetically active baroclinic zones.

Difficulties in using isentropic coordinates arise chiefly near the ground, where super-adiabatic lapse rates are found and isentropic surfaces intersect the ground. The first problem generally arises over small areas and may be solved by utilizing height coordinates in the boundary layer and isentropic coordinates above. The second has been reasonably well resolved by an interpolation scheme in some preliminary, adiabatic experiments by Eliassen and Raustein (1968).

To the author's knowledge, there has been no previous work with numerical modeling in isentropic coordinates which includes diabatic processes. In this particular series of experiments in which the heating function is specified and the steady-state response determined, isentropic coordinates are especially attractive because the form of the thermodynamic equation is greatly simplified. In a broader sense, the experience gained by studying thermal forcing in this model should be useful in future work with more advanced numerical models.

### 3.1 Steady State or Slowly Varying Concept

The term steady state, when applied to the tropical cyclone, usually refers to the storm's mature stage in which certain significant parameters, such as central pressure and maximum wind, remain relatively unchanged over a period

of time. Axisymmetric assumption is usually best satisfied during this mature stage.

In the iteration technique used in this model, mass and momentum are "forecast" using a constant, specified heating function until a slowly varying state is reached. True steady-state conditions are never determined because of the large amount of time required to reach such a state. In typical experiments, changes from initial conditions in response to the constant heating function are very large during the first few iterations as the mass and momentum fields attempt to adjust to the new forcing function. Later, however, rates of change are less. When this "slowly varying" state is reached (usually after about 1200 iterations) differences in the results caused by experimental variation of physical processes or parameters are apparent. Later some objective measures are presented to determine when this state is attained. Again, it is the differences between experiments, rather than the absolute values of any one experiment, that are significant.

## 3.2 Description of Model

### 3.2.1 Basic Equations

The tangential and radial equations of motion and the continuity equation in isentropic coordinates are

$$\frac{\partial rv_\lambda}{\partial t} = -v_r\frac{\partial rv_\lambda}{\partial r} + r\left[-fv_r - \frac{d\theta}{dt}\frac{\partial v_\lambda}{\partial\theta} + K_H\left(\nabla^2 v_\lambda - \frac{v_\lambda}{r^2}\right) + \frac{\partial}{\partial z}K_z\frac{\partial v_\lambda}{\partial z}\right], \tag{19}$$

$$\frac{\partial v_r}{\partial t} = -v_r\frac{\partial v_r}{\partial r} + fv_\lambda + \frac{v_\lambda^2}{r} - \frac{\partial\psi}{\partial r} - \frac{d\theta}{dt}\frac{\partial v_r}{\partial\theta} + K_H\left(\nabla^2 v_r - \frac{v_r}{r^2}\right) + \frac{\partial}{\partial z}K_z\frac{\partial v_r}{\partial z}, \tag{20}$$

$$\frac{\partial}{\partial t}\frac{\partial p}{\partial\theta} = -\frac{1}{r}\frac{\partial}{\partial r}v_r\frac{\partial p}{\partial\theta} - \frac{\partial}{\partial\theta}\frac{d\theta}{dt}\frac{\partial p}{\partial\theta}, \tag{21}$$

where the horizontal and vertical mixing terms in (19) and (20) are expressed in height coordinates rather than the more complex transformed expressions for computational convenience. This approximation is justified from the relatively large uncertainty in the form of $K_H$ and $K_z$.

The "vertical velocity" term in isentropic coordinates, $d\theta/dt$, is computed from

$$\frac{d\theta}{dt} = \frac{1}{C_p}\frac{\theta}{T}\dot{Q} + K_T\left\{ -\frac{\partial \rho^{-1}}{\partial \theta}\left[\frac{\partial^2 P}{\partial r^2} - \frac{\partial P^{-1}}{\partial \theta}\frac{\partial P}{\partial r}\left(2\frac{\partial^2 \rho}{\partial r \partial \theta}\right.\right.\right.$$
$$\left.\left.\left. - \frac{\partial \rho^{-1}}{\partial \theta}\frac{\partial \rho}{\partial r}\frac{\partial^2 P}{\partial \theta^2}\right)\right] + \left(r\frac{\partial \rho}{\partial \theta}\right)^{-1}\frac{\partial \rho}{\partial r}\right\} + \frac{\partial}{\partial z}\frac{Kz\,\partial\theta}{\partial z}, \qquad (22)$$

where $\dot{Q}$ is the parameterized heating rate.

The second term in (22) results from approximating the horizontal diffusion by $K_T \nabla^2 \theta$ in pressure coordinates and transforming to isentropic coordinates. Again the uncertainties in $K_T$ outweigh the error in the approximation.

For the surface, drag friction replaces the vertical mixing term in the equations of motion,

$$\frac{\partial r v_\lambda}{\partial t} = -v_r \frac{\partial r v_\lambda}{\partial r} + r\left[ -f v_r - \frac{C_D |V| v_\lambda}{\Delta z} + K_H \left(\nabla^2 v_\lambda - \frac{v_\lambda^2}{r}\right)\right], \qquad (23)$$

$$\frac{\partial v_r}{\partial t} = -v_r \frac{\partial v_r}{\partial r} + f v_\lambda + \frac{v_\lambda^2}{r} - \frac{C_p \theta}{p_o^\chi}\frac{\partial p^\chi}{\partial r} - \frac{C_D |V| v_r}{\Delta z}$$
$$+ K_H\left(\nabla^2 v_r - \frac{v_r^2}{r}\right). \qquad (24)$$

The local change of surface potential temperature computed from the thermodynamic equation is

$$\frac{\partial \theta_s}{\partial t} = -v_r \frac{\partial \theta_s}{\partial r} + \frac{d\theta_s}{dt} + K_T \nabla^2 \theta_s . \qquad (25)$$

The remaining equations constituting the complete set are the hydrostatic equation,

$$\frac{\partial \Psi}{\partial \theta} = C_p \frac{T}{\theta} \quad , \tag{26}$$

and the definition of potential temperature,

$$\theta = T \, (P_o/P)^{\kappa} \quad . \tag{27}$$

3.2.2 Finite Difference Equations

The geometry of the model (fig. 1) consists of 12 equally spaced isentropic surfaces ($\theta_i = 370^{\circ}K - i\,\Delta\theta$, $\Delta\theta = 5^{\circ}$ K, i = 1, 12) and the sea level surface. The approximate mean tropical pressures of the even isentropic surfaces are given for reference (Jordan, 1958). The variables, $v_\lambda$ , $v_r$ , p , $\Psi$ , $\dot{Q}$ , and $d\theta/dt$, are all defined on the sea level surface. On the isentropic surfaces the variables are staggered for computational convenience with $v$ , $\Psi$ , and $\frac{\partial P}{\partial \theta}$ defined on odd surfaces. The horizontal grid is also staggered with $v$ defined at $r = (j-1)\Delta r$ and the thermodynamic variables ( $\Psi$ , p , $\dot{Q}$ , $d\theta/dt$) defined at $r_{j+\frac{1}{2}} = (j-\frac{1}{2})\Delta r$ for j = 1, 2 ....J. The horizontal domain extends to the radius $R_J$, which is either 500 or 1000 km.

In (19) through (25) all space derivatives are estimated by centered differences. The finite difference form of the RHS of (24) is given for reference with the i index suppressed for simplicity,

$$\frac{\partial v_r}{\partial t} \doteq -v_{r_j}\left(\frac{v_{r_{j+1}} - v_{r_{j-1}}}{r_{j+1} - r_{j-1}}\right) + f v_{\lambda_j} + \frac{v_{\lambda_j}^2}{r_j} - \frac{c_p \theta}{p_o^{\kappa}} \frac{p^{\kappa}_{j+1\frac{1}{2}} - p^{\kappa}_{j+\frac{1}{2}}}{(r_{j+1\frac{1}{2}} - r_{j+\frac{1}{2}})}$$

$$- \frac{c_D \left[v_{\lambda_j}^2 + v_{r_j}^2\right]^{\frac{1}{2}} v_{r_j}}{\Delta z} + K_H \left\{ \frac{\frac{v_{r_{j+1}} - v_{r_j}}{r_{j+1} - r_j} - \frac{v_{r_j} - v_{r_{j-1}}}{r_j - r_{j-1}}}{.5\,(r_{j+1} - r_{j-1})} \right. \qquad (28)$$

$$\left. - \frac{v_{r_{j+1}} - v_{r_{j-1}}}{r_j (r_{j+1} - r_{j-1})} - \frac{v_{r_j}}{r_j^2} \right\}.$$

For the calculation of the vertical mixing term, the finite difference approximation is

$$\frac{\partial K_z}{\partial z}\frac{\partial v_r}{\partial z}\Bigg|_i \approx \frac{K_{z_{i-1}}\left(\frac{v_{ri-1} - v_{r_i}}{z_{i-1} - z_i}\right) - K_{z_i}\left(\frac{v_{ri} - v_{ri+1}}{z_i - z_{i+1}}\right)}{0.5\,(z_{i-1} - z_i)} \qquad (29)$$

where i refers to the level. The unwieldy expressions for the second derivative terms are greatly simplified for a constant grid interval. The general form is retained however, in anticipation of the use of a variable grid in some experiments.

The pressure is obtained from "forecast" values of $\frac{\partial p}{\partial \theta}$ by integrating downward from a fixed value of p(365°K):

$$p_{i+1} = p_{i-1} - (\theta_{i-1} - \theta_{i+1})\frac{\partial p}{\partial \theta_i} \quad , \; i = 2, 4, \ldots .12. \qquad (30)$$

At the sea surface $\theta$ equals $\theta_s$ (r). From an integration of the hydrostatic equation upward from sea level, $\Psi$ on even surfaces is

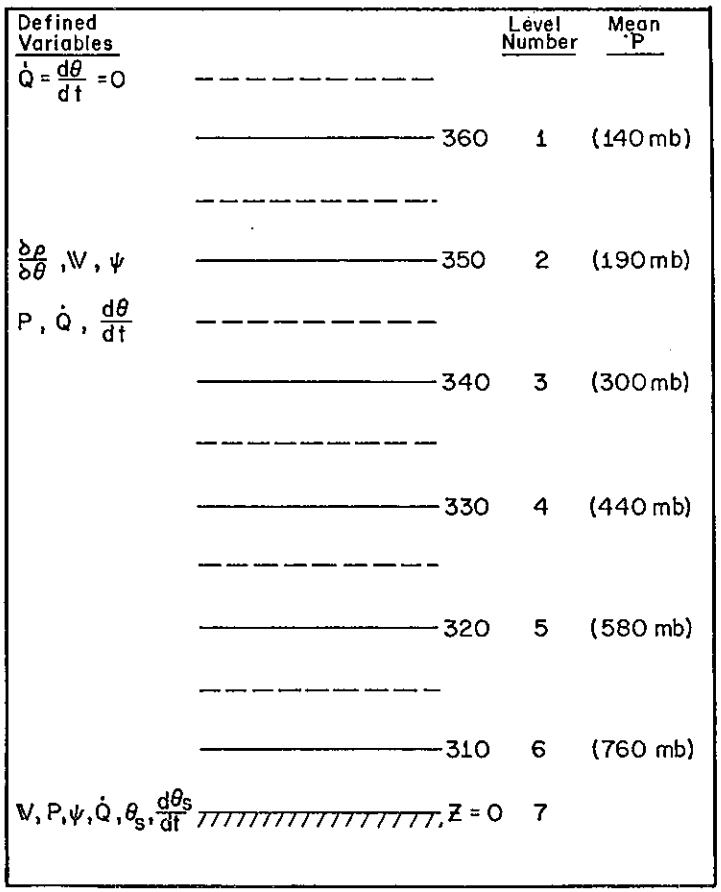


Figure 1. Geometry of isentropic model of the hurricane

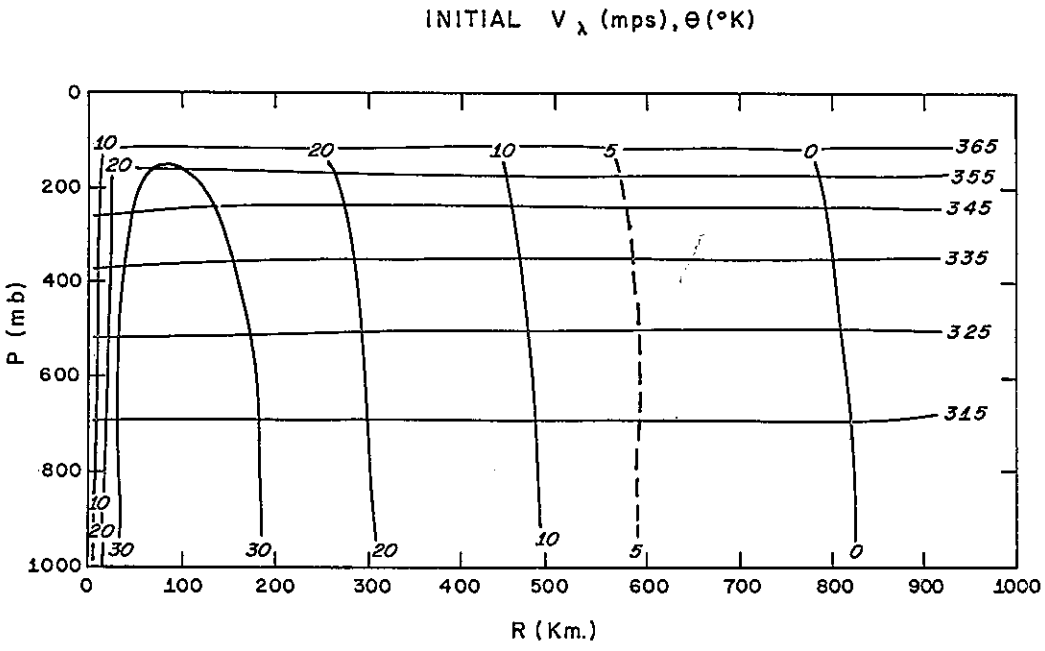


Figure 2. Initial tangential winds and potential temperatures for experiments

$$\Psi_{i-1} = \Psi_{i+1} + (\theta_{i-1} - \theta_{i+1})\, C_p \left(\frac{p}{p_o}\right)^{\kappa}_{i} \quad , \quad i = 12,\ 10,\ \ldots.2 \qquad (31)$$

where $\Psi_{12}$ equals $c_p T_{12}$ .

### 3.2.3 Boundary Conditions

The boundary conditions for the top isentropic surface are p equal to 135 mb, $d\theta/dt$ equal zero and $\frac{\partial w}{\partial z}$ equal zero. At the lateral boundary the pressure and temperature gradients, the horizontal divergence, and the relative vorticity are all assumed to vanish, which enables the calculation of the variables at $R_J$ by

$$P_J = P_{J-1} \qquad (rv_r)_J = (rv_r)_{J-1}$$

$$\Psi_J = \Psi_{J-1} \qquad (rv_\lambda)_J = (rv_\lambda)_{J-1} \qquad (32)$$

$$(\theta_s)_J = (\theta_s)_{J-1} \quad .$$

### 3.2.4 Computational Procedure

The iteration technique to determine the steady-state solutions utilizes a simulated backward difference scheme (Matsuno, 1966), which has the desirable property of damping high frequency waves. One cycle of the scheme is summarized with the superscript referring to the iteration step number:

(1) Given values of $v_\lambda^n$ , $v_r^n$ , $\Psi^n$ , $p^n$, $d\theta/dt^n$, $\theta_s^n$

(2) "Forecast" tentative values $v_\lambda^*$ , $v_r^*$ , $\frac{\partial p}{\partial \theta}^*$ , $\theta_s^*$

at step n+1 (designated by $^*$ ) using appropriate tendency equations (19) through (25) and values of variables at step n.

(3) Calculate $p^*$ and $\psi^*$ from (30) and (31) using tentative estimates $\frac{\partial p}{\partial \theta}^*$ and $\theta_s^*$ .

(4) Forecast final estimates of $v_\lambda\, n+1$ , $v_r n+1$ , $\frac{\partial p}{\partial \theta}\, n+1$ , and $\theta_s^{n+1}$ from same equations in step 2 by using $^*$ values of variables where they appear in tendency equations.

(5) Calculate $p^{n+1}$ and $\psi^{n+1}$ from (30) and (31).

(6) Calculate $d\theta/dt^{n+1}$ from (22)

(7) Calculate variables at lateral boundary from (32).

This completes one iteration step.

To determine when the quasi-steady state has been reached, the following norms on any iterated variable, f, are defined by

$$L_\infty \equiv \max_{\text{all } j} \left| f_j^n - f_j^{n-20} \right| , \tag{33}$$

$$L_2 \equiv \left[ \frac{1}{N} \sum_{j=1}^{N} (f_j^n - f_j^{n-20})^2 \right]^{\frac{1}{2}} \tag{34}$$

After each 20th iteration cycle, $L_\infty$ and $L_2$ are computed with f equal to the radial and tangential winds. These norms are computed for separate radial rings, 0-200, 200-400, 400-600 .....km, and for each level to determine which parts

of the domain reach a slowly varying state first.

### 3.2.5 Computational Stability

The computational stability analysis of the complete set of equations is very complicated. Separate analyses were made for various combinations of the linearized prediction equations. The most stringent stability requirement from these results yields an estimate for the requirement for the complete set of non-linear equations.

The most severe restriction on the size of the time increment, $\Delta t$, is governed by the speed of the external gravity wave. By considering the continuity equation and the radial equation of motion, the criterion for linear computational stability is $\frac{\Delta t}{\Delta r}\sqrt{\bar{p}/\bar{\rho}} \leq 1$, where $\bar{\rho}$ and $\bar{p}$ are mean density and pressure, respectively, and $\sqrt{\bar{p}/\bar{\rho}}$ is the approximate speed of the external gravity wave (about 330 m/sec). The analysis for this condition is presented in appendix B.

### 3.2.6 Mass Budget

Because the model predicts mass changes directly from the continuity equation, it is essential that the finite difference equations preserve mass exactly so that there are no fictitious sources in the system. The mass budget equation obtained by letting f equal 1 in (18) is

$$\frac{dM}{dt} = \frac{2\pi R}{g} \int_{\theta_0}^{\theta_t} \left(\frac{\partial p}{\partial \theta} v_r\right)_R \, d\theta \quad . \tag{35}$$

By the centered finite difference scheme

$$\sum_{j=1}^{J} \frac{\Delta\left(rv \frac{\partial p}{\partial \theta}\right)}{\Delta r}_j \Delta r_j = R_J \left(v_r \frac{\partial p}{\partial \theta}\right)_J \quad , \tag{36}$$

and only flow across the horizontal boundary at $R_J$ can contribute to a net mass change in the region.

### 3.2.7 Kinetic Energy Budget

The kinetic energy budget for the volume obtained by equating f to the specific kinetic energy, k, in (18) is

$$\frac{dk}{dt} = \frac{2\pi R}{g} \int_{\theta_0}^{\theta_t} \left(k \frac{\partial p}{\partial \theta} v_r\right)_R \, d\theta - \frac{2\pi}{g} \int_0^R \int_{\theta_0}^{\theta_t} r \frac{dk}{dt} \frac{\partial p}{\partial \theta} \, d\theta \, dr \, . \tag{37}$$

The time rate of change of the specific kinetic energy obtained by multiplying the tangential and radial equations of motion by $v_\lambda$ and $v_r$, respectively, and adding becomes

$$\frac{dk}{dt} = - v_r \frac{\partial \Psi}{\partial r} + K_H \left[ V_r \left(\nabla^2 v_r - \frac{v_r}{r^2}\right) + v_\lambda \left(\nabla^2 v_\lambda - \frac{v_\lambda}{r^2}\right) \right]$$

$$+ \frac{C_o}{\Delta Z} |V| \left(v_r^2 + v_\lambda^2\right) \qquad \text{surface only} \tag{38}$$

$$+ V_r \frac{\partial \, Kz \frac{\partial v_r}{\partial z}}{\partial z} + V_\lambda \frac{\partial \, Kz \frac{\partial v_\lambda}{\partial z}}{\partial z} \qquad \theta \text{ levels only.}$$

3.2.8 Initial Conditions

In all experiments the initial conditions (or first guess) consist of a vortex in gradient balance with a surface maximum of 37 m/sec at 80 km (fig. 2), a weak warm core with a temperature excess of $1^{\circ}C$ in the center, and a central pressure of 970 mb. Through the thermal wind relation, there is a slight decrease of wind speed with height. The environmental pressure is 1011 mb.

In the first two experiments, the radial winds initially were assumed to be zero; however, these conditions produced large pressure tendencies initially and generated large amplitude gravitational oscillations. In later experiments, the radial winds were calculated to balance the vertical divergence term in the continuity equation so that the initial pressure tendency was zero. These latter initial conditions resulted in a more gradual change of the mass field.

## 3.3 The Experimental Parameters

In the experiments presented in this paper , the constant parameters are the Coriolis parameter, the drag coefficient, and the depth of the boundary layer. The Coriolis parameter is $5.0 \times 10^{-5}$ $sec^{-1}$ and corresponds to $20^{\circ}N$. The drag coefficient, approximated by 0.003, was selected from

empirical studies (Miller, 1962) and should be a reasonable value for the high velocities found in hurricanes. The depth of the boundary layer is assumed to be 1.0 km.

Very little is known about the variation of the vertical mixing coefficient, $K_z$. However, it seems qualitatively reasonable to assume that the vertical mixing should decrease as the static stability increases. This effect is included in a crude fashion by decreasing $K_z$ linearly with height from a value prescribed for the 315° K isentropic surface (about 700 mb) to one half this value at the 365° surface. The value of $K_z$ referred to in the experiments is the maximum value.

## 4. EXPERIMENTAL RESULTS

In this section results from the more significant experiments are presented. After two preliminary adiabatic experiments to verify some of the simple aspects of the model, the role of internal (vertical and horizontal) mixing for a fixed heating function is investigated. Then for constant mixing coefficients, the response of the mass and momentum structures to various horizontal and vertical distributions of latent heating and infrared cooling is studied in the main set of experiments. Later, the computational aspects of the model, such as domain size, resolution, and variable grid

spacing, are considered, and finally fine horizontal resolution is utilized to study the effects of reduced horizontal mixing.

In all experiments, the latent heating function was computed by arbitrarily assuming a radial profile or rainfall rates and distributing the equivalent amount of heat vertically. In figure 3 the rainfall rates which determine the horizontal heating distributions in the various experiments are presented. The maximum rainfall rate of 50 cm/day at 30 km (corresponding roughly to the eyewall) is quite moderate for a mature hurricane. For example, Riehl and Malkus (1961) estimated a rainfall rate of 90 cm/day in hurricane Daisy (1958).

The variation of the vertical distribution is one of the interesting aspects of the problem in view of our lack of knowledge concerning the effective heat release for the hurricane scale. For the vertical profile of latent heating, $Q$ of (22) is prescribed as a function of mass, thus $\frac{d\theta}{dt}$ may vary as the isentropes move through the fluid. The two vertical profiles of latent heat release studied in the experiments are shown in figure 4. The basis for the form of these profiles is discussed in section 4.3.2. All experiments, except Experiment 10, utilize the distribution that releases the higher proportion of heat in the upper troposphere.

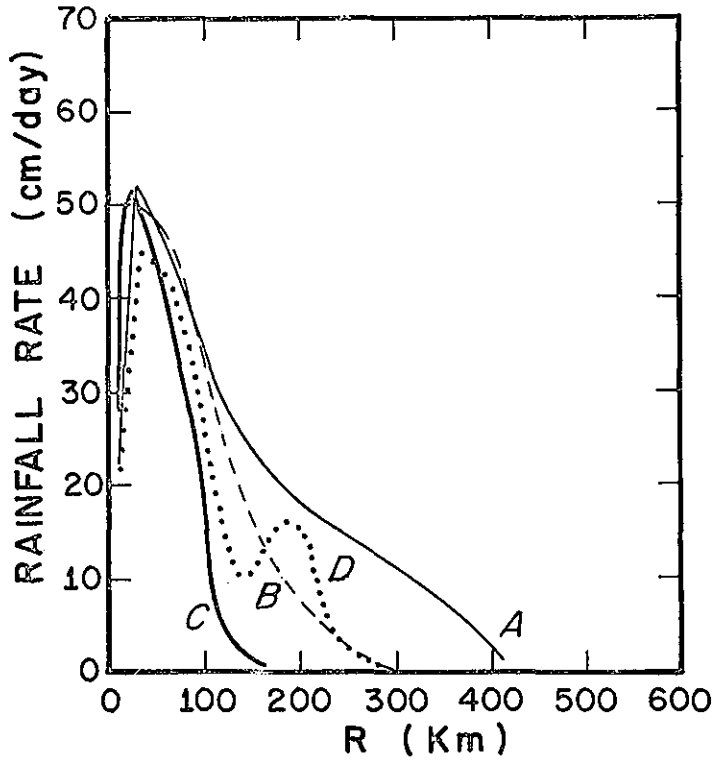


Figure 3. Radial profiles of rainfall rates used to specify horizontal variations of latent heating.

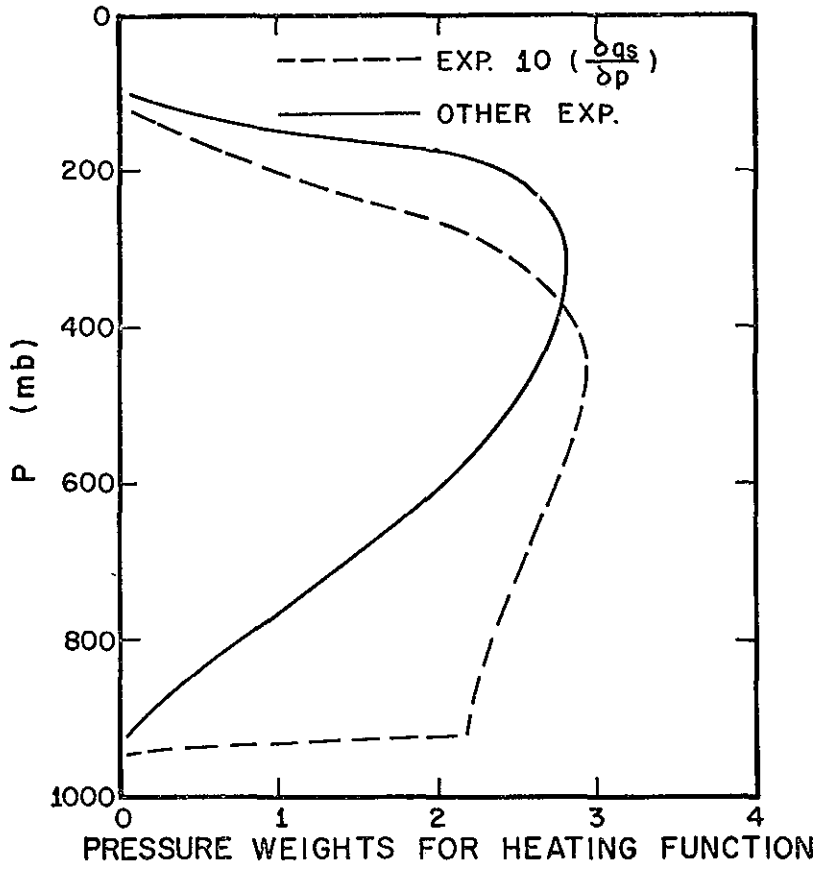


Figure 4. Vertical profiles of latent heat release for experiments

The importance of sensible heating at the sea-air interface to hurricane development and maintenance has been established from both empirical (Malkus and Riehl, 1960) and numerical (Ooyama, 1969) results. As air flows inward toward lower pressure in the boundary layer, the sensible heating increases its equivalent potential temperature. The higher equivalent potential temperature enhances the convection and increases the heating and generation of available potential energy. In this model, the sensible heating, $\dot{Q}_s$, is modeled by assuming the total sensible heating is $0.11 \times 10^{14}$ watts (Malkus and Riehl, 1960) and distributing the heat radially, as shown in figure 5. Therefore, there is no feed-back between sensible and latent heating and the model is insensitive to this effect. In computing $d\theta_s/dt$, (25) is approximated by

$$\frac{d\theta_s}{dt} = \frac{\theta_s}{C_p T_s} \dot{Q}_s \approx \frac{\dot{Q}_s}{C_p} \qquad (39)$$

### 4.1 Preliminary Adiabatic Experiments

In the first experiment, with no friction or heating, the initial gradient balance should be preserved except for small changes from round-off error. After 10 iterations an apparently random pattern of radial velocities with magnitude $10^{-3}$ cm/sec develops from the round-off error. After 200 iterations, when the computation

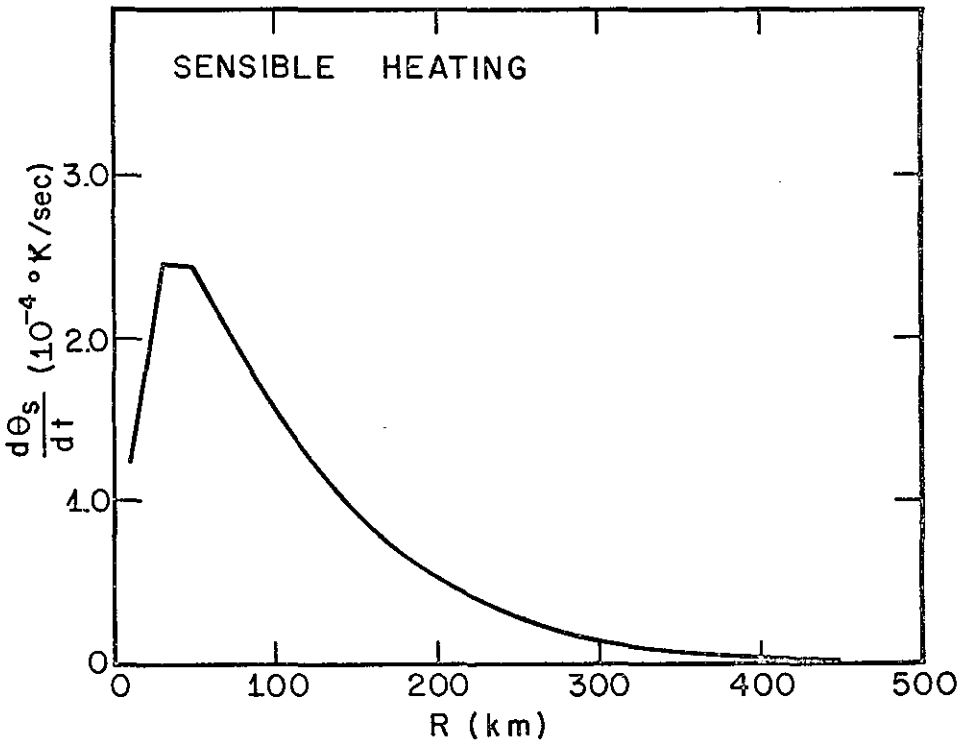


Figure 5. Surface potential temperature change by sensible heating

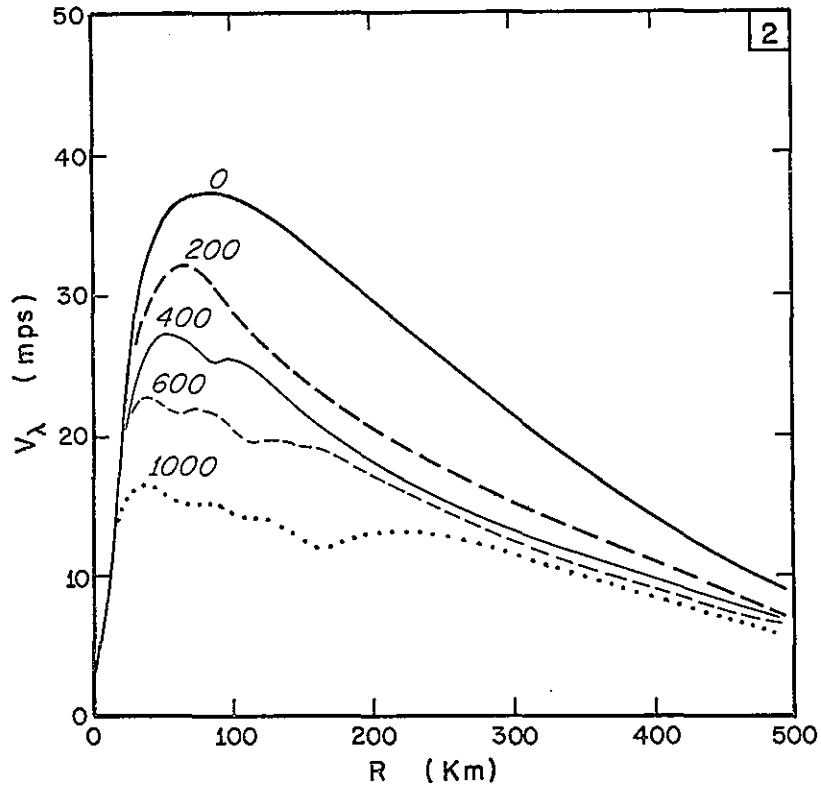


Figure 6. Radial profiles of surface tengential wind for various iteration steps in Experiment 2

is terminated, the radial velocity pattern is still random with maximum amplitudes of $10^{-2}$ cm/sec and the tangential velocities and pressures are unchanged to the precision of the output (0.01 cm/sec and 0.1 mb).

In Experiment 2 the heating and internal mixing are zero, and the effect of drag friction alone is examined ($C_D$ = 0.003). In this experiment with no heating the model is a true forecast model. A possible physical analogue is a tropical cyclone that moves over land with the consequence that its source of latent heat and sensible heat is rapidly diminished. The vortex is expected to decay as kinetic energy is dissipated in the boundary layer and adiabatic cooling by frictionally induced vertical motion destroys the warm core.

Figure 6 illustrates radial profiles of the surface tangential wind at various stages of the iteration. An erosion of the tangential wind maximum occurs with a reduction from 37 to 18 m/sec in 1000 steps (8.3 hours). The evolution of the radial winds is shown in figure 7. The maximum inflow quickly reaches about 12 m/sec and the radius of maximum inflow moves outward with time. In the upper levels, the outflow is characterized by stable inertial-gravity waves with amplitude 1 m/sec, which move outward from the center at about 35 m/sec. These waves are not as prominent in later experiments that include heating, probably because of the

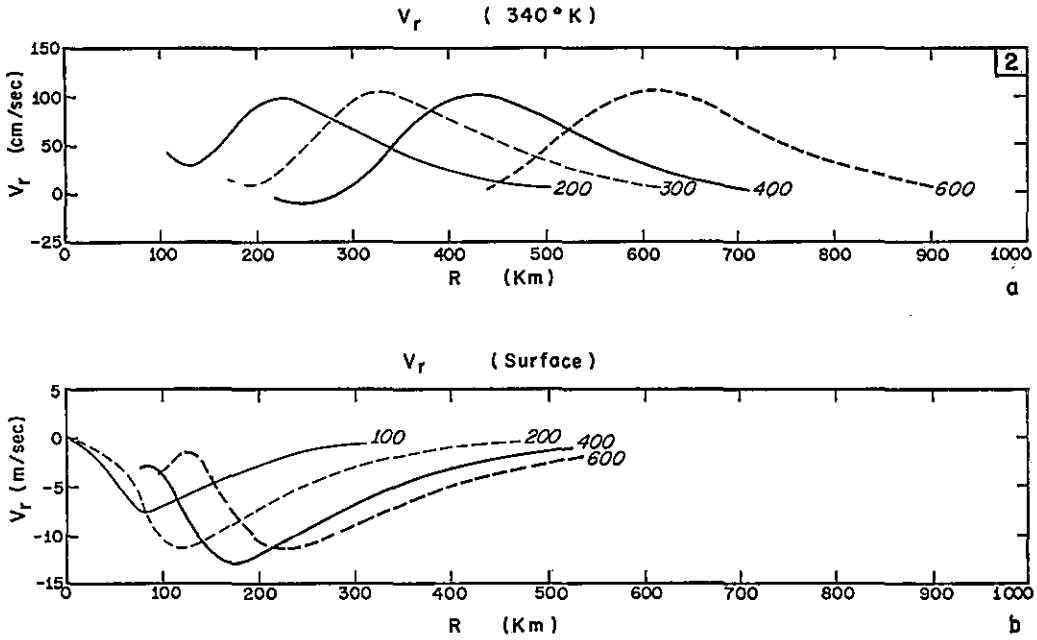


Figure 7. Radial profiles of radial winds for various iteration steps in Experiment 2

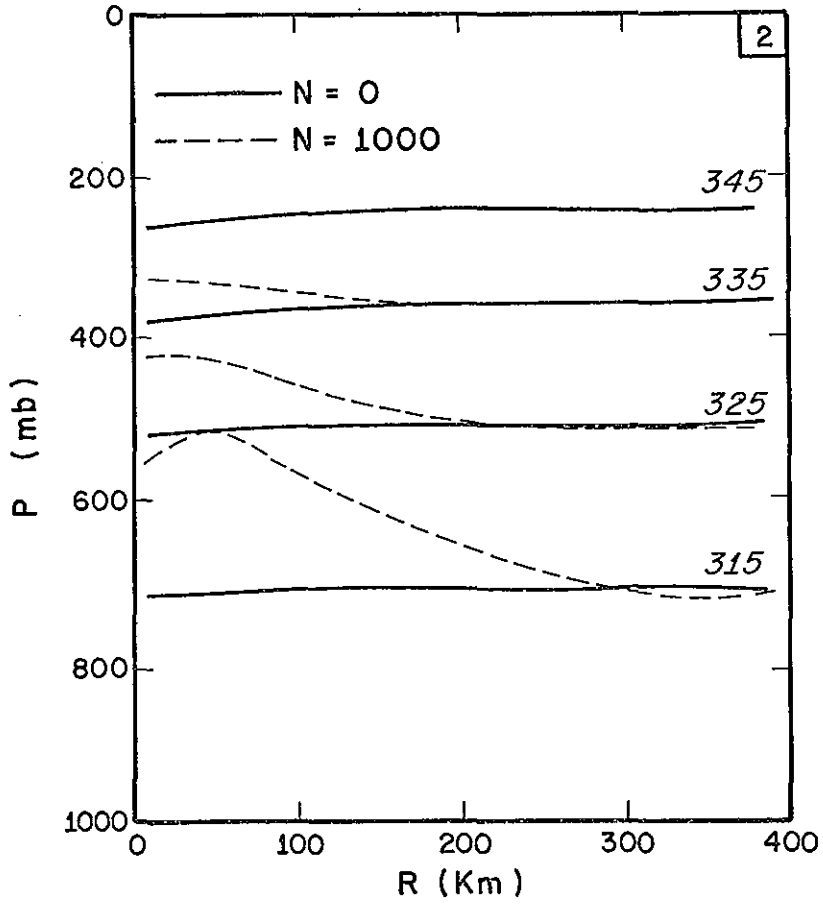


Figure 8. Isentropic cross section for the initial state and after 1000 steps in Experiment 2

steadying influence of the constant forcing function.

The thermal structure after 1000 steps is shown in figure 8. The initial warm core has been replaced by a cold core structure with a temperature decrease of 10°C in the vortex center. Strong adiabatic cooling in the inn er region associated with the frictionally induced vertical motion is accompanied by slight adiabatic warming away from the center.

For drag friction and no heating, the results that the tangential wind decreases from 37 to 18 m/sec in 8 hours, the frictionally induced vertical motion destroys the warm core, and the average kinetic energy dissipation rate is 6 watts $m^{-2}$ are consistent with those expected for a dissipating hurricane over land.

### 4.2 The Role of Internal Mixing

The proper formulation of internal mixing (both horizontal and vertical) is an important, but unfortunately poorly understood aspect of numerical modeling. Because of the difficulty in making direct measurements, the dissipation of kinetic energy by internal mixing is usually estimated as a residual in empirical energy budgets, e.g., Riehl and Malkus (1961), Hawkins and Rubsam (1968). These studies indicate that the kinetic energy dissipation by internal mixing is about the same magnitude as the dissipation at the surface.

The horizontal diffusion of momentum in the hurricane has been modeled using constant mixing coefficients, but the values used by different investigators (table 1) vary over several orders of magnitude. A further complication is that the truncation errors of the finite difference schemes produce large, non-linear damping.

The vertical mixing process is even more complex than horizontal mixing, because the vertical eddies (cumulus clouds) have the same vertical scale as the hurricane. Gray (1967) has found that the momentum transport by cumulus convection is an important process in the steady-state dynamics of hurricanes. Constant vertical mixing coefficients seem particularily inadequate to describe this process correctly. Indeed, Gray finds a large variation of the vertical mixing coefficients with height ranging from $10^6$ to $10^9$ $cm^2$ $sec^{-1}$.

Because of these uncertainties, the effects of horizontal and vertical mixing are investigated in Experiments 3 through 6. The steady heating for these experiments, shown in figure 9, is defined by the rainfall profile A figure 3 and the solid vertical profile in figure 4. The results from these first experiments provide values of the mixing coefficients for use in later experiments in which the heating distribution was varied.

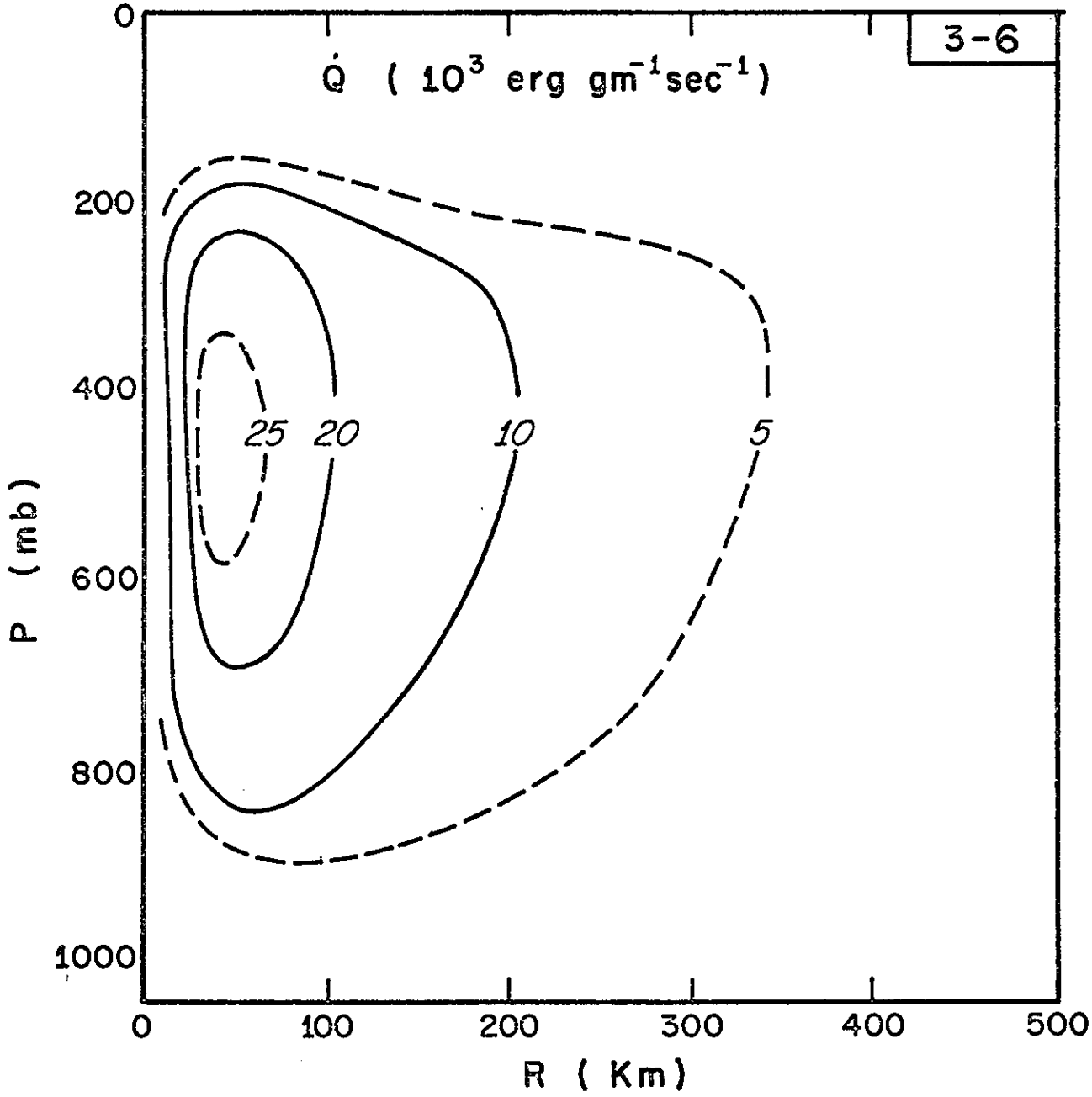


Figure 9. Cross section of latent heat release for Experiments 3-6

Table 1. Exchange Coefficients ($cm^2 sec^{-1}$) in Hurricanes

| Investigator | $K_H$ | $K_z$ | Remarks |
|---|---|---|---|
| Estoque and Partagas (1968) | $10^8 - 10^9$ | - | Forecast model* |
| Gray (1967) | - | $10^6$-$10^9$ | Empirical study |
| Kasahara (1961) | $1.6 \times 10^8$ | - | Forecast model* |
| Krishnamurti (1961) | $2.7 \times 10^9$ | $1.2 \times 10^7$ | Diagnostic study |
| Kuo (1965) | $10^8$ | $10^5$-$10^6$ | Forecast model |
| Ooyama (1969) | $10^7$ | 0 -$10^5$ | Forecast model* |
| Riehl and Malkus (1961) | $10^8$ | $10^6$ | Empirical study |
| Rosenthal (1969) | $10^8$ | 0 -$10^5$ | Forecast model* |
| Yamasaki (1968a,b) | $10^7$ | $10^5$ | Forecast model* |

* Denotes additional non-linear damping due to truncation error in finite difference scheme.

4.2.1 Evolution to Slowly Varying State: Experiment 3

In Experiment 3 the effects of a very large amount of horizontal mixing ($K_H = 25 \times 10^8$ $cm^2 sec^{-1}$) and little vertical mixing ($K_z = 0.5 \times 10^6$ $cm^2 sec^{-1}$) are investigated. For this first heating experiment, some details of the evolution to the quasi-steady state are presented. In later experiments, only the final state is emphasized.

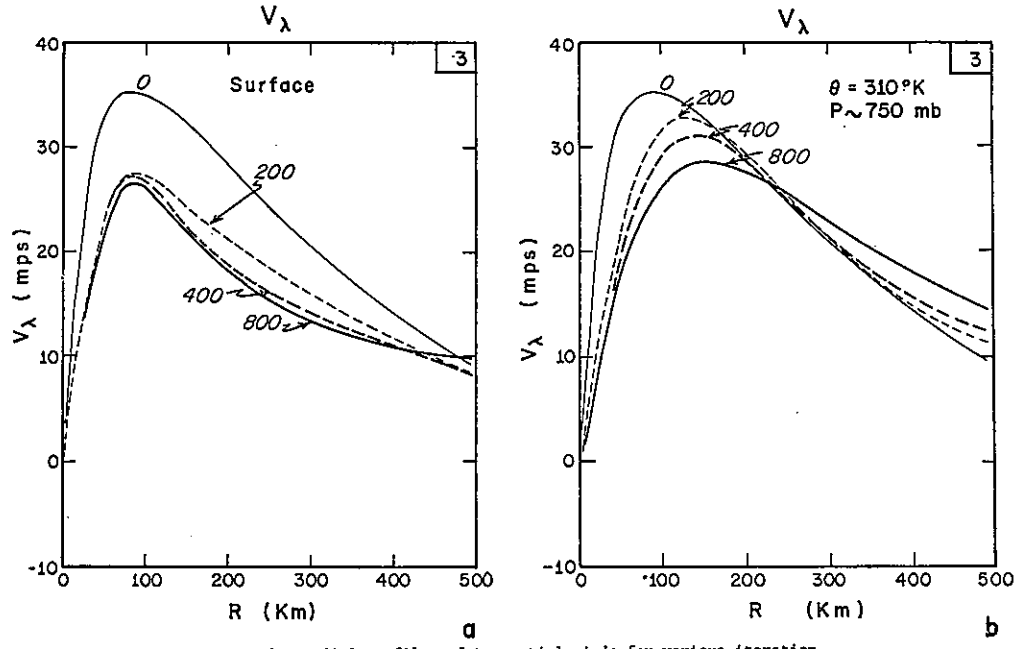


Figure 10. Radial profiles of tangential winds for various iteration steps in Experiment 3

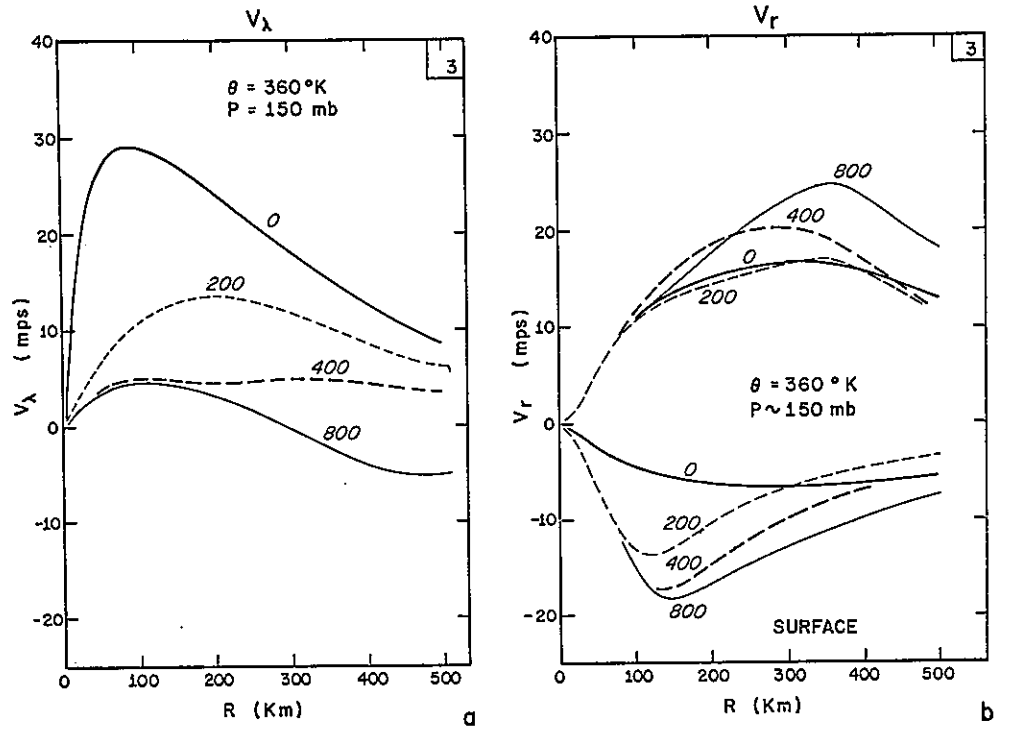


Figure 11. Tangential and radial wind profiles in Experiment 3

Momentum and Temperature Profiles. In figures 10 and 11, the radial profiles of the wind components at several levels at 0, 200, 400, and 800 steps illustrate the evolution of the slowly varying state. The initial changes in the velocity profiles are very large. Although a completely steady state is not attained by the end of the iteration at 800 steps, the changes are sufficiently small to justify meaningful comparisons between these preliminary experiments.

There are three interesting features in the evolution of the tangential wind profile: First is the relatively rapid transition of the upper level cyclonic winds to anticyclonic beyond 300 km (fig. 11a). Second is the gradual outward diffusion of the middle level cyclonic wind maximum (fig. 10b). Third is the maintenance of the sharp wind maximum at the surface, although the maximum is reduced from 37 to 26 m/sec.

The evolution of the radial winds (fig. 11b) shows an increase in both the upper level outflow and lower level inflow with a tendency toward sharper extrema. The radial motion in the middle levels remains relatively weak.

In figure 12 the isentropic cross section shows considerable warming in the upper levels where the heating is a maximum. The initial temperature difference of $1^{\circ}C$ between the center and 500 km increases to about $10^{\circ}C$ at 300 mb.

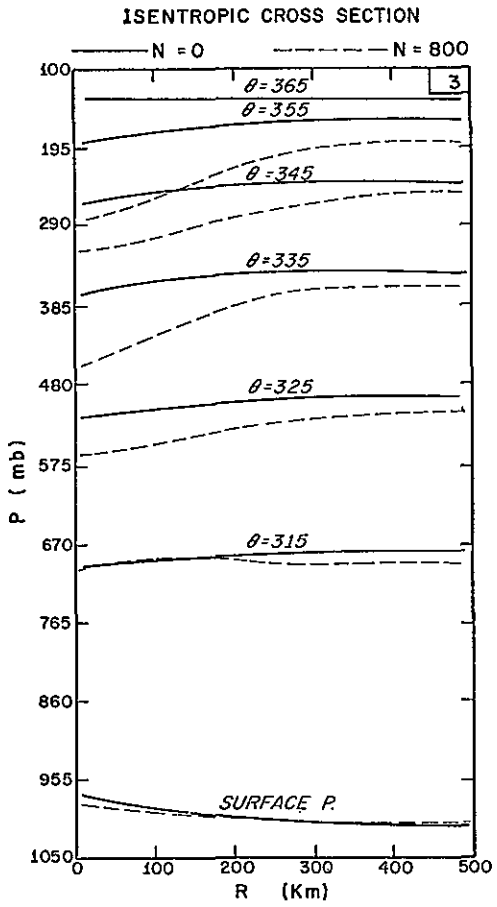


Figure 12. Isentropic cross section for initial and slowly varying state in Experiment 3

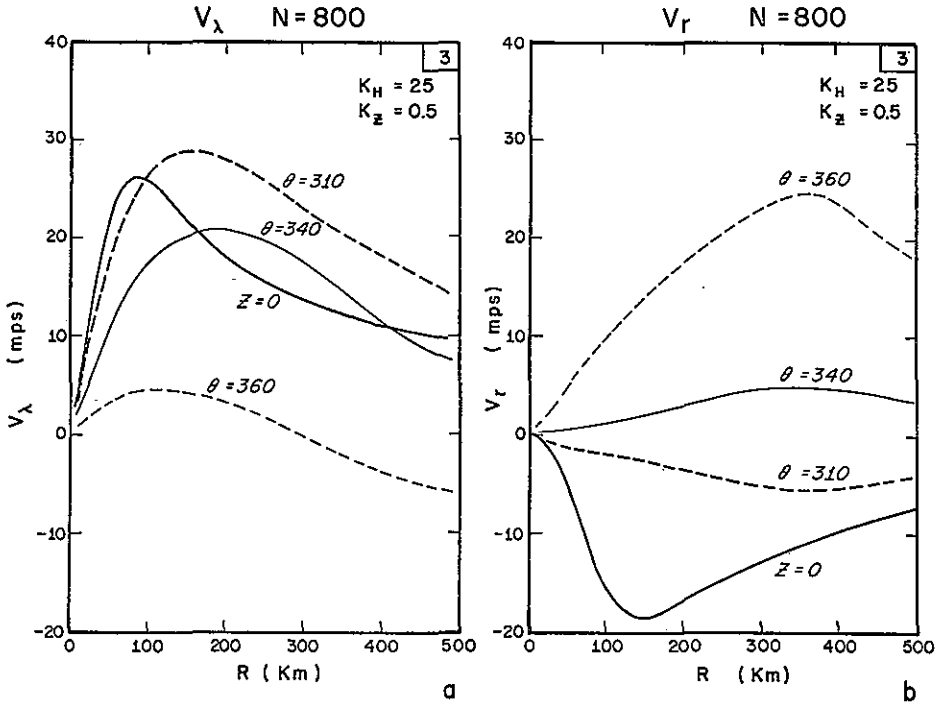


Figure 13. Tangential and radial wind profiles in Experiment 3

In the lower troposphere there is little change, although there is a tendency for slight cooling around 700 mb.

The evolution of the mass and momentum fields is explained by examining the important physical processes in various regions of the storm. Figure 13 illustrates tangential and radial winds after 800 iterations. Profiles for the middle layers show that the large amount of horizontal mixing diffuses the tangential wind maximum outward. At the surface, however, the sharp maximum is maintained as the advection of angular momentum by the strong inflow counters the opposite effect of the lateral diffusion. In the upper levels, the outflow advects air with low angular momentum outward so that the initial cyclonic circulation becomes anticyclonic. Inside 200 km, the upward transport of momentum by the heating maintains a reasonable vertical shear. In the middle levels beyond 200 km, however, radial and vertical advection of momentum is small. Because the vertical mixing is negligible in this experiment, only horizontal mixing disturbs the gradient balance in this region. This process is relatively slow and large vertical shear develops beyond 200 km (fig. 13a). This weak vertical coupling in tropical systems outside of convective areas has been discussed by Charney (1963).

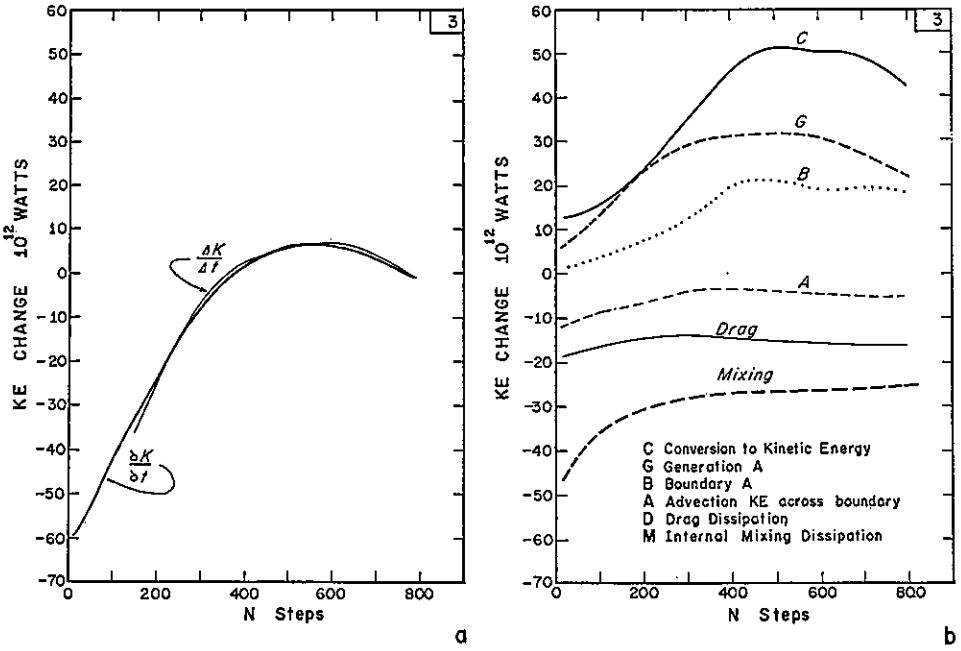


Figure 14. Energy transformation rates in Experiment 3

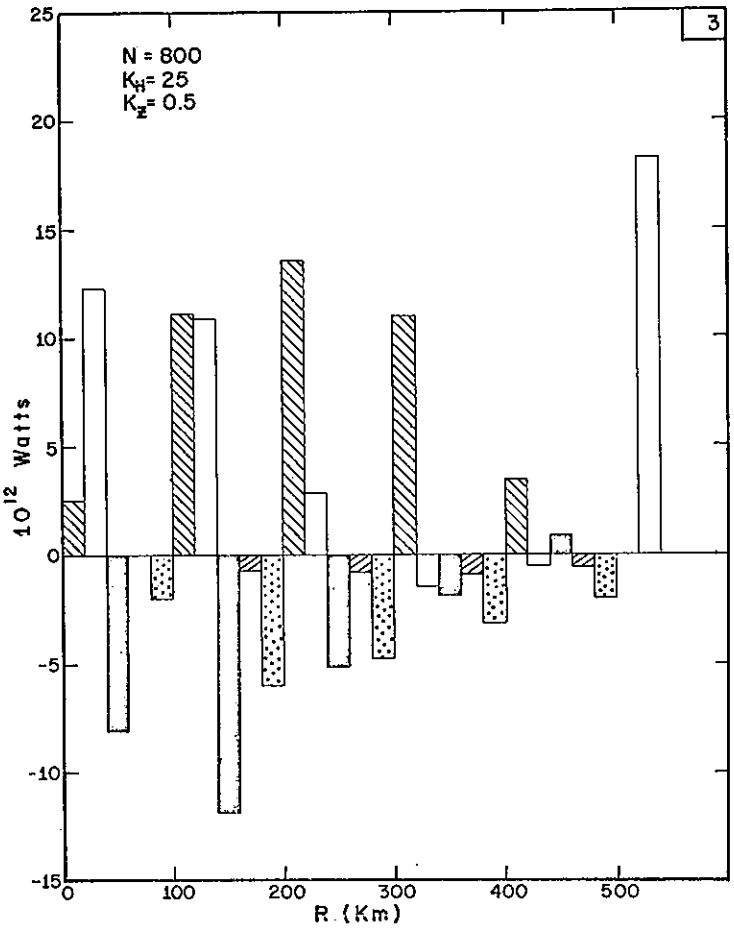


Figure 15. Energy budget in Experiment 3 (see fig. 33 for key)

The large amount of horizontal mixing produces the diffuse warm core shown in the isentropic cross section (fig. 12). Although the magnitude of the temperature anomoly is reasonable, the horizontal temperature gradient is nearly constant out to 300 km. Observations of hurricane structure show a more concentrated warm core.

Energy Budget. Figure 14b shows the evolution of the different components of the rates of change of available potential and kinetic energy. Initially the dissipation by horizontal mixing is dominant, causing a large negative kinetic energy tendency. After 400 steps the internal mixing remains relatively constant. Throughout the entire experiment the dissipation from surface drag is smaller than that from internal mixing.

One of the most interesting features of the energy budget evolution is the relationship between changes in the generation and boundary flux of available potential energy and its conversion to kinetic energy. Although energetic consistency requires only that these changes be equal in the steady-state, there is an extremely close correlation between the two at all stages of all the experiments. This suggests that the available energy generated by the steady forcing is almost immediately converted to kinetic energy.

Initially the kinetic energy conversion closely follows the generation. After 300 steps, however, the mass outflow is removing heat at 500 km which would otherwise reduce the radial temperature gradient. This process is reflected in an increase in the boundary term, B, of the available energy change equation. The sum of the generation and boundary terms continue to almost exactly balance the conversion to kinetic energy, so that changes in the store of available potential energy are small.

Although the boundary term in the available energy budget is large, the boundary flux of kinetic energy is rather small compared to the conversion and dissipation processes within the volume. The contribution is relatively constant and is negative, indicating that the storm is exporting kinetic energy to the environment.

The contribution by the various energy transformation processes within 100 km radial rings is presented in figure 15. Most of the generation occurs inside 200 km while its conversion to kinetic energy occurs primarily between 100 and 300 km. The large contribution to the available energy budget by the boundary processes is interesting and supports earlier studies which show that the hurricane cannot be considered a closed system on this scale.

The most important dissipative process in Experiment 3 is lateral mixing, which is expected in view of the large value of $K_H$. Dissipation from surface friction is nearly independent of radius. Vertical mixing dissipation is an order of magnitude smaller than the horizontal and surface dissipation, indicating that it is negligible for $K_z$ equal to $0.5 \times 10^6$ $cm^2 sec^{-1}$.

The total energy budget for Experiment 3 is shown in table 2. These results may be compared with estimates from observational studies of hurricanes summarized in table 3. The large kinetic energy conversion rate in Experiment 3, in spite of the weak maximum wind, is related to the large horizontal mixing which tends to diffuse the momentum laterally and produce a large vortex.

Table 2. Energy Transformation Rates ($10^{12}$ watts)

| Experiment | 3 | 4 | 5 | 6 | 7 | 8 | 10 | 11 | 12 | 13 | 16 |
|---|---|---|---|---|---|---|---|---|---|---|---|
| Rainfall profile type | A | A | A | A | B | C | B | ½B | B | B | B |
| Vertical profile p=pseudo-adiabatic c=cloud-environment | C | C | C | C | C | C | P | C | C | C | C |
| $K_H$ ($10^8$ $cm^2 sec^{-1}$) | 25. | 10. | 10. | 5. | 5. | 5. | 5. | 5. | 5. | 5. | 2.5 |
| $K_z$ ($10^6$ $cm^2 sec^{-1}$) | 0.5 | 1. | 5. | 5. | 5. | 5. | 5. | 5. | 5. | 5. | 5. |
| Generation A | 24.1 | 21.2 | 15.5 | 17.3 | 10.7 | 4.8 | 2.9 | 13.7 | 13.8 | 14.6 | 9.9 |
| Boundary A | 18.2 | 17.0 | 13.3 | 14.6 | 4.2 | 0.1 | 1.1 | 5.0 | 2.4 | 2.5 | 3.5 |
| Conversion to K | 42.0 | 39.2 | 30.3 | 32.9 | 16.5 | 6.2 | 5.3 | 18.8 | 18.6 | 19.0 | 15.1 |
| Boundary K | -5.0 | -4.3 | -2.2 | -2.2 | 0.0 | 0.0 | 0.0 | 0.0 | -0.1 | -0.1 | -0.2 |
| Drag dissipation | -18. | -22. | -15. | -14. | -9.2 | -7. | -5. | -11. | -9.4 | -9.8 | -12. |
| Lateral mixing | -26. | -16. | -12. | -6.8 | -5.7 | -5. | -3. | -5.8 | -5.9 | -6.0 | -4.2 |
| Vertical mixing | -2.5 | -6.0 | -18. | -15. | -11. | -5. | -5. | -10. | -13. | -13. | -13. |

Table 3. Empirical Energy Budgets

| Investigation | Region of Storm (km) | Heating $10^{14}$ watts | Gen A | Conv K | Adv K $10^{12}$ | Sfc Disp. watts | Int Disp. |
|---|---|---|---|---|---|---|---|
| Anthes + Johnson (1968) | 0-1000 | 3.2 | 10.3 | - | - | - | - |
| Hawkins + Rubsam (1968) | 0-150 | 2.2 | - | 2.3 | 3.9 | -4.2 | -2.0 |
| Hughes (1952) | 0-444 | 5.4 | - | - | - | - | - |
| Miller (1962) | 0-111 | 3.6 | - | 8.0 | 2.4 | -5.1 | -5.3 |
| Palmén + Jordan (1955) | 0-666 | 5.4 | - | 15.0 | - | - | - |
| Palmén + Riehl (1957) | 0-666 | 5.0 | - | 15.0 | 0.0 | -13. | 0.0 |
| Riehl + Malkus (1961) 8/25 | 0-150 | 2.1 | - | 2.8 | 0.3 | -1.6 | -1.0 |
| 8/27 | 0-150 | 4.0 | - | 6.8 | 3.5 | -3.2 | -6.6 |

Truncation Error. The difference between observed rates of change in the total kinetic energy of the volume and the instantaneous tendencies computed from (38) is an estimate of the truncation error in the model. The tendencies as a function of iteration step and the observed changes evaluated over 100 steps, shown in figure 14a, show generally good agreement with little systematic deviation. Maximum differences are about 10 percent, indicating that truncation error is small.

Although the results from Experiment 3 were not particularly realistic because of the large amount of horizontal mixing, the transient features of the evolution to the slowly varying state have indicated some of the general characteristics of the model. A horizontal mixing coefficient of 25 x $10^8$ $cm^2 sec^{-1}$ produces an unrealistically diffuse storm with a very large radius of maximum wind. In addition, the generation, the conversion of available potential energy to kinetic energy, and the dissipation by lateral mixing are too large compared with empirical results.

4.2.2 Slowly Varying States of Mixing: Experiments 4 through 6

Because the large, diffuse vortex in Experiment 3 indicates that the horizontal mixing is overestimated and the vertical mixing is underestimated, the horizontal and vertical mixing coefficients are varied in Experiments 4 through 6. The horizontal mixing coefficient is decreased from 25 x $10^8$ to 5 x $10^8$ $cm^2 sec^{-1}$, and the vertical mixing coefficient is increased from 0.5 x $10^6$ to 5.0 x $10^6$ $cm^2 sec^{-1}$. All other parameters are held constant.

Momentum and Temperature Profiles. The radial profiles of the tangential and radial winds after 800 iterations and the isentropic cross sections for Experiments 4, 5, and 6 are shown in figures 16 through 21. It is evident from these

figures that the results become more realistic as $K_H$ decreases and $K_z$ increases. The tangential wind maximum increases from 28 to 38 m/sec, and the warm core becomes more concentrated as $K_H$ is reduced (fig. 17, 19, and 21). Differences in the radial wind profiles are less (fig. 16b, 18b, and 20b) because the effects of decreasing $K_H$ are partially counteracted by increasing $K_z$.

As $K_z$ is increased, vertical mixing reduces the vertical shear of the tangential wind, and the radial tilt of the maximum wind axis becomes less. It is difficult, however, to determine how much positive vertical shear in the lower 300 mb is reasonable. In a series of separate boundary layer experiments (app. A) the surface wind beyond the radius of maximum wind is subgradient by as much as 50 percent because of surface friction. This results in a substantial positive wind shear in the lower levels. Thus part of the large shear may be caused by insufficient vertical resolution of the boundary layer.

Although non-linear computational instability occurs in the boundary layer experiments (app. A) for $K_H$ equal to $10 \times 10^8$ $cm^2 sec^{-1}$, only a faint suggestion of oscillations in the radial wind profile appears in the complete model experiments, even though $K_H$ is reduced to $5 \times 10^8$ $cm^2 sec^{-1}$ (figure 20b). This probably results from the additional damping effect of vertical mixing and the interaction between

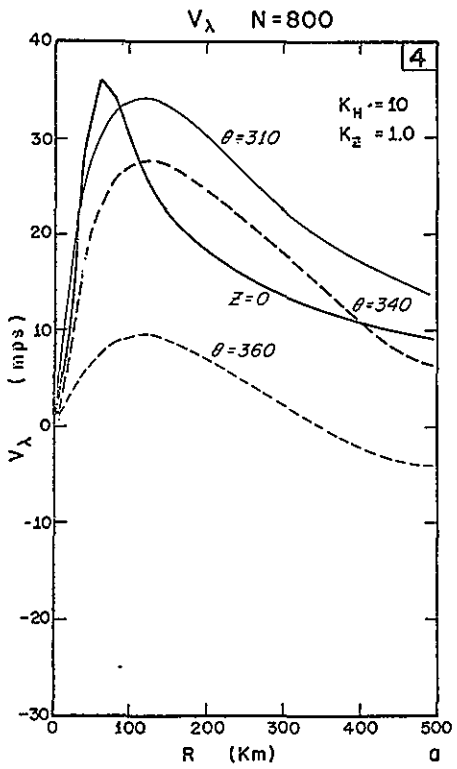


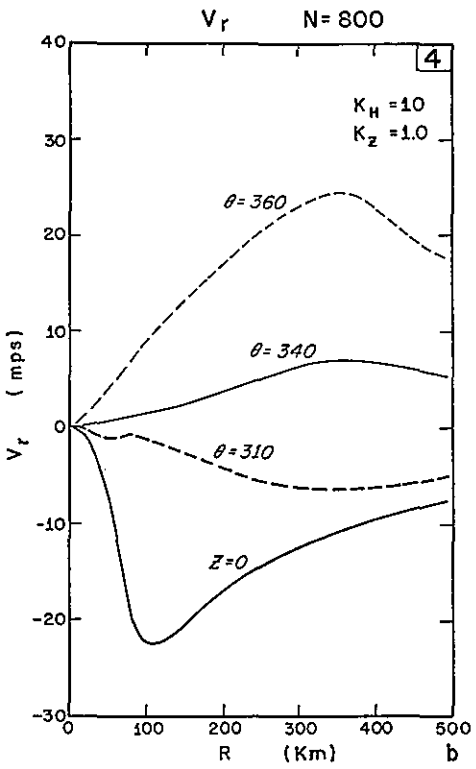


Figure 16. Tangential and radial wind profiles in Experiment 4

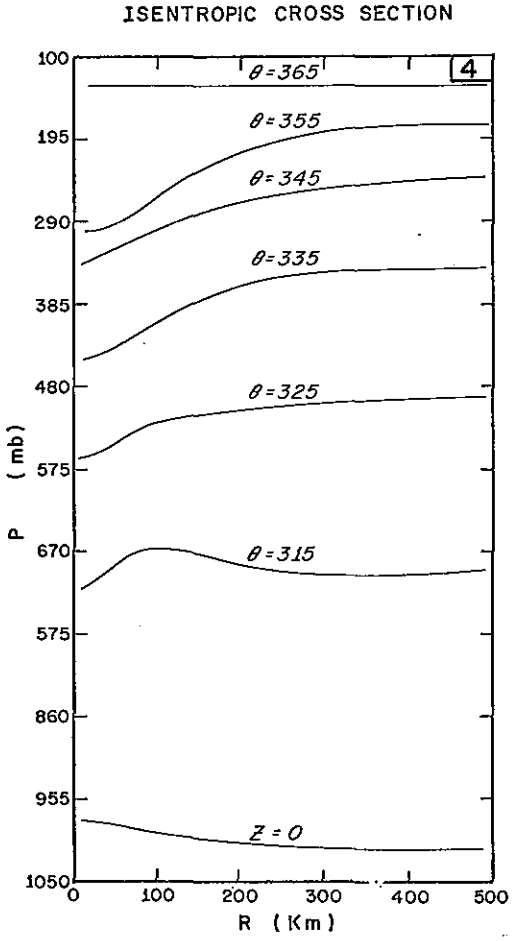


Figure 17. Isentropic cross section for Experiment 4

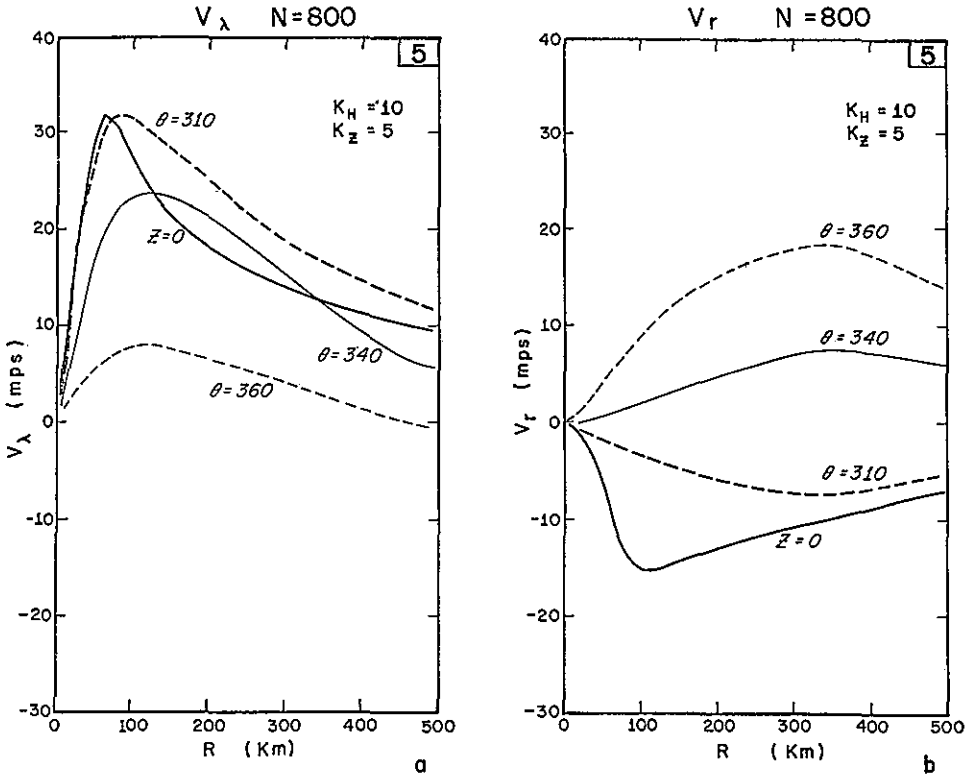


Figure 18. Tangential and radial wind profiles in Experiment 5

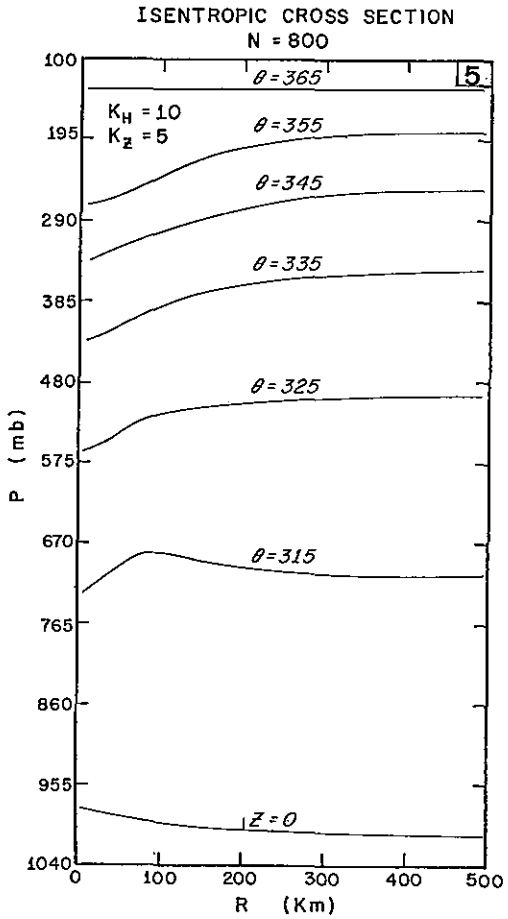


Figure 19. Isentropic cross section for Experiment 5

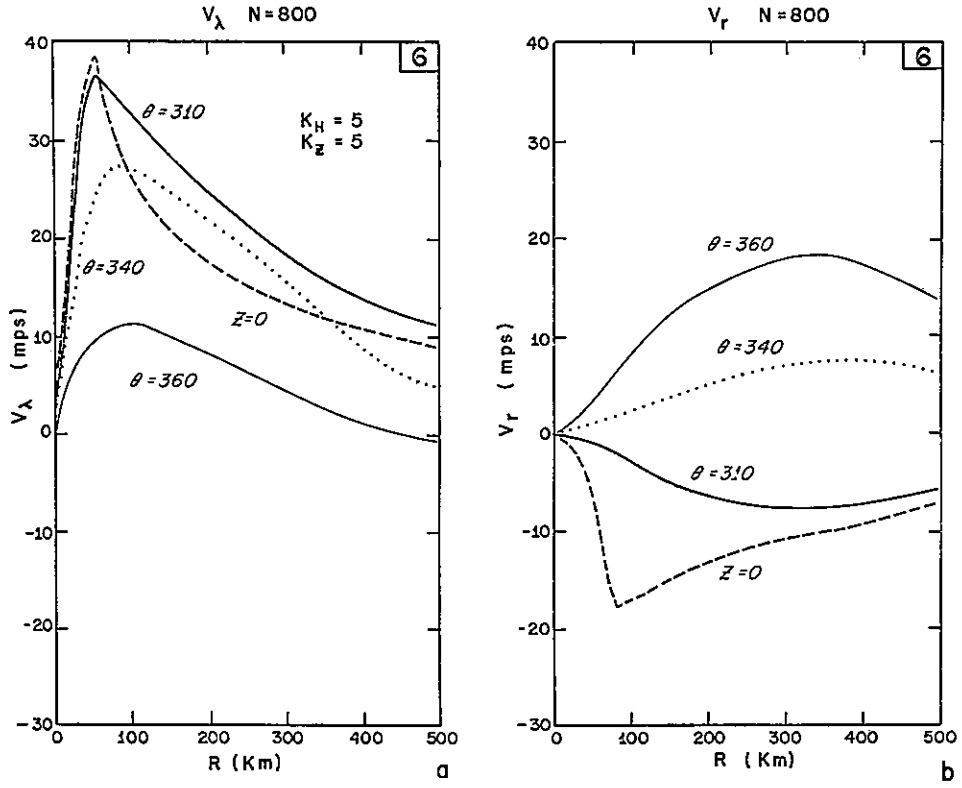


Figure 20. Tangential and radial wind profiles for Experiment 6

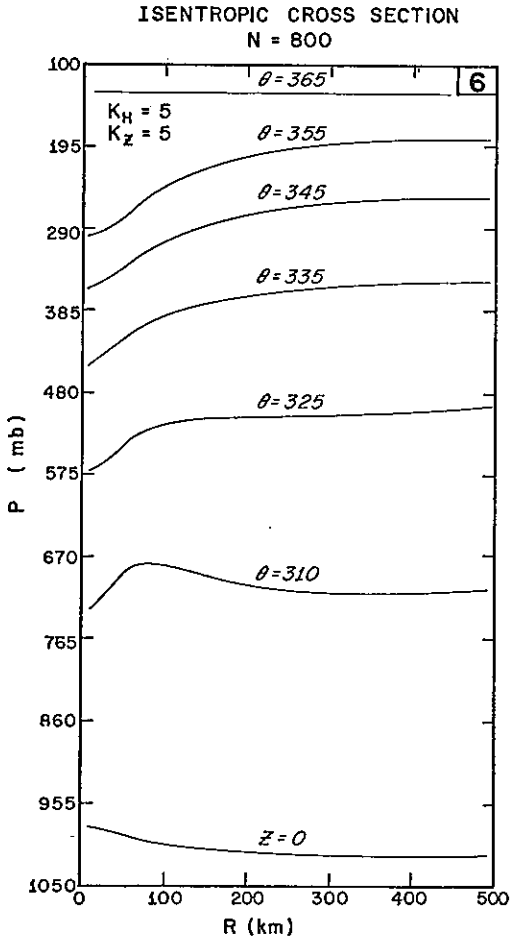


Figure 21. Isentropic cross section for Experiment 6

the velocity and mass fields in the complete model.

Energy Budget. The energy budgets for Experiments 4, 5, and 6 by 100 km rings are shown in figures 22 through 24 and the total energy budgets are summarized in table 2. Decreases in $K_H$ and increases in $K_z$ are accompanied by corresponding decreases and increases in horizontal and vertical mixing dissipation respectively. Drag dissipation remains relatively constant because the increased maximum winds occur over a smaller area. The generation of available energy and conversion to kinetic energy decrease toward more realistic values (table 3) as the storm becomes more concentrated.

### 4.2.3 Summary

The results from Experiments 3 through 6 establish ranges of the horizontal and vertical mixing coefficients which give fairly reasonable results. Values of $K_H$ greater than or equal to $10 \times 10^8$ $cm^2 sec^{-1}$ are too high, resulting in a large, diffuse storm. Values of $K_z$ less than or equal to $1 \times 10^6$ $cm^2 sec^{-1}$ do not yield sufficient vertical mixing to produce reasonable vertical shears of the tangential winds. The most realistic results are obtained for $K_H$ equal to $5 \times 10^8$ $cm^2 sec^{-1}$ and $K_z$ equal to $5 \times 10^6$ $cm^2 sec^{-1}$. Both values are possibly on the high side, but in view of the threat of non-linear instability if smaller values are used, we prefer to begin the study of variable heating functions with these values.

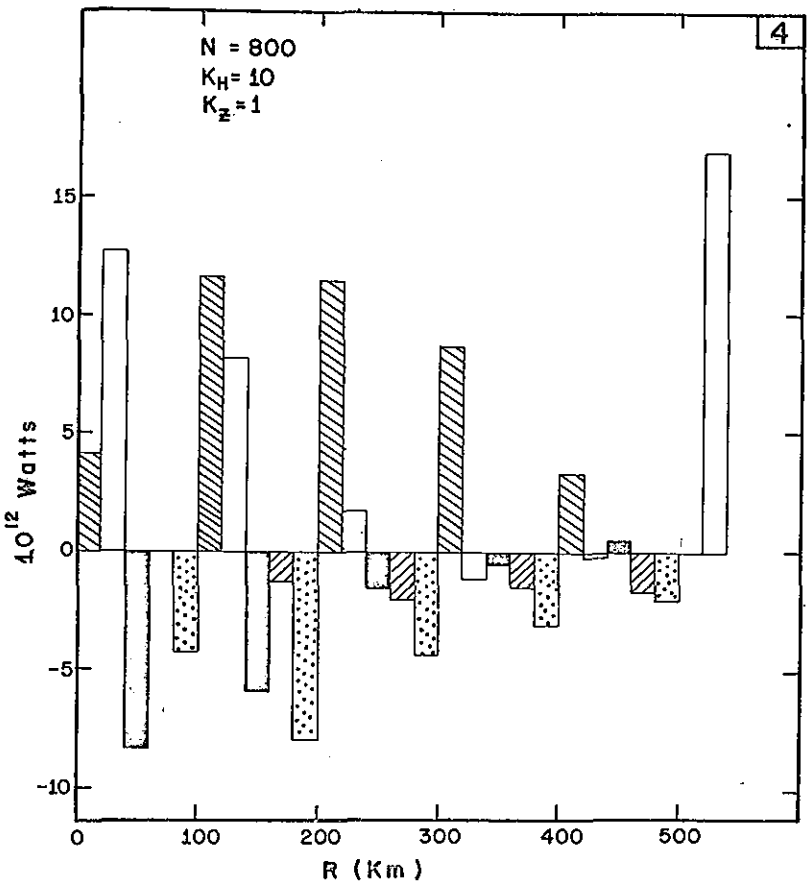


Figure 22. Energy budget for Experiment 4 (see fig. 33 for key).

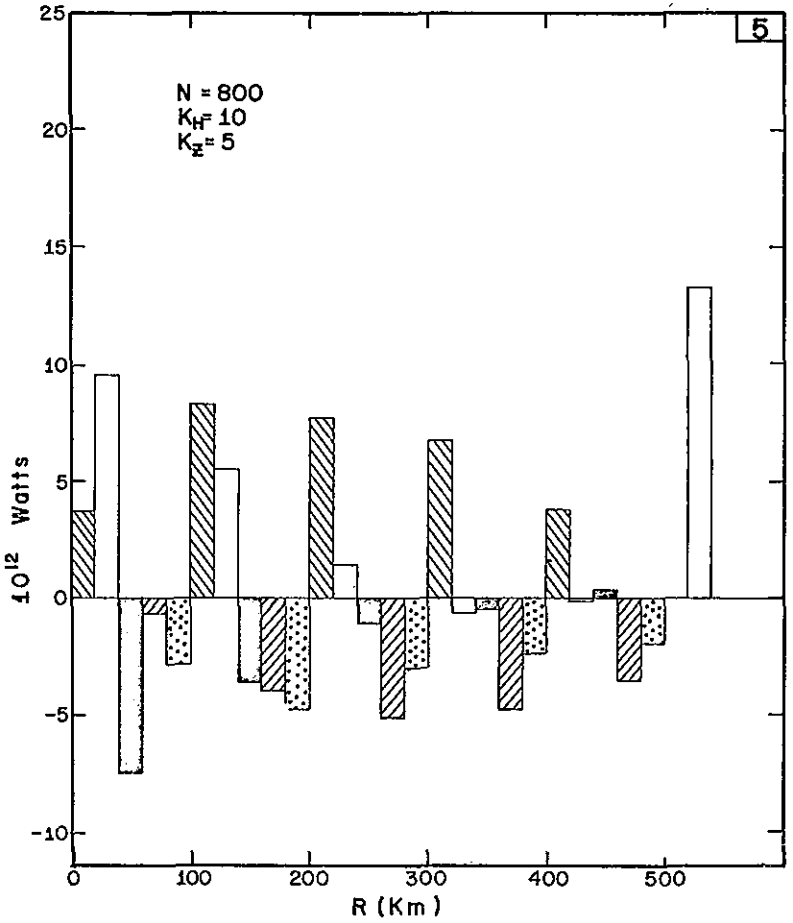


Figure 23. Energy budget for Experiment 5 (see fig. 33 for key).

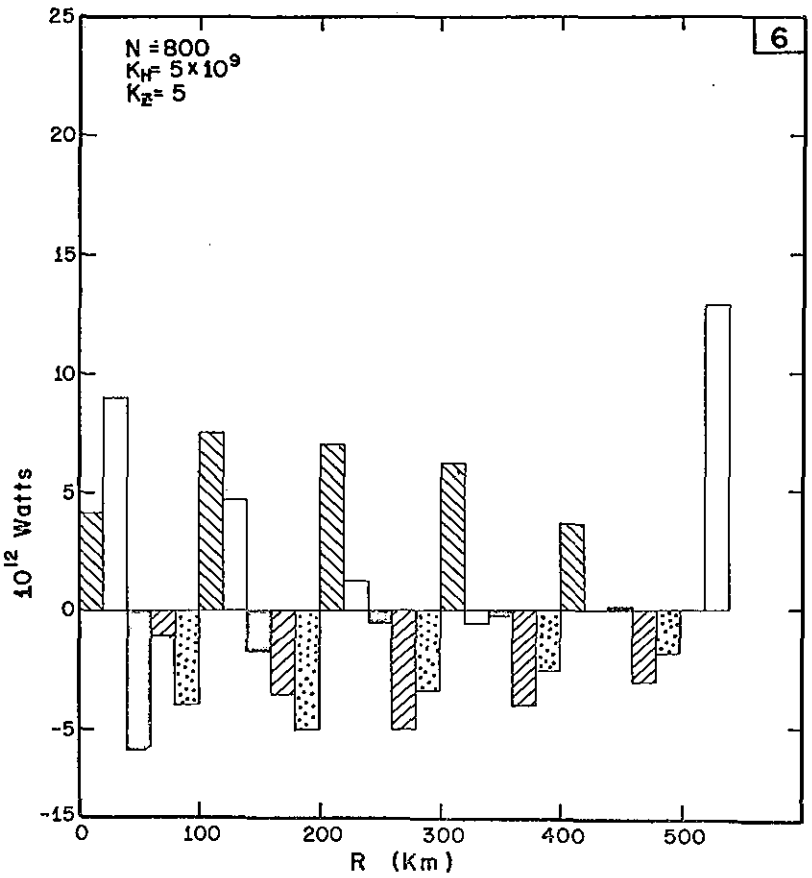


Figure 24. Energy budget for Experiment 6 (see fig. 33 for key).

## 4.3 The Role of Variable Distributions of Heating

From the premise of the thermal forcing of the hurricane, difference between size and intensity of individual storms must be related to space and time variations of the heating distributions. However, the question of just how sensitive or responsive is the storm circulation to these variations remains unanswered.

From the continuity equation one expects that the radial circulation is highly dependent on the horizontal and vertical heating distributions. The response of the tangential circulation is more complex. However, the supposition that the time response of the total circulation to changes in thermal forcing is relatively rapid underlies the justification for hurricane modification experiments. In this section the results of the model attained from various combinations of horizontal and vertical heating distributions provide some insight into this relation between the hurricane circulation and thermal forcing.

4.3.1. Radial Variation of Latent Heating

The heating function in Experiment 6 (discussed in sec. 4.2.2.) produces a rather large storm of only moderate intensity. The total heat release, generation of available energy, and conversion to kinetic energy are larger than empirical results by a factor of two or three. These results suggest that the heating function overestimates the latent heat release at large distances from the center.

In Experiments 7 and 8 the latent heat release beyond 100 km is progressively decreased with the result that the relative heating becomes more concentrated near the center (rainfall types B and C in table 4 and fig. 3). In Experiment 9, the primary heating maximum at 30 km is reduced slightly and a secondary heating maximum is introduced at 200 km to simulate the effect of rainbands (rainfall type D in table 4 and fig. 3). In all four experiments the vertical heating distribution is specified by the solid curve in figure 4.

Table 4. Summary of Experiments Investigating Radial Variation of Heating

| Experiment | Rainfall Type | Total Heating rate $10^{14}$ watts |
|---|---|---|
| 6 | A | 21.3 |
| 7 | B | 11.0 |
| 8 | C | 5.5 |
| 9 | D | 11.0 |

Concentrated Heating Near the Center: Experiment 7. In all experiments with 20 km resolution and a time step of 30 seconds, the large-scale changes, especially in the inner 300 km region, were small enough after 1600 iterations (13.3 hours) to justify meaningful comparisons of the slowly varying state. Before the discussion of the steady-state solutions, quantitative results illustrating the convergence to a steady-state are presented for one experiment. The variation of $L_2$ (34) on the tangential and radial winds is shown only for Experiment 7 because the behavior of the norms in the other experiments is quite similar.

In figure 25 the convergence of the tangential winds is most rapid in the lower levels near the center. Inside 200 km, the tangential wind has reached a slowly varying state after 800 iterations. In the upper levels, however, at large

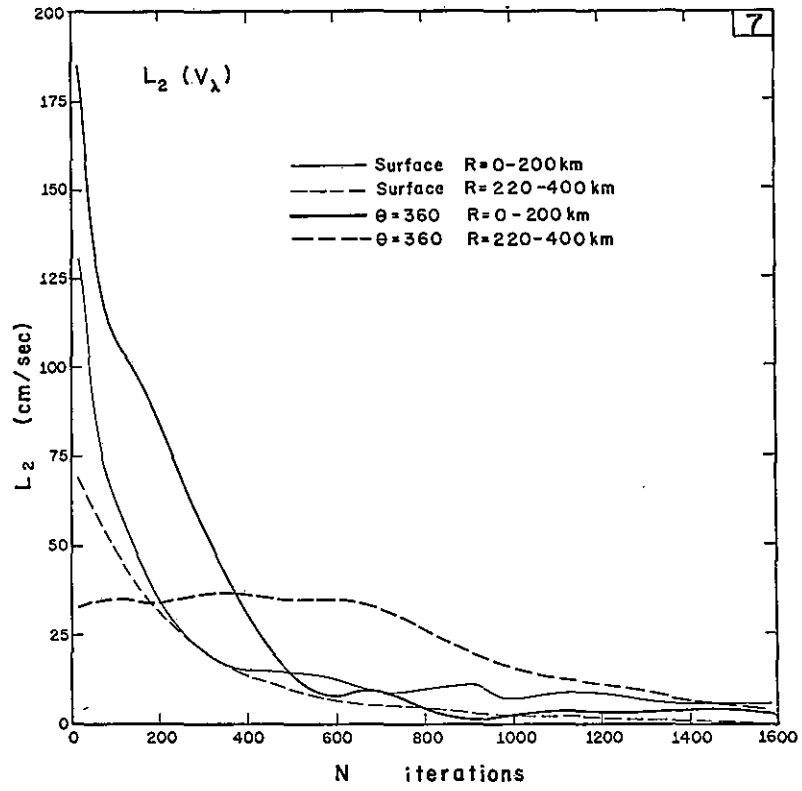


Figure 25. Time variation of $L_2$ norm on tangential wind in Experiment 7

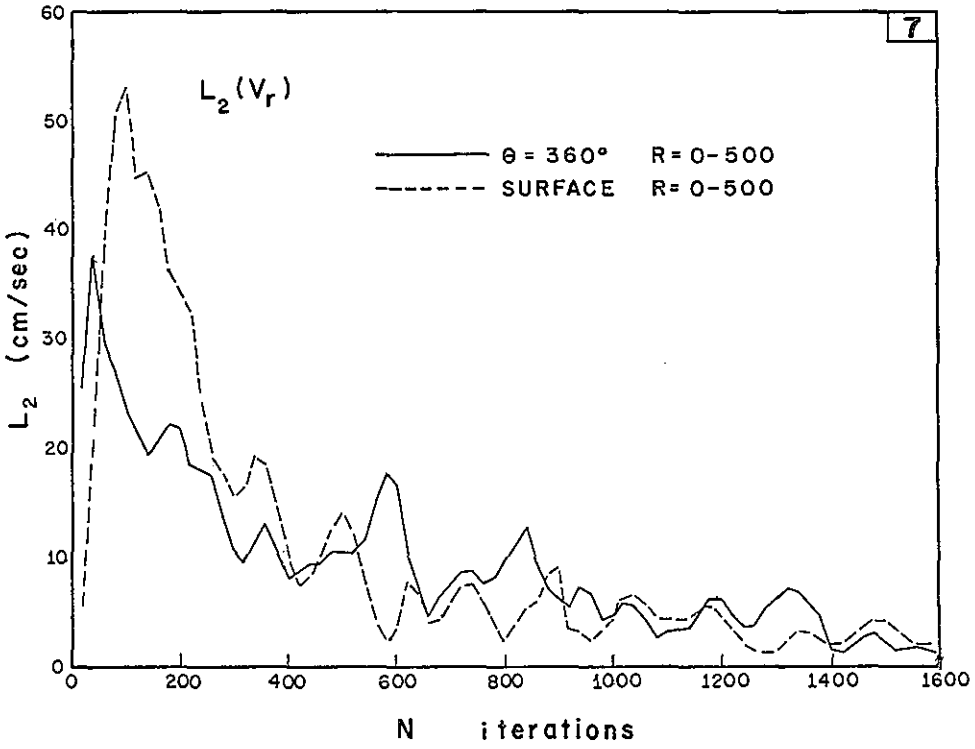


Figure 26. Time variation of $L_2$ norm on radial wind in Experiment 7

distances from the center, convergence is much slower. In fact, $L_2$ ($v_\lambda$ ) at 360°K does not be begin to decrease until the inner region reaches a quasi-steady-state (about 600 iterations). The physical explanation is that the inner region adjusts rather quickly to the heating function. In the outer region, the heating is either small or zero, thus the winds are influenced only by advection and mixing. In the upper levels, internal mixing is negligible, so that only horizontal advection is important. Because the radial advection is outward at this level the tangential winds in the outer regions are primarily determined by the steady-state angular momentum distribution near the center. The slow convergence in this region reflects the time required for the angular momentum near the center to be advected to the edge of the domain.

The convergence of the $L_2$ norm on the radial winds for the surface and 360°K is shown in figure 26. The oscillations superimposed on the downward trend are evidence of the inertial gravity waves mentioned in Experiment 2. The frequency of these waves is apparently low enough to avoid most of the damping in Matsuno finite difference scheme.

Momentum and Temperature Structure. In Experiment 7 (rainfall type B, fig. 3) the total heating rate is reduced from 21.3 to 11.0 x $10^{14}$ watts, a rate closer to empirical results (table 2). The more concentrated heating function in this experiment generates a smaller warm core with nearly as intense a pressure gradient near the center as the one in Experiment 6. The tangential and radial wind profiles are shown in figure 28 and may be compared with those from Experiment 6 in figure 27. The effect of reducing the heating beyond 150 km on the tangential wind is to slightly decrease the maximum wind from 34 to 33 m/sec at 60 km. However, the winds beyond 150 km decrease significantly. The 3 percent decrease in the maximum wind speed, in spite of a 50 percent reduction in total heating is somewhat paradoxical and emphasizes the importance of differential heating in establishing the temperature and pressure gradients and the angular momentum distribution.

The changes in the radial winds are greater than those in the tangential winds (fig. 27b, 28b). The inflow is reduced beyond 200 km; e.g., from 11 to 8 m/sec at 250 km. The maximum outflow decreases from 19 to 14 m/sec and the radius of maximum outflow moves inward from 360 to 180 km.

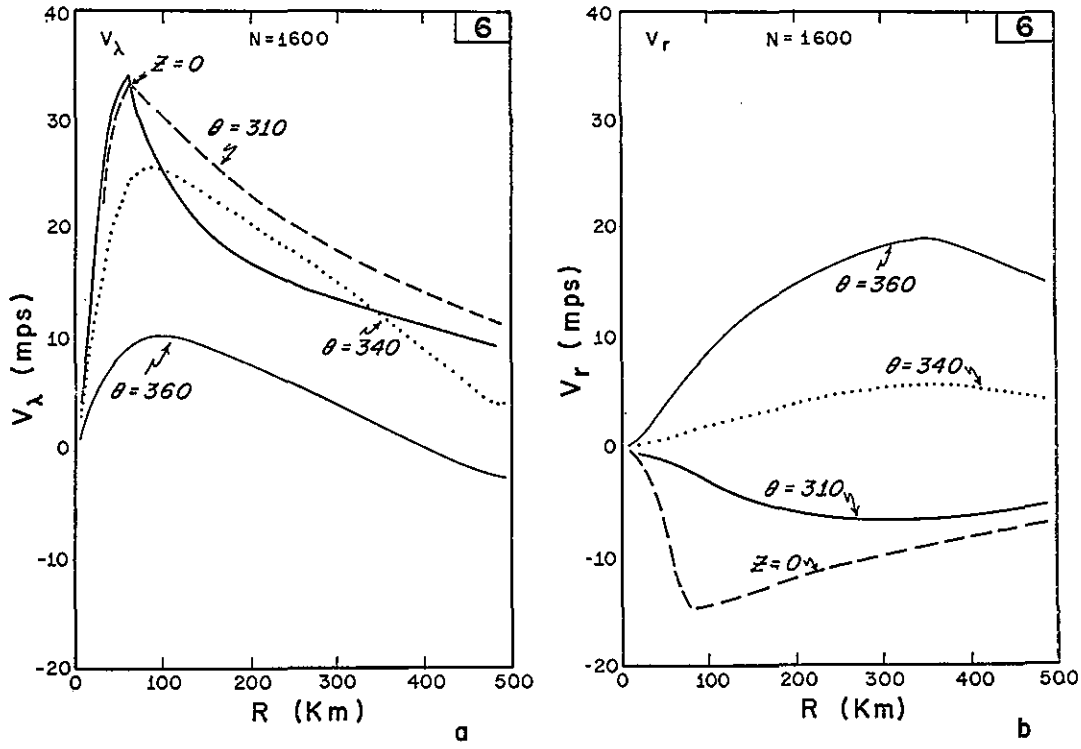


Figure 27. Tangential and radial wind profiles in Experiment 6

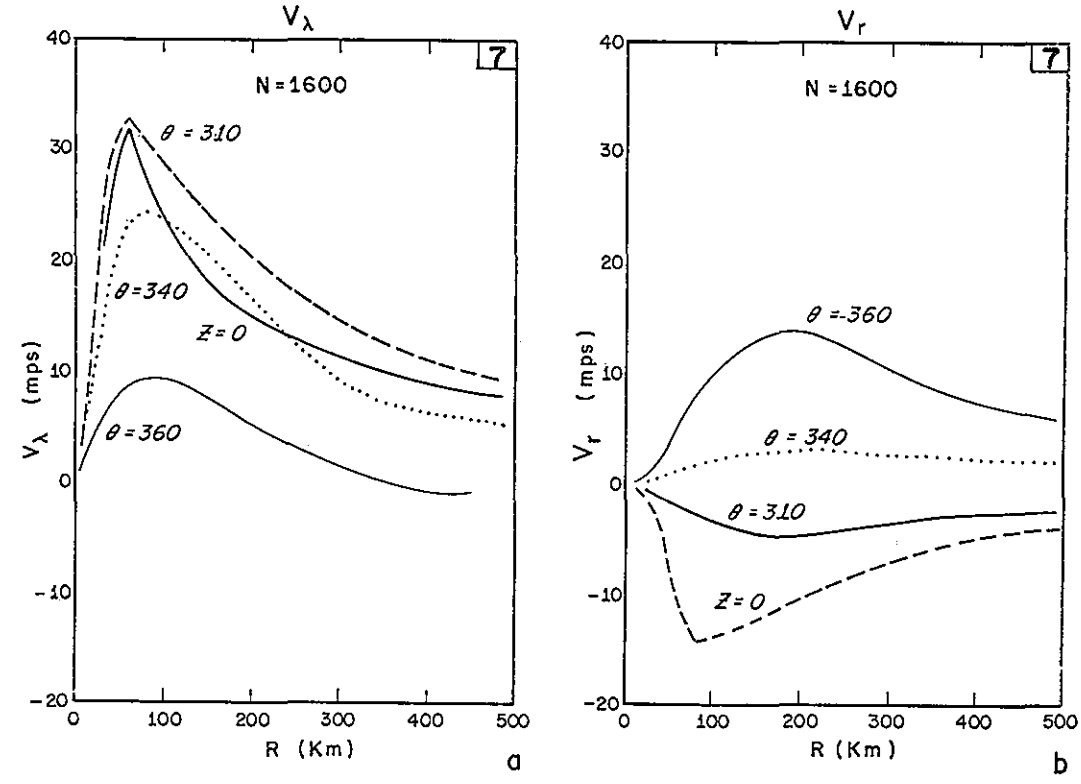


Figure 28. Tangential and radial wind profiles for Experiment 7

Because the results from Experiment 7 are quite realistic, they are presented in some detail. The tangential wind cross section, figure 29, shows a region of maximum cyclonic winds near the center with little vertical wind shear below 300 mb. In the lower levels beyond the radius of maximum wind, positive vertical shear exists because of surface friction. A small region of anticyclonic winds occurs in the upper levels beyond 400 km.

The radial wind cross section, figure 30, shows inflow from the surface to about 600 mb, although significant ( $|v_r| \geq 5$ m/sec) inflow is limited to the region below 800 mb. The maximum inflow of 15 m/sec is somewhat stronger than empirical observations (e.g., Miller, 1962), but weaker than the inflow found in the separate boundary layer experiments (app. A). Significant outflow occurs above 300 mb.

Generation and Conversion of Available Potential Energy. The vertical cross sections of the generation and its conversion to kinetic energy for Experiment 7 are shown in figures 31 and 32. Most of the generation occurs in the middle and upper troposphere inside 150 km, a result which agrees well with the empirical estimate of Anthes and Johnson (1968). Conversion of available to kinetic energy, on the other hand, occurs mainly below 800 mb inside 300 km where the inflow and acceleration toward lower pressure are large.

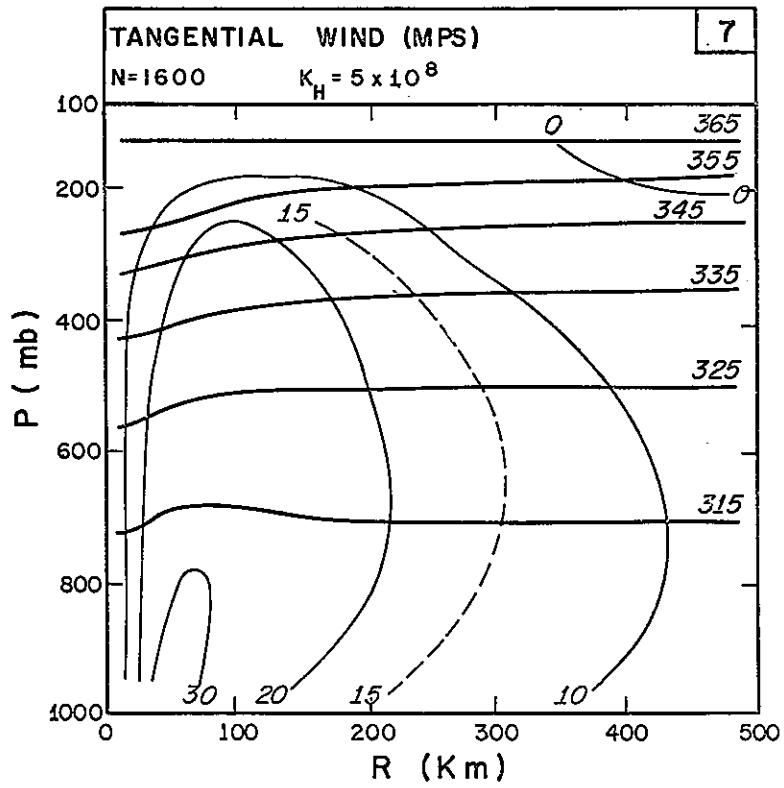


Figure 29. Tangential wind cross section for Experiment 7

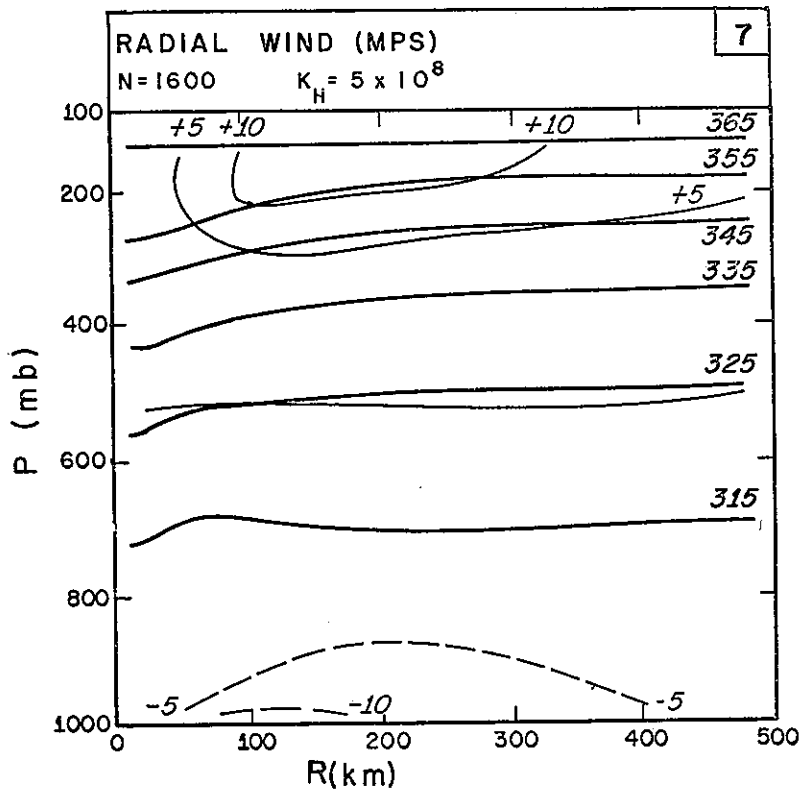


Figure 30. Radial wind cross section in Experiment 7

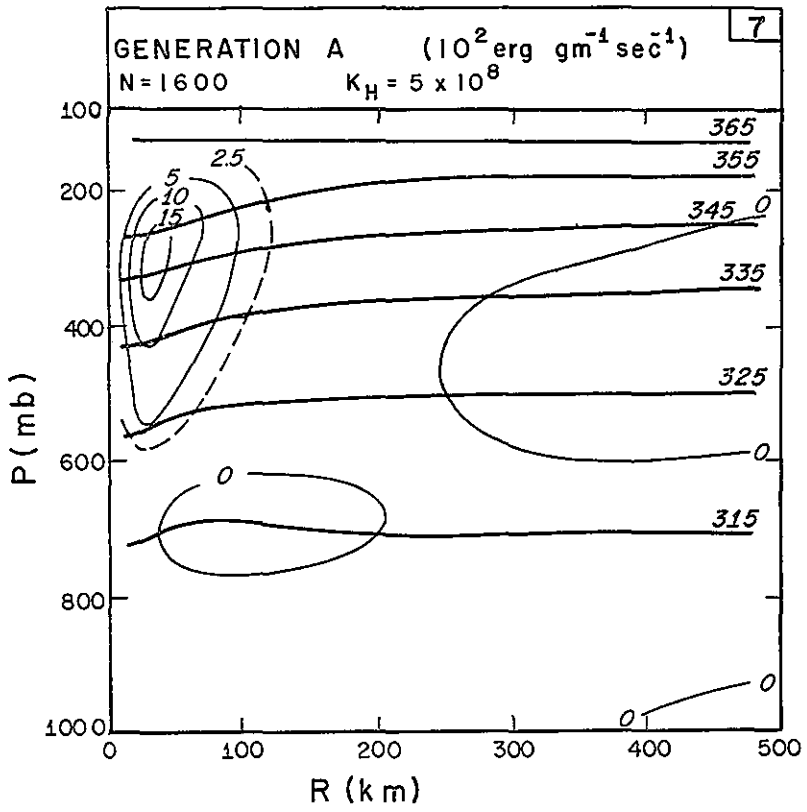


Figure 31. Generation of available potential energy in Experiment 7

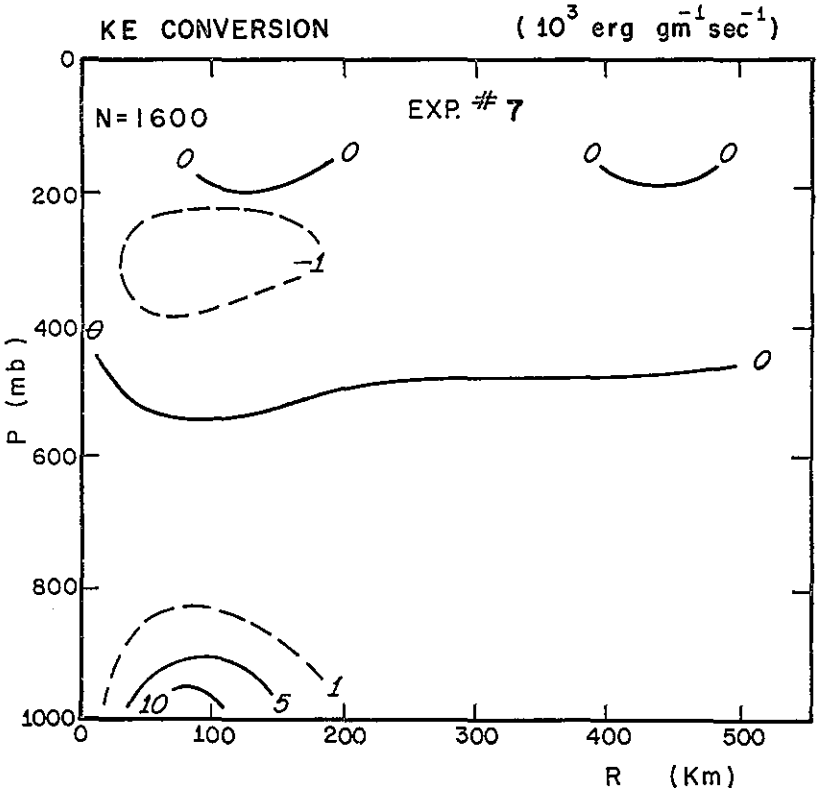


Figure 32. Kinetic energy conversion in Experiment 7

A small region of negative conversion occurs in the upper troposphere near the center as air flows outward against the pressure gradient force.

Energy Budget. The energy budget by radial rings for Experiment 7 is shown in figure 33. Compared to Experiment 6 (fig. 34) all components of the time rate of change of the energy budget are reduced, especially beyond 200 km where the heating is significantly less. In the total energy budget (see table 1), the generation of available potential energy and its conversion to kinetic energy are reduced to 10.7 and 16.5 x $10^{12}$ watts, respectively - values which compare favorably with the empirical results in table 3. The kinetic energy sinks are 9.2 x $10^{12}$ watts for surface drag, 11.0 x $10^{12}$ watts for vertical mixing, and 5.7 x $10^{12}$ watts for horizontal mixing. Comparison of these dissipation rates with empirical results is difficult. While the dissipation by drag friction is readily computed from hurricane wind data, dissipation by internal mixing is usually computed as a residual in a kinetic energy budget. Also, the empirical results in table 3 were determined for only a small portion of the storm ( $r \leq 150$ km).

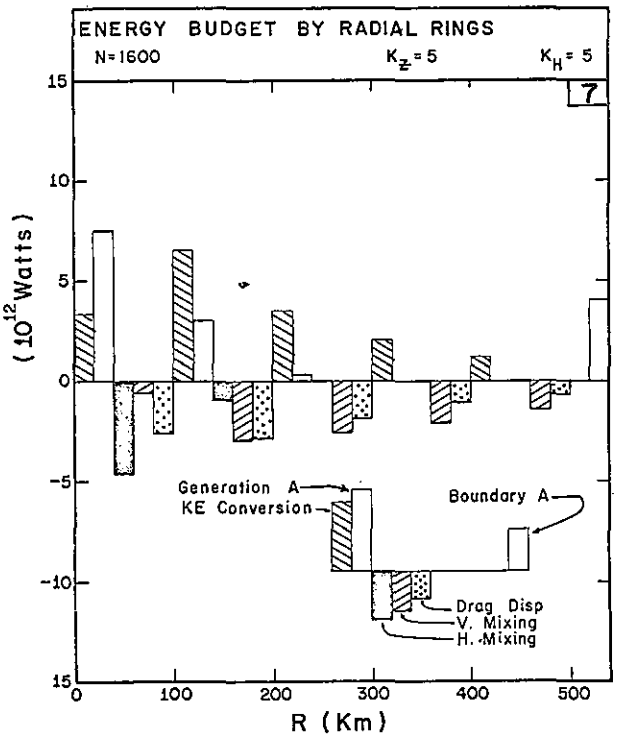


Figure 33. Energy budget for Experiment 7

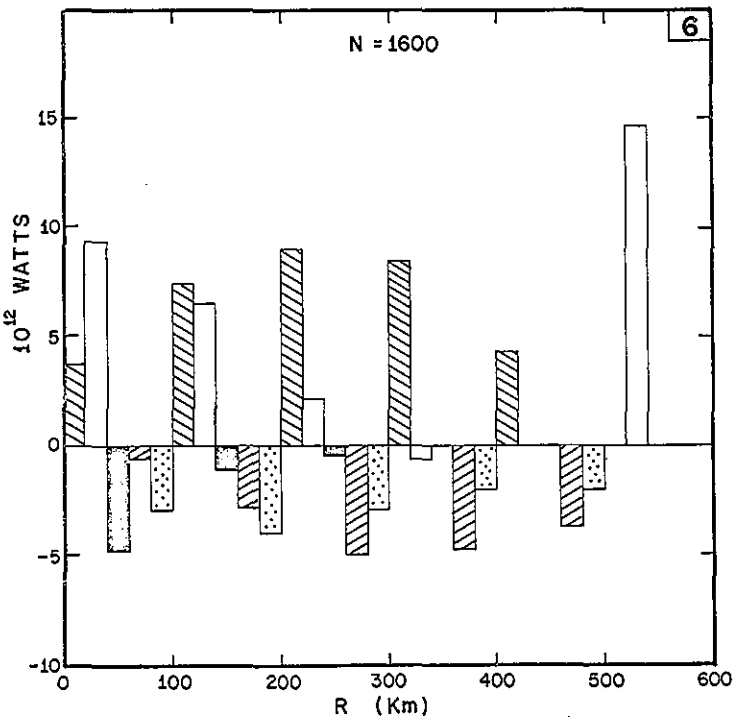


Figure 34. Energy budget in Experiment 3 ( see fig. 33 for key).

In view of the above uncertainties, the dissipation rates in Experiment 7 appear reasonable. Inside 200 km, the ratio of internal to surface friction is about 1.2, which approximately agrees with empirical results. Beyond 200 km this ratio increases because of the large dissipation from vertical mixing. The vertical mixing may be overestimated in this region for two reasons: First, the assumption that $K_z$ is constant horizontally is very crude. The vertical turbulance, including cumulus convection, probably decreases with increasing radius; therefore $K_z$ in the model should decrease also. Second, the large vertical mixing dissipation is related to the fact that the middle level winds in the outer region have not yet completely adjusted to the upper and lower level winds, a consequence of the weak vertical coupling mentioned earlier. Thus the vertical shear resulting from the initial conditions is still large. The fact that the ratio of vertical mixing to surface dissipation decreases with increasing iteration step provides support for this second reason.

In summary, the effect of reducing the heating beyond 200 km in Experiment 7 is to significantly reduce the tangential and radial wind components at larger radii. For a reduction of the total heating by 50 percent, only a 3 percent decrease in maximum wind is produced. The generation and conversion of available energy and dissipation of kinetic

energy compare favorably with empirical evidence, even though the total heating is somewhat higher than empirical results.

Very Concentrated Heating Near Center: Experiment 8. The thermal forcing by the extremely concentrated heating function, Type C in figure 3, is studied in Experiment 8. Inside 100 km the horizontal distribution is essentially unchanged from that in Experiments 6 and 7. The heating rate beyond 100 km is greatly reduced and the total heating decreases to $5.5 \times 10^{12}$ watts, an amount comparable to observational evidence (table 3).

Because of the concentrated heating distribution, a variable grid was utilized in Experiment 8. For $r \leq 160$ km the resolution is 10 km. For $r > 160$ km the resolution varies smoothly from 10 km at 160 km to 25 km at the maximum radius of 500 km. The use of a variable grid is justified in a later experiment.

Momentum and Temperature Structures. Within 100 km the tangential and radial wind profiles for Experiment 8, shown in figure 35, are quite similar to the profiles for Experiment 7 (fig. 28). The slight shift inward of the maximum wind from 60 km (Experiment 7) to 50 km (Experiment 8) is probably a consequence of the increased resolution rather than the heating reduction beyond 100 km.

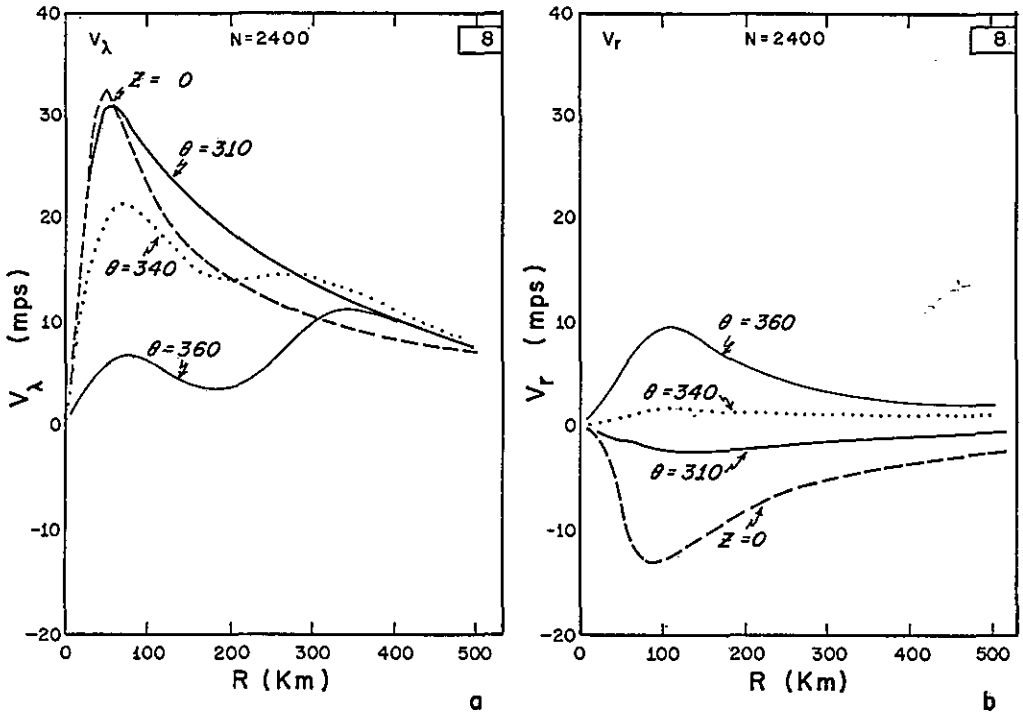


Figure 35. Tangential and radial wind profiles in Experiment 8

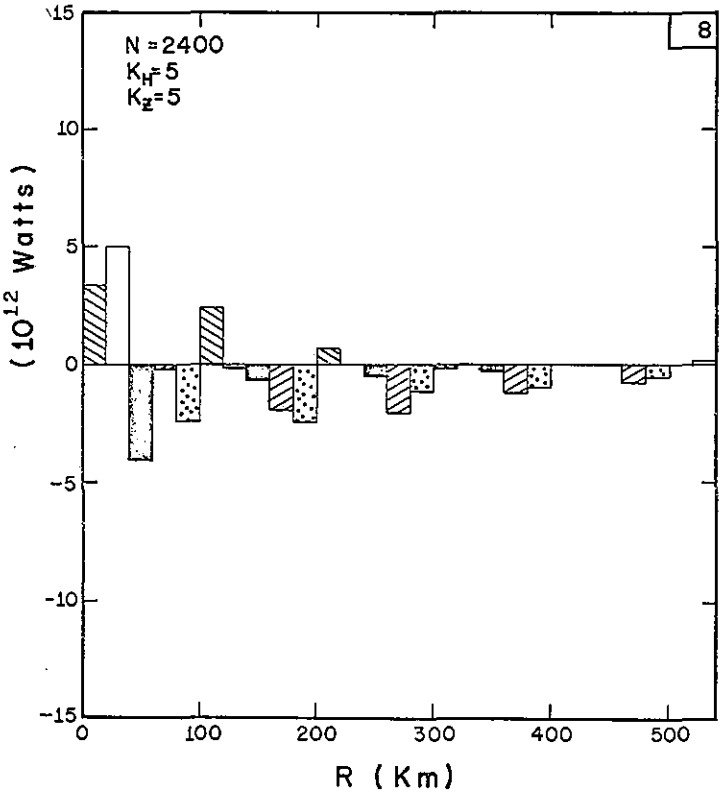


Figure 36. Energy budget for Experiment 8 (see fig. 33 for key).

Although changes inside 100 km are small, large differences are present at greater distances. Maximum outflow is reduced from 14 m/sec at 180 km (Experiment 7) to 10 m/sec at 100 km (Experiment 8). At 300 km the outflow is reduced from 11 m/sec to 3 m/sec.

The decreased outflow produces a different tangential wind distribution at larger radii. Whereas the stronger outflow in Experiment 6 and 7 produces anticyclonic winds at 500 km by an outward advection of low angular momentum from the center, there is little radial advection at this distance in Experiment 8. Thus internal mixing dominates and the tangential winds slowly decay.

Energy Budget. The energy budget, shown in figure 36, reflects the decrease in storm intensity compared with Experiments 6 and 7. The generation of available energy occurs entirely within 100 km. The boundary term in the available energy budget decreases from $4.2 \times 10^{12}$ watts to $0.1 \times 10^{12}$ watts. The total energy budget (table 2) shows significantly smaller values for all processes, except horizontal mixing. The dissipation by horizontal mixing is nearly constant because the curvature of the wind profile inside 100 km is relatively unchanged.

Experiments 6, 7, and 8 indicate that the reduction of heating at large distances has little effect on the inner

region of the storm and suggests that the maximum winds are determined primarily by heating in the inner region. As the heating is reduced at larger distances, the storm decreases in horizontal extent and the tangential and radial winds beyond 100 km are reduced. The size and intensity of the anticyclone aloft is closely related to the amount of heating at large distances from the center. This relationship suggests that the intensity of the thermal anticyclone associated with storms in nature should be closely correlated with the diameter of the active convective area.

Primary Heating Near Center With Secondary Maximum at 200 km: Experiment 9 - In the final experiment studying the horizontal variation of heating, a secondary heating maximum is introduced at 200 km. See rainfall type D in figure 3. The heating rate in the inner region is reduced slightly from that in Experiment 7 so that the total heat release remains fixed. The introduction of a secondary heating maximum is an attempt to investigate the possible role of hurricane rainbands in which substantial precipitation occurs at some distance from the center (Gentry, 1964). Although rainbands are generally asymmetric and spiral in toward the center, the mean effect in an axisymmetric model appears as a ring of enhanced convection.

The results from Experiment 9 show rather small changes from those in Experiment 7. The profiles of the tangential and radial winds at the surface and 340°K for Experiments 7 and 9 are compared in figure 37. The weak secondary heating maximum reduces the maximum tangential wind from 33 to 31 m/sec at 60 km and produces a slight increase in middle levels at 200 km. The latter increase is caused by the increased vertical transport of low-level momentum.

The radial wind profile shows a slightly weaker circulation inside 200 km. Maximum inflow is reduced from 14 to 13 m/sec at 80 km, and the single outflow maximum at 180 km in Experiment 7 is replaced by two weaker maxima at 100 and 200 km in Experiment 9.

Experiment 9 may have some relevance to hurricane modification experiments (Project STORMFURY , 1969). One aspect of STORMFURY involves seeding supercooled water in rainbands with silver iodide crystals. The additional heat of fusion would then increase the heating at this distance and possibly reduce the amount of air reaching the center by deviating the inflow upward. This chain of events would then result in a decrease of the maximum winds near the center.

The changes in circulation in Experiment 9 that result from an increase in heating at 200 km and a slight decrease inside 200 km are small, but confirm the hypothesis of the

rainband experiments in Project STORMFURY. However, the results are inconclusive. From one point of view it may be argued that the reduction in maximum winds is small in comparison to the changes in the heating distribution. On the other hand, if the hurricane vortex is unstable, a small change might produce interactions which cause greater differences with time. The steady-state model, of course, is not capable of studying such feed-back.

4.3.2 Vertical Variation of Latent Heating: Experiment 10

The vertical distribution of latent heating is an important aspect of the tropical cyclone problem. In extratropical regions, which are normally conditionally stable, most of the large scale condensation heating results from stable moist adiabatic ascent. In the conditionally unstable tropics; however, large scale lifting results in small scale convection. The vertical distribution of the environmental heating by the convection is a complicated process and involves entrainment, horizontal and vertical mixing, and large scale vertical motion. The effective heating of the large scale may then be quite different from the cloud scale distribution.

Early attempts at hurricane modeling (e.g., Kasahara, 1961; Rosenthal, 1964) related the heating to the variation of saturation specific humidity, $q_s$ , along an appropriate

moist adiabat. This pseudo-adiabatic type of heating resulted in unrealistic circulations, and showed that the hurricane could not be considered a huge cloud. Kuo (1965) attempted to relate the large scale to the cloud scale heating by making the heat release at any level proportional to the cloud-environment temperature difference. Parameterization similar to this type of heating (hereafter called "cloud-environment" type) has given quite realistic results in prognostic hurricane models (Yamasaki, 1968a,b; Rosenthal, 1969).

The relative variation of the heating profiles between the pseudo-adiabatic and cloud-environment types are contrasted in figure 38. The variation of $\frac{\partial q_s}{\partial T}$ along several moist adiabats is shown for a surface pressure of 1010 mb, a relative humidity of 85 percent, and various surface temperatures. The dashed profile is the difference between the temperature of the moist adiabat defined by an equivalent potential temperature of 362.6°K and the mean hurricane season environmental temperature (Jordan, 1958).

A much higher proportion of heat is released in the upper levels in the cloud-environment type than in the pseudo-adiabatic type. The ratio of 300 to 600 mb heating in the former is about 1.7 while in the latter the ratio varies from 1.0 to 0.5. From a linear analysis, Rosenthal

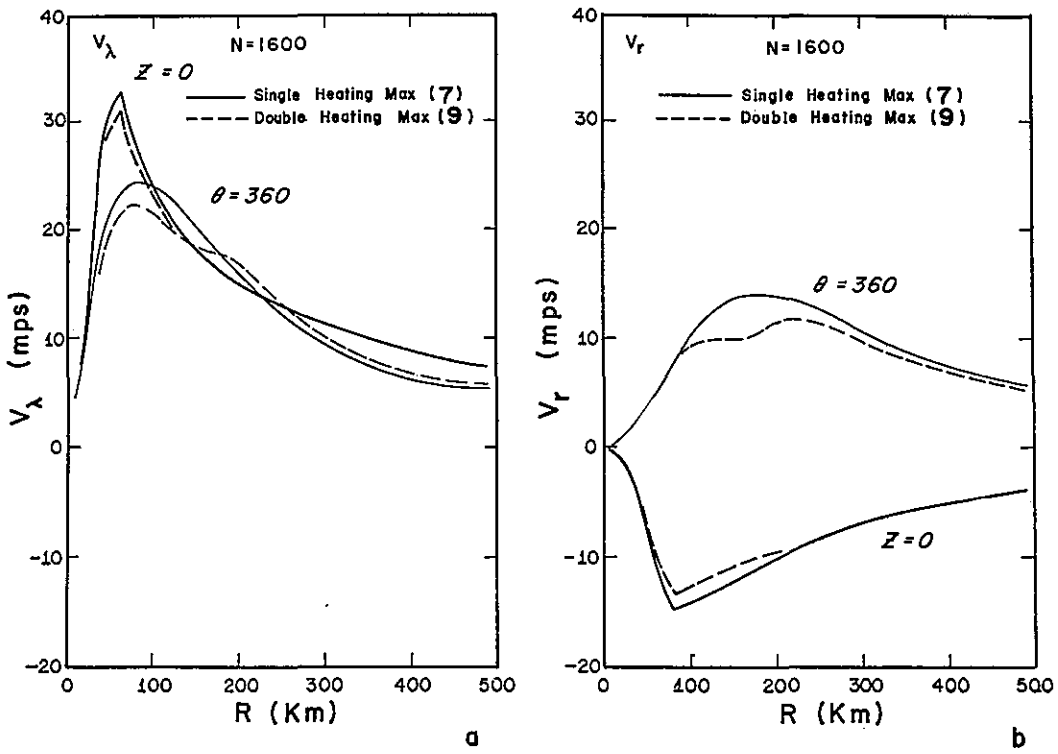


Figure 37. Tangential and radial wind profiles in Experiment 7 and 9

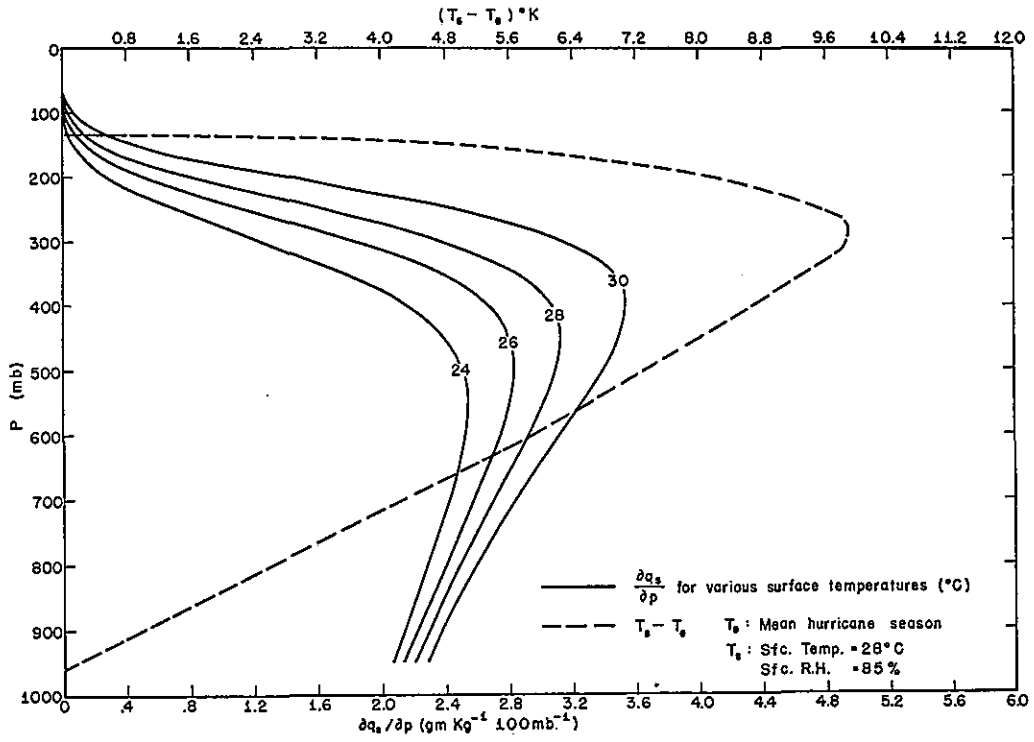


Figure 38. Vertical profiles for pseudo-adiabat and cloud-environment type latent heating for various conditions

and Koss (1968) showed that this ratio was an important parameter in the growth of tropical cyclones. They found reasonable growth rates and thermal structures for a ratio of 1.25. Yamasaki (1968a) found reasonable results for a ratio of about 1.1. These values are easily exceeded in the could-environment type heating. In the pseudo-adiabatic type, however, the ratio is highly dependent on $\theta_e$ , approaching the critical value only for very warm, moist air.

In Experiment 10 the vertical distribution of heating is proportional to $\frac{\partial \theta_e}{\partial p}$ along the moist adiabat defined by a surface temperature of 28°C shown in figure 38. The same distribution is also contrasted with the vertical heating distribution of the earlier experiments in figure 4. The horizontal heating distribution and all other parameters were identical to those in Experiment 7. The vertical cross section of heating is shown in figure 39.

Figure 40 shows the radial profiles of tangential and radial winds in Experiment 10. The low-level tangential wind profiles are similar to those in Experiment 7 (fig. 28). The reduced vertical transport of momentum in the upper levels, however, yields weaker winds. The radial wind profiles show a deep, weak outflow layer in Experiment 10 in contrast to the shallow, strong outflow layer of Experiment 7. This difference is related to the change in thermal structure

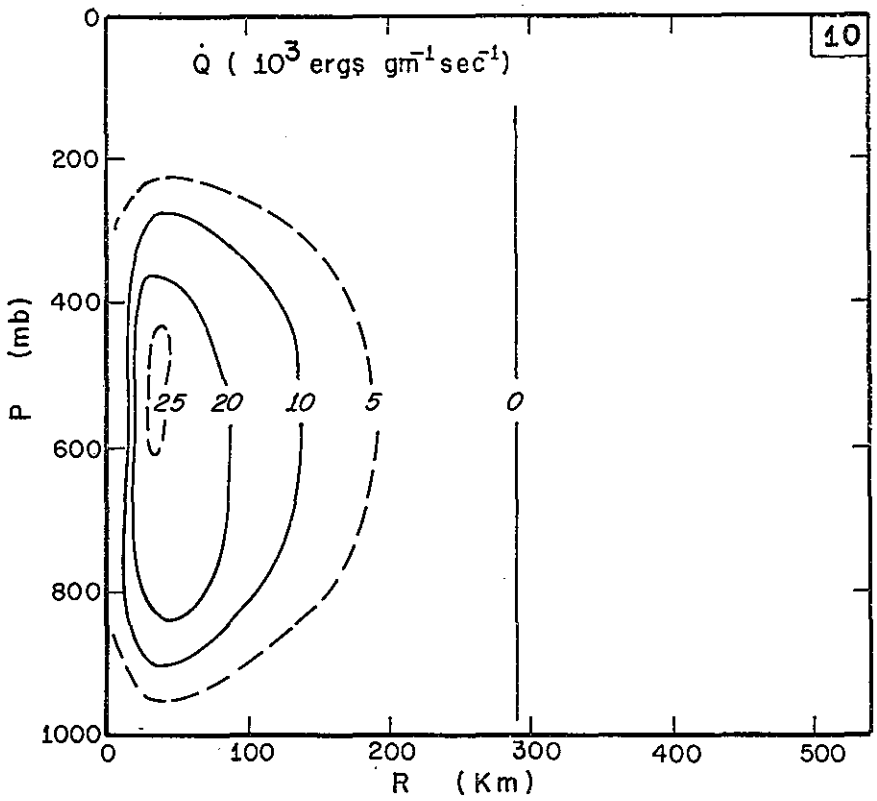


Figure 39. Cross section of latent heat release in Experiment 10

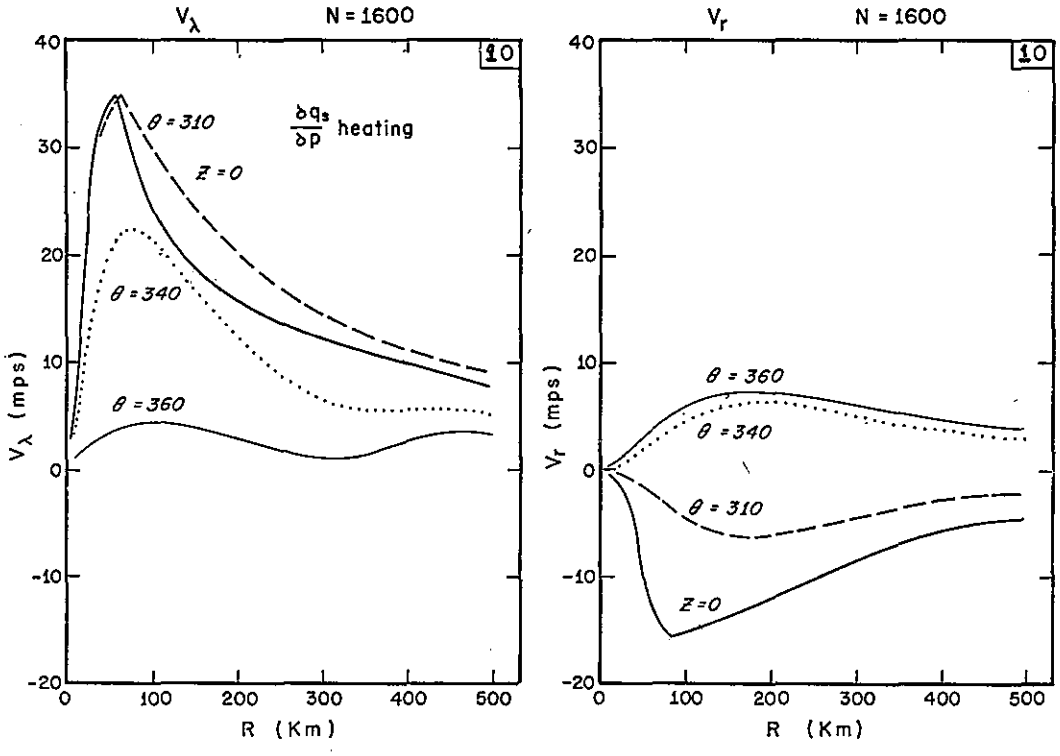


Figure 40. Tangential and radial wind profiles in Experiment 10

shown in figure 41. In Experiment 10 the level of maximum temperature departure drops from 300 mb to 500 mb, the pressure gradient decreases more rapidly with height, and the outflow begins at lower levels. Near 200 mb the atmosphere is nearly undisturbed, and the radial and tangential circulations at this level are less than those in Experiment 7.

Both the temperature structure and the radial winds in the upper levels are unrealistic in the pseudo-adiabatic type of heating of Experiment 10. Observations show that the maximum temperature departure occurs in the upper rather than middle troposphere (Hawkins and Rubsam, 1968; Malkus and Riehl, 1961). They also support a thin, strong outflow layer rather than a deep, sluggish layer (Miller, 1958, 1964). These results confirm that the cloud-scale heating is not appropriate to the hurricane scale in the mature, slowly varying state.

### 4.3.3 Variation of Total Heating: Experiment 11

The results from the previous experiments emphasize the importance of variable heating distributions. In all the experiments the heating maximum was defined by a rainfall rate of about 50 cm/day at 30 km, a moderate rate for a mature hurricane. In Experiment 11 the heating function is

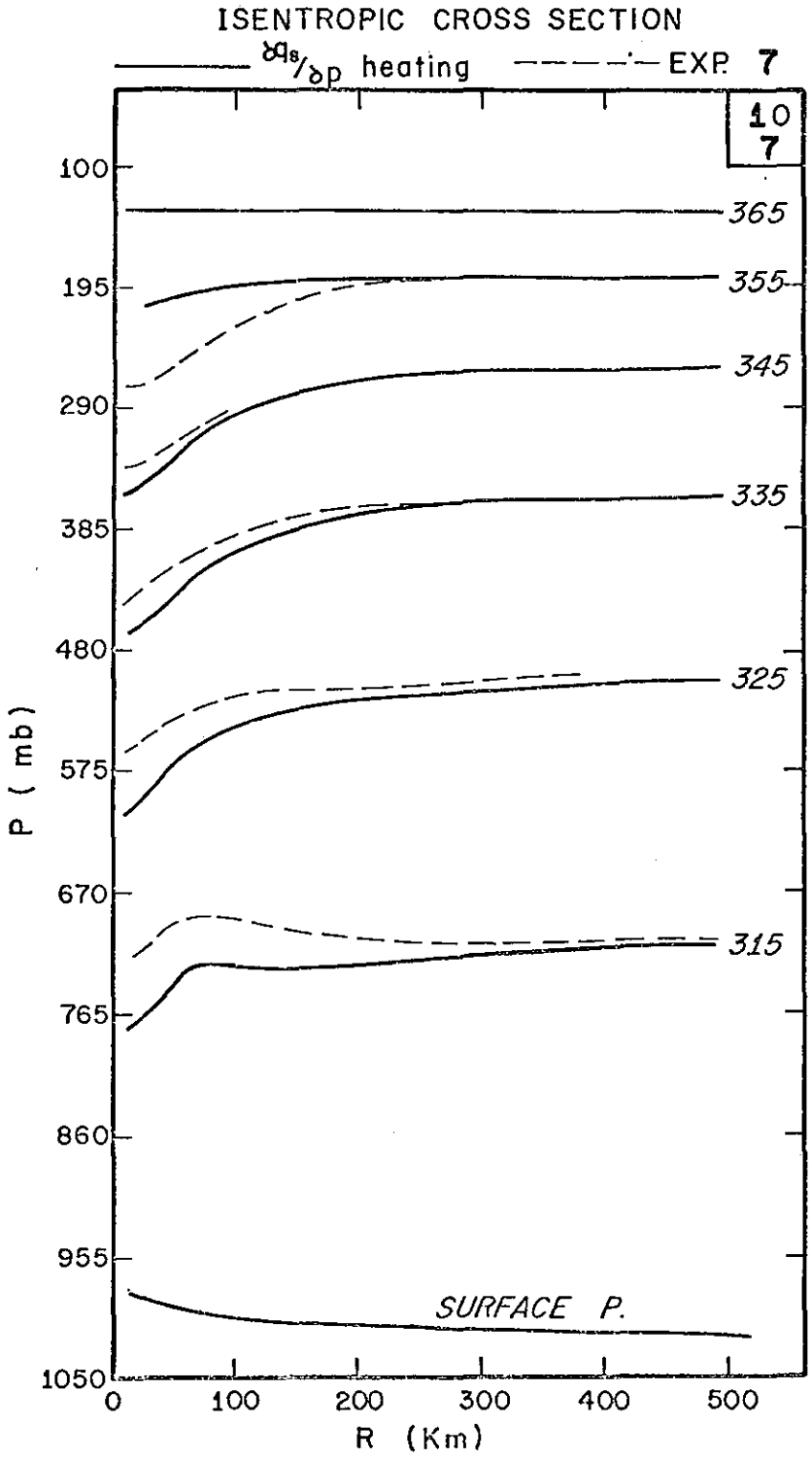


Figure 41. Isentropic cross section Experiments 7 and 10

one half that of Experiment 7, while the horizontal and vertical heating variation and all other parameters are identical.

Figures 42 and 43 show the momentum and temperature profiles of the slowly varying state. As expected, the tangential and radial circulations are considerably less than those in Experiment 7, and the thermal structure shows a weaker warm core. The maximum tangential wind is reduced from 33 to 25 m/sec; maximum inflow is reduced from 15 to 9 m/sec, while the outflow is decreased from 14 to 7 m/sec. The maximum temperature departure is reduced from +10°C to + 4°C.

The energy budget for Experiment 11, summarized in table 2, shows a reduction by a factor of two or three. The kinetic energy is still decreasing after 1600 iterations, indicating that true steady-state circulations, especially at large distances from the center, will be weaker than those presented in figure 42. Thus the thermal forcing given by the rainfall rates of Experiment 11 produces a circulation that is typical of a moderate to weak tropical storm.

### 4.3.4 The Role of Infrared Cooling: Experiment 13

Becuase of the immense importance of latent and sensible heat as energy sources into the tropical cyclone system, little attention has been directed toward infrared cooling as a sink of energy. In numerical experiments to date,

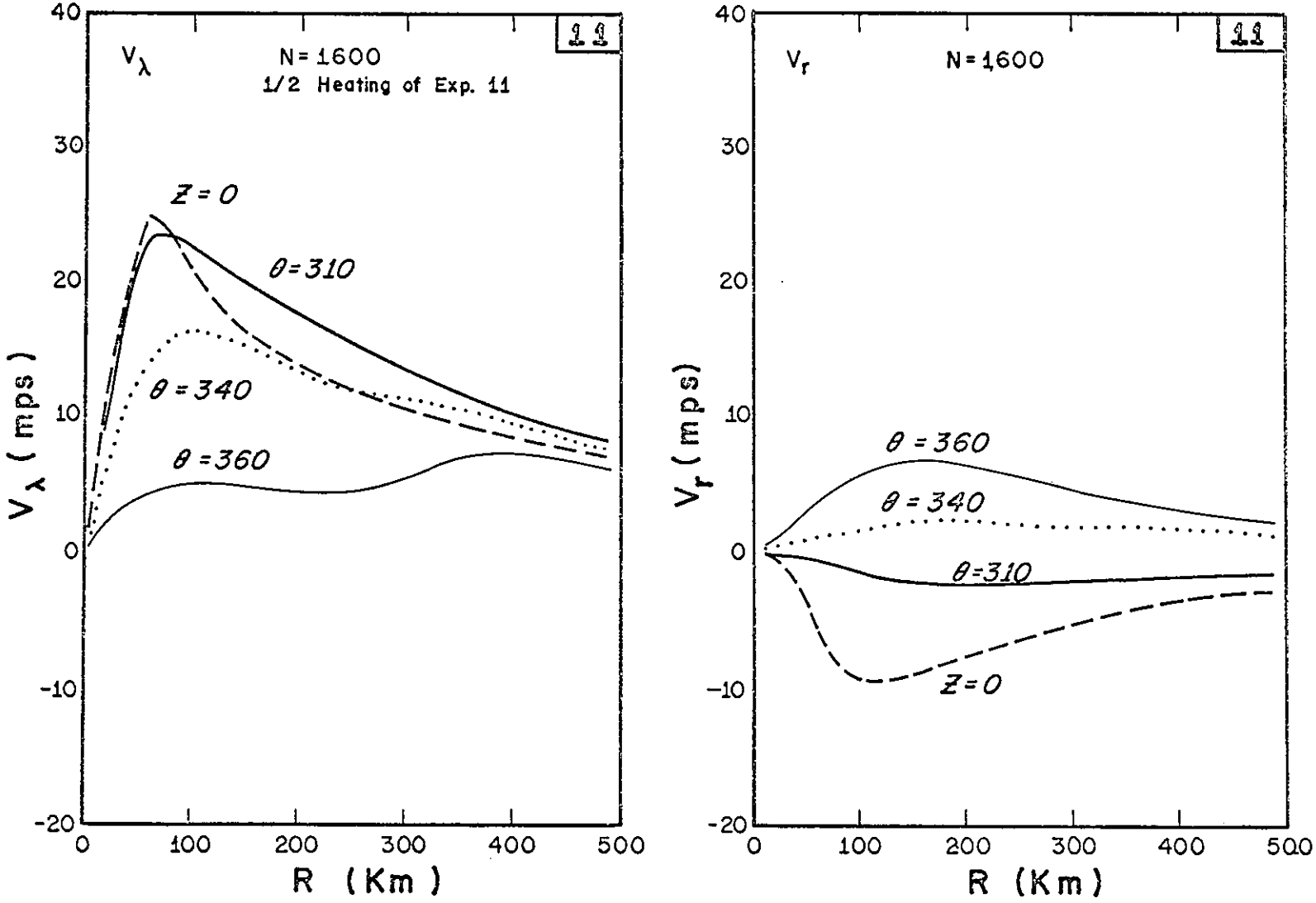


Figure 42. Tangential and radial wind profiles in Experiment 11

only Ooyama (1969) included the effect of radiative cooling. Ooyama experimented with a uniform cooling rate and found little change from the non-cooling cases. He notes, however, that differential cooling may affect the development of tropical cyclones.

In the Hurricane Hilda study, Anthes and Johnson (1968) estimated that infrared cooling in the outer region of the storm could generate 15 to 20 percent of the total generation of available potential energy on the hurricane scale (1000 km). The total cooling nearly equalled the total latent heating on this scale. It is important, therefore, to ascertain whether radiative cooling represents a passive energy loss or contributes actively toward maintaining the baroclinicity in the hurricane.

If the 15 to 20 percent generation by infrared emission is respresentative, the effect of the cooling on the dynamics should be investigated, in view of the strong correlation between generation of available energy and conversion to kinetic energy in these experiments. Appendix C presents radiative cooling rates in the clear tropical atmosphere, which are computed using Sasamori's (1968) radiation model. Sasamori's model is quite suitable for use in numerical models of the tropical cyclone because of its relative simplicity and computational economy in terms of speed and storage.

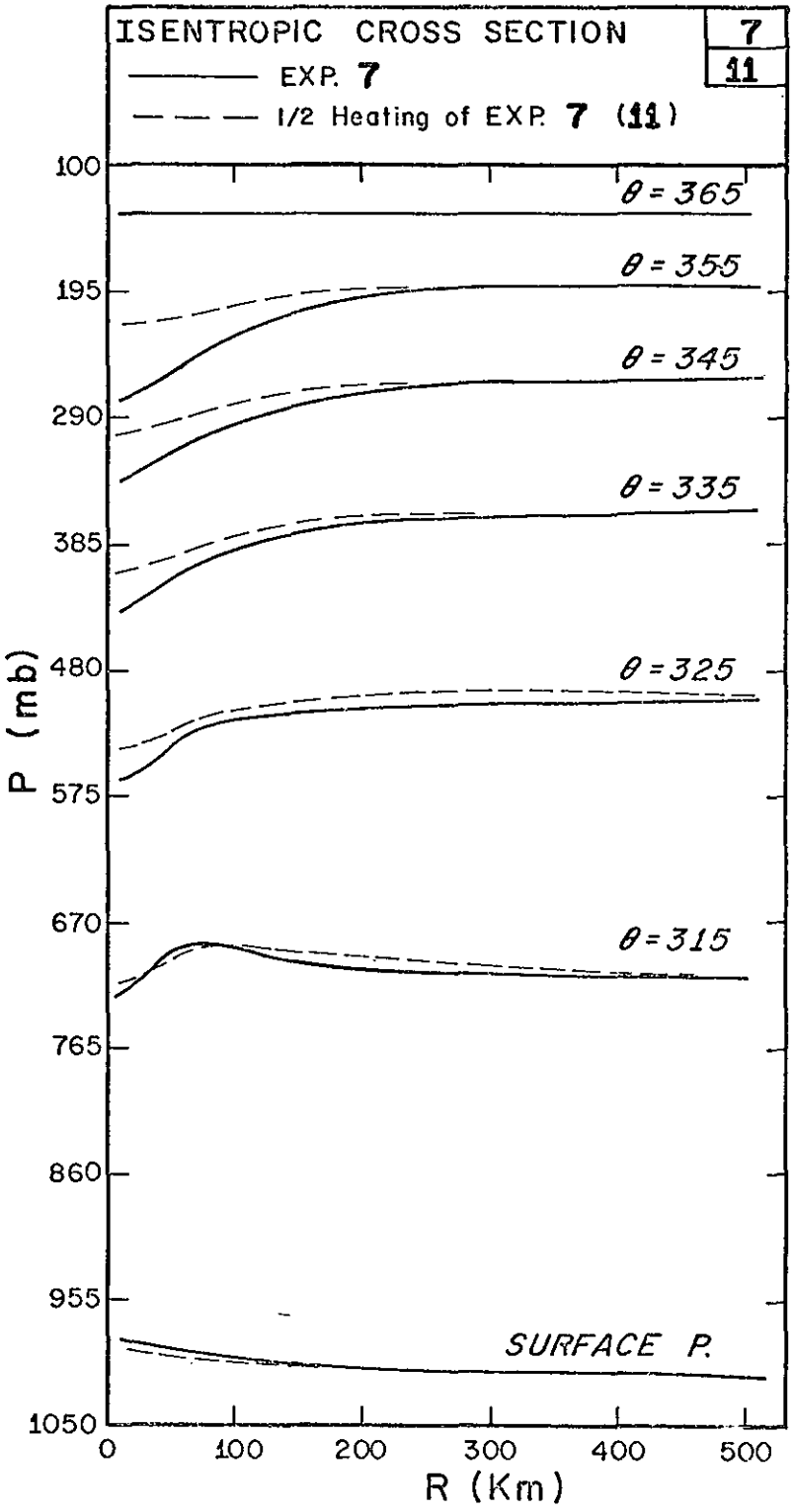


Figure 43. Isentropic cross section in Experiments 7 and 11

Experiments 12 and 13 contrast the effects of radiative cooling on the slowly varying state of the tropical cyclone. The horizontal domain is extended to 1000 km for these experiments. Experiment 12 represents the non-cooling control experiment and is identical to Experiment 7 except for the larger domain. The effects of this change are minor and are discussed separately in a later section.

Experiment 13 is identical to Experiment 12 except that uniform horizontal cooling occurs from 300 km (assumed to be the edge of the cloud cover) to 1000 km. The vertical distribution is given by the mean cooling profile shown in appendix C, figure C4.

Momentum and Temperature Structures. Figures 44, 45, and 46 show the tangential and radial wind profiles and the thermal structure for the cooling and non-cooling experiments. The cooling results in an increase of 1.5 m/sec in maximum tangential wind and an increase of 1 m/sec in maximum inflow. As expected, the temperatures beyond 300 km are cooler in Experiment 13. A somewhat surprising result, however, is the cooling in the core of the storm, which is nearly as great as that in the outer regions. This cooling is apparently due to horizontal advection and mixing.

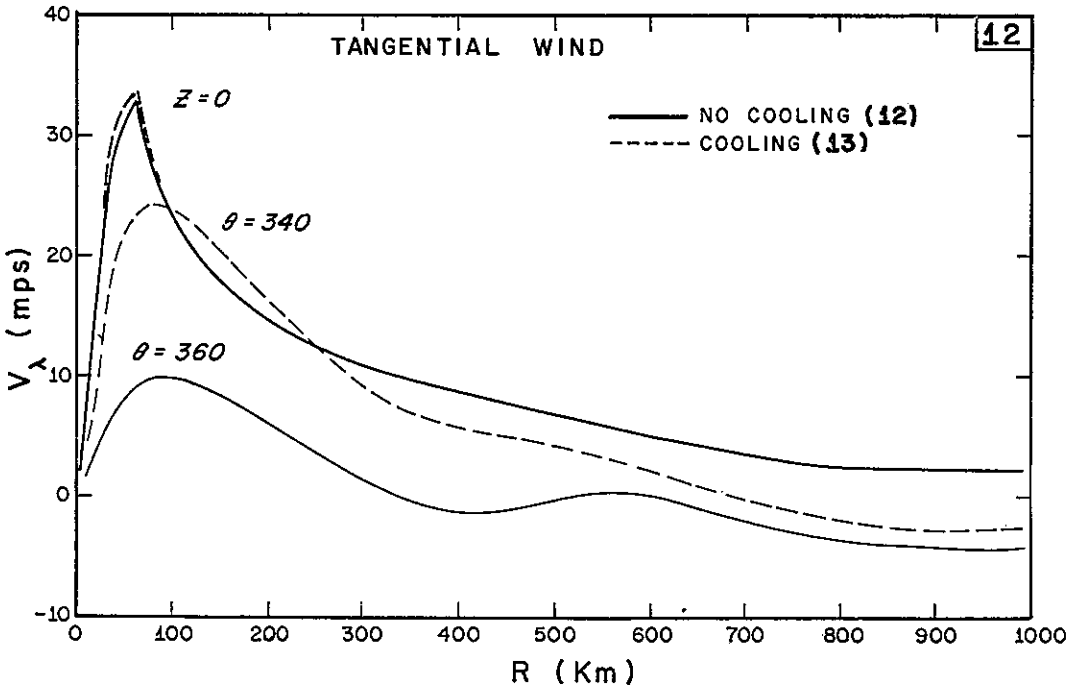


Figure 44. Tangential wind profiles in Experiments 12 and 13

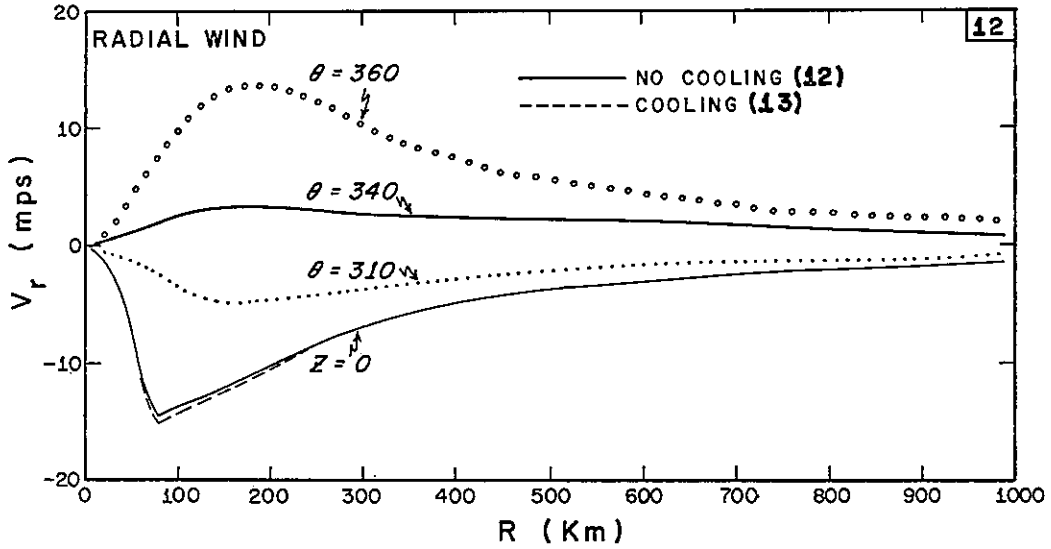


Figure 45. Radial wind profiles in Experiments 12 and 13

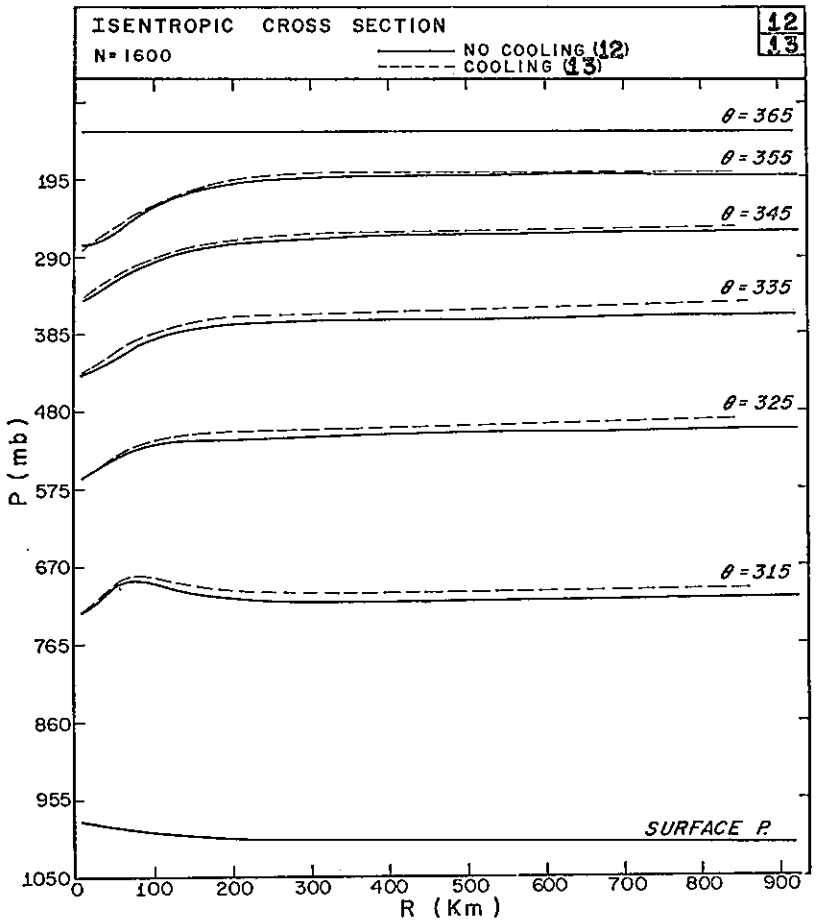


Figure 46. Isentropic cross section for Experiments 12 and 13

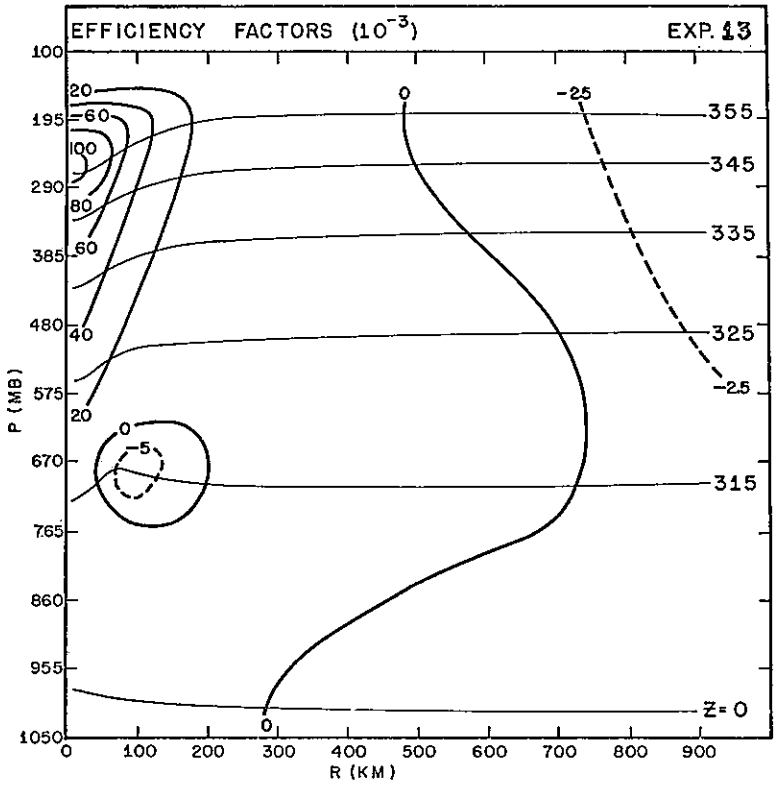


Figure 47. Isentropic and efficiency factor cross section in Experiment 13

Energy Budget. The difference in temperature structures (fig. 46) indicates that the radiative sink of energy is considerable. The total cooling of $3.4 \times 10^{14}$ watts is about a third of the total heating of $11.0 \times 10^{14}$ watts, and confirms that the radiative heat loss is the same order of magnitude as the latent heat gain on the scale of 1000 km.

The generation of available potential energy by the cooling is $0.2 \times 10^{12}$ watts, or about 1.5 percent of the total generation. This is considerably less than the 17 percent estimated by Anthes and Johnson (1968). The difference is related to differences in temperature structures between Hurricane Hilda and Experiment 13. Figures 47 and 48 show the efficiency factor cross sections for Hilda and for Experiment 13. The greater large scale baroclinicity beyond 500 km in the Hilda environment results in a large magnitude for the negative efficiency factors. Thus cooling at 1000 km in the Hilda enviornment generates more available potential energy than in Experiment 13. Another factor is the infrared emmision in the region of positive efficiency factors. In Hilda, cooling was computed from 500 to 1000 km, a region of mostly negative efficiency factors. In Experiment 13, cooling occurs from 300 to 1000 km. Because the 300-500 km region consists of positive efficiency factors, the infrared generation of available energy is negative in this region.

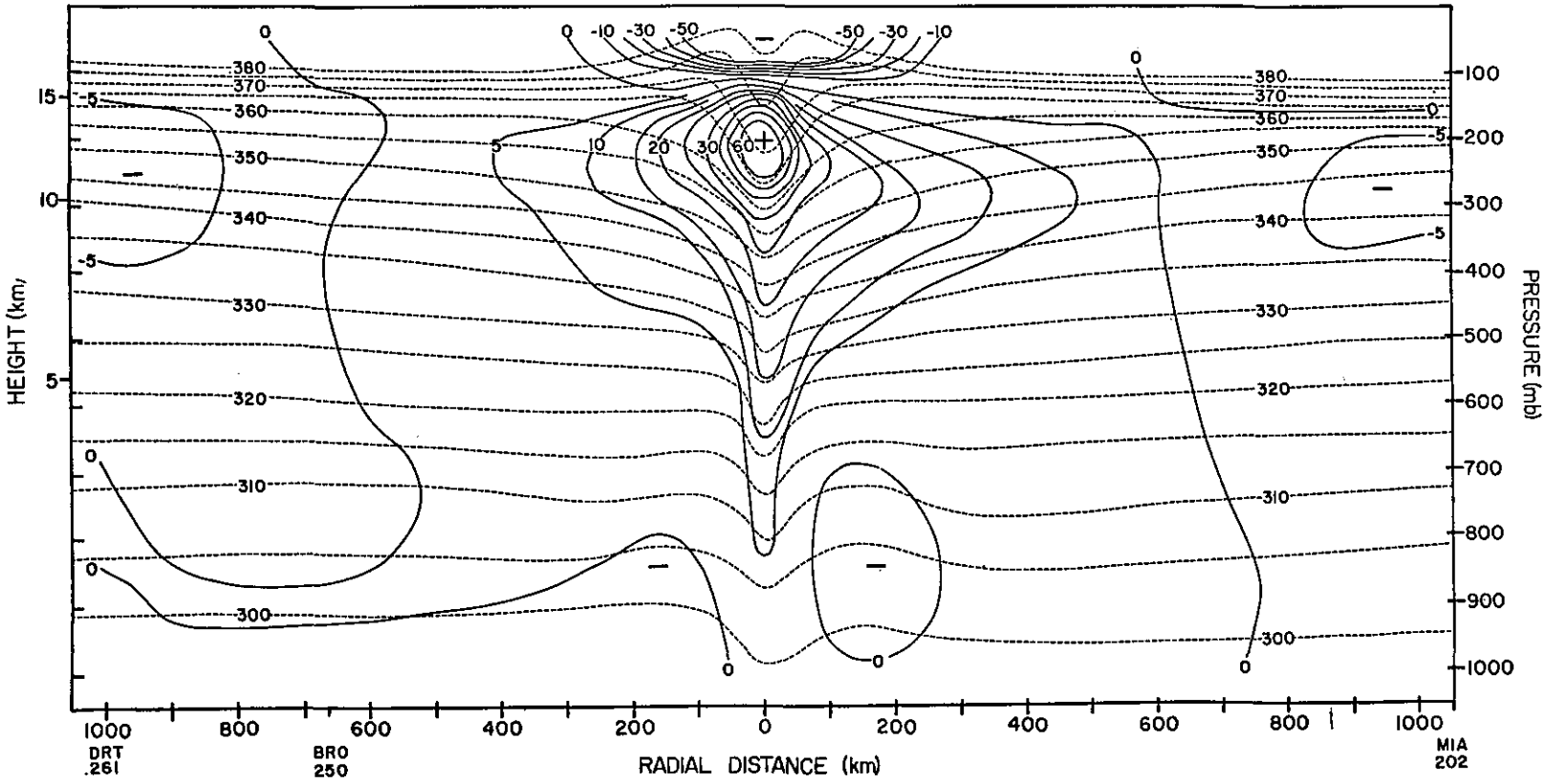


Figure 48. Isentropic and efficiency factor cross section in Hurricane Hilda (1964). From Anthes and Johnson (1968)

The energy budget by 100 km rings for Experiments 12 and 13 is shown in figure 49 and the total budget is summarized in table 2. Although the percentage of generation by radiation is less than 2 percent, the total generation is about 6 percent higher in Experiment 13. Thus the slightly increased baroclinicity in the cooling experiment results in an increase in the generation by the latent heating.

Although the increase in maximum wind speed in the infrared experiment is only 1.5 m/sec, the total cooling represents a significant energy sink. The infrared generation of available energy is considerably less than an earlier diagnostic estimate. Even though the cooling has a small effect on the dynamics of a mature storm in near steady-state, the possibility remains that it may play a more significant role in the earlier stages of tropical storm development. Because the formative stages frequently span several days, the cumulative effect of differential cooling between clear and cloudy regions may be large. The gradual increase in baroclinicity could enhance the convective heating by accelerating the slow meridional circulation.

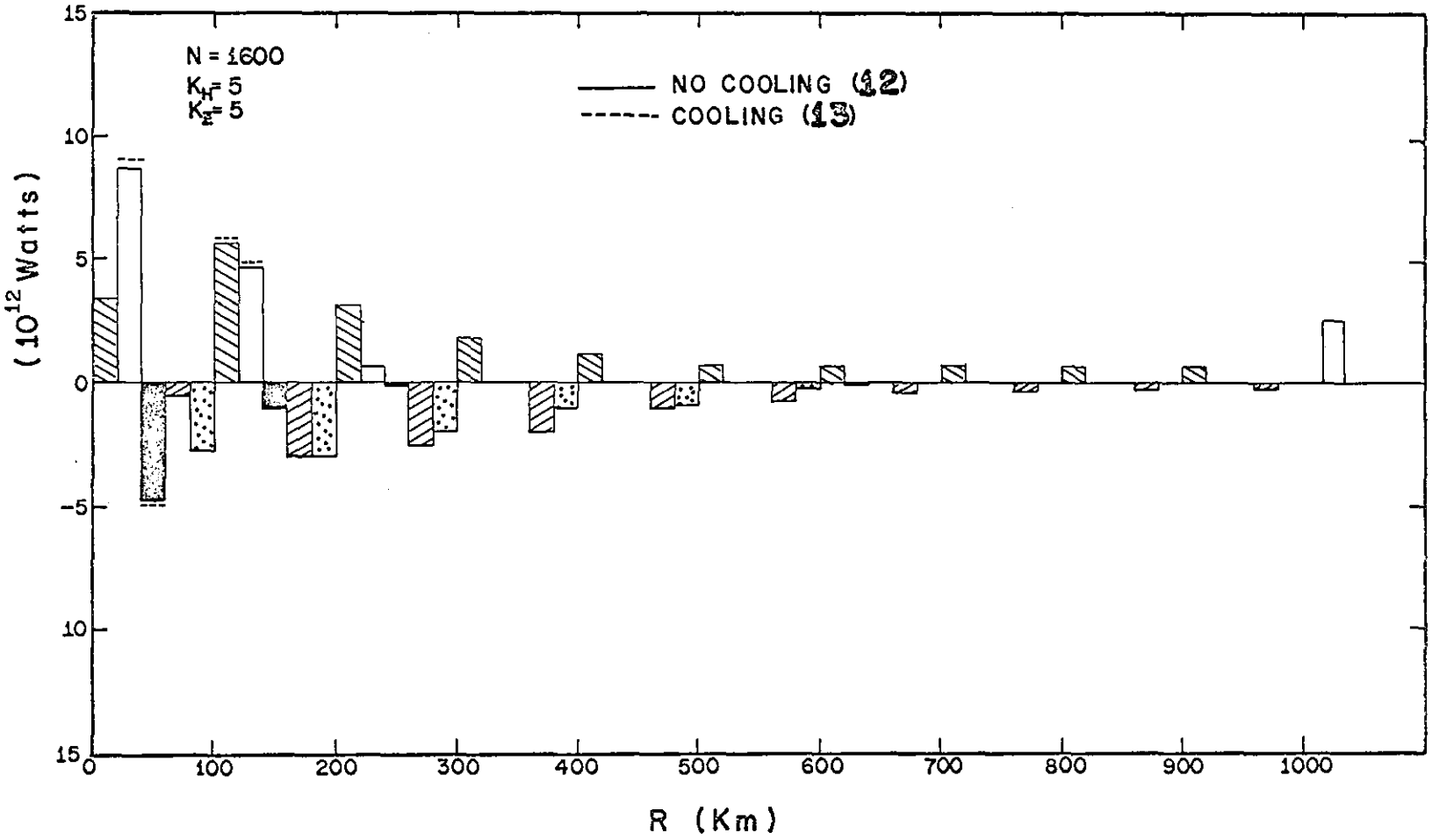


Figure 49. Energy budget for Experiments 12 and 13

## 4.4 Experiments of a Computational Nature

The experiments so far have emphasized primarily the role of physical processes such as variable mixing and heating in the determination of steady circulations. In numerical models, however, it is also important to ascertain the effect of the computational or artificial aspects of the model on the solutions. Ideally, the computational or artificial aspects of domain size, boundary conditions, and resolution should be small in comparison to physical effects. The experiments in this section compare solutions with domains of 500 and 1000 km, with constant horizontal resolutions of 10 and 20 km, and with a variable horizontal grid.

### 4.4.1 Domain Size: Experiment 12

The effect of the arbitrary horizontal boundary conditions may be investigated by increasing the size of the horizontal domain. Experiments 7 and 12 are identical, except that the horizontal domain of 500 km is extended to 1000 km in the latter. Figure 50 shows the tangential wind profiles for both experiments. Differences for r less than 200 km are less than 30 cm/sec at all levels. Between 300 and 500 km, however, the maximum difference is 1 m/sec. The low level tangential winds show greater anticyclonic shear in Experiment 12, a result of the boundary condition of

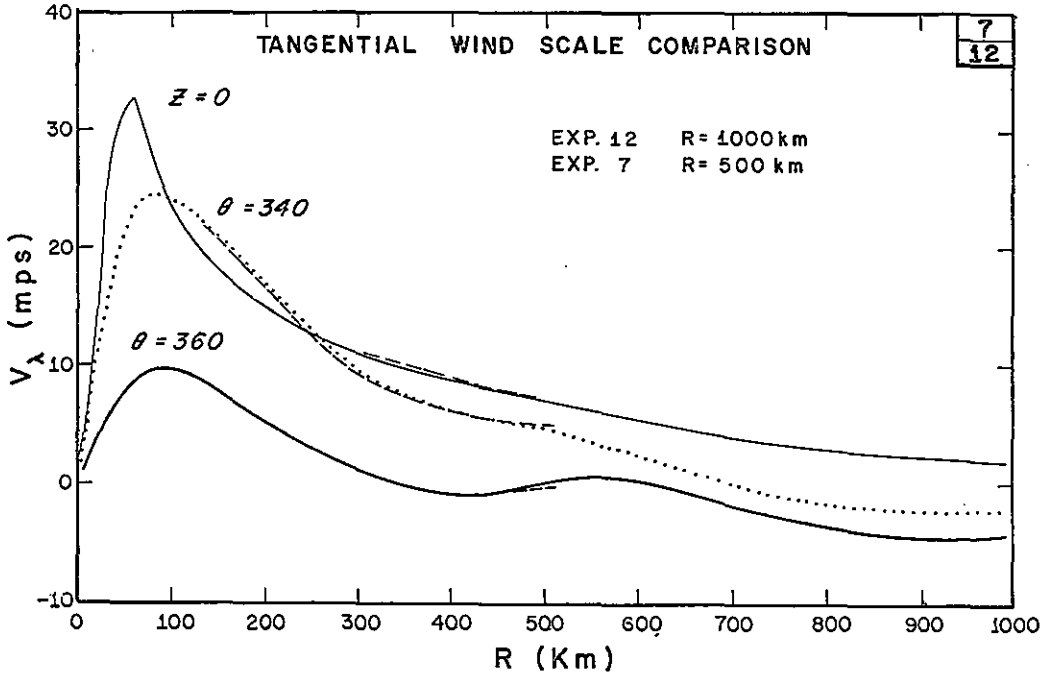


Figure 50. Tangential wind profiles in Experiments 7 and 12

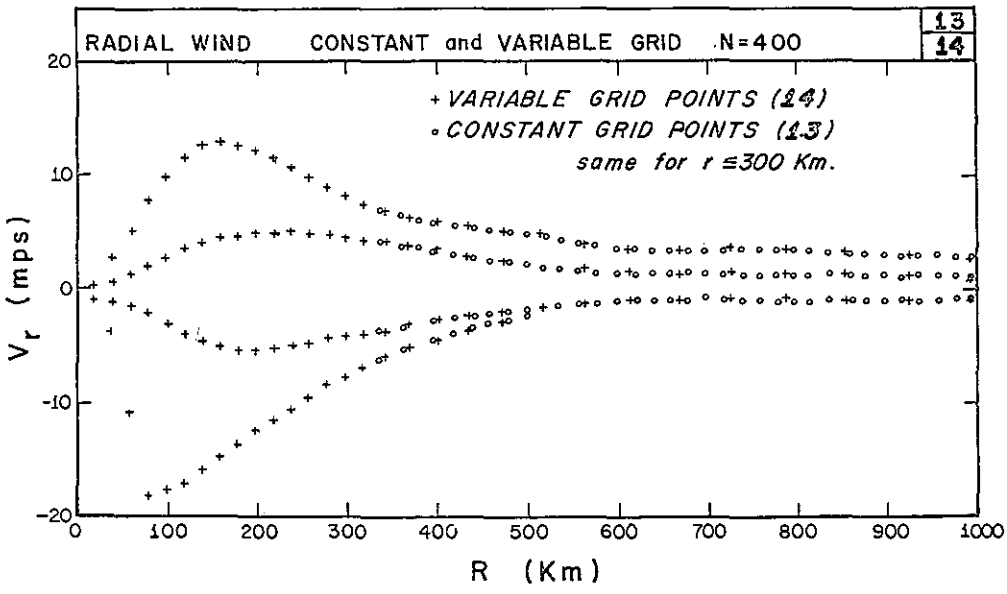


Figure 51. Radial wind profiles in Experiments 13 and 14

zero relative vorticity being shifted from 500 km in Experiment 7 to 1000 km in Experiment 12.

A small difference is also present in the low level radial wind profile (not shown). The boundary condition of zero divergence at 500 km in Experiment 7 is replaced by weak positive divergence in Experiment 12, and the inflow is less by 0.4 m/sec at this distance. The small differences between these two experiments, especially near the radius of maximum winds, justify using the 500 km domain for the non-cooling experiments.

### 4.4.2 Variable Grid: Experiment 14

In numerical models of atmospheric convective phenomena such as cumulus clouds, squall lines, or hurricanes, a greater resolution for a portion of the domain is desirable. For the hurricane a finer mesh is needed near the eyewall where horizontal gradients are large than in the environment of the storm where gradients are weak.

Recently Anthes (1969) utilized the transformation $r = x^2 + cx$ in Ogura's (1963) axisymmetric cumulus cloud model to obtain a continuously varying grid with highest resolution near the center. Although these results appeared reasonably good, later results (Reeves, 1969 and Anthes, 1969, unpublished manuscripts) showed that differences in

grid sizes near the origin could lead to large errors in estimating terms such as $\frac{1}{r}\frac{\partial v_r}{\partial r}$. Hence the transformation for this model is modified by retaining a constant grid from the origin to $R_o$ and introducing the transformation $r = R_o + x^2 + cx$ for $r > R_o$. This transformation, with proper choice of $R_o$, c, and increment, $\Delta x$, increases computing efficiency with no significant reduction in accuracy.

In comparison of the results from a variable and a fixed grid, the size of domain is 1000 km and the horizontal resolution for $r \leq 300$ km is 20 km in both experiments. For the variable grid, Experiment 14, the parameters of the transformation are $R_o$ equal to 300 km, c equal to 395.1 $m^{\frac{1}{2}}$, and $\Delta x$ equal to 43.6 $m^{\frac{1}{2}}$. The resolution varies from 20 km at 300 km to 73.3 km at 1000 km. The number of grid points is reduced from 51 to 31 and a 40 percent saving in the computational time is achieved. Initial conditions for the grid points beyond 300 km are interpolated from the profiles of the fixed grid.

Figure 51 shows the radial wind profiles after 400 iterations. Differences are extremely small; for example, the maximum inflow in the variable grid Experiment 14 is 18.18 m/sec compared to 18.19 m/sec in the fixed grid Experiment 13. The maximum tangential wind difference is 0.02 m/sec. Exact comparisons beyond 300 km are difficult because the grid points in the two experiments do not

coincide. However, the results agree very well and suggest that a further reduction in grid points may be possible without generating unacceptable errors. The excellent agreement between Experiments 13 and 14 justifies use of the variable grid as a reasonable and economically useful substitute for the constant grid.

4.4.3 High (10km) Resolution: Experiment 15

In the final experiment of a computational nature, Experiment 7 is repeated utilizing the variable grid. For $R_o$ equal to 150 km, c equal to 484.1 $m^{\frac{1}{2}}$, and $\Delta x$ equal to 19.85 $m^{\frac{1}{2}}$, the resolution varies from 10 km within 150 km of the center to 25 km at the outer boundary of 500 km. The number of grid points increases from 26 in Experiment 7 to 36 in Experiment 15. Because the time step must be halved to satisfy the linear computational stability requirement, an increase in computation time of 138 percent is required.

Figure 52 shows the tangential wind profiles after 400 and 800 iterations, respectively. The profiles for Experiment 15 are somewhat smoother near the radius of maximum wind than for Experiment 7. The maximum tangential wind is reduced from 39.28 m/sec in Experiment 7 to 38.65 m/sec in Experiment 15, while the maximum inflow decreases from 18.28 m/sec to 17.63 m/sec. These differences, which

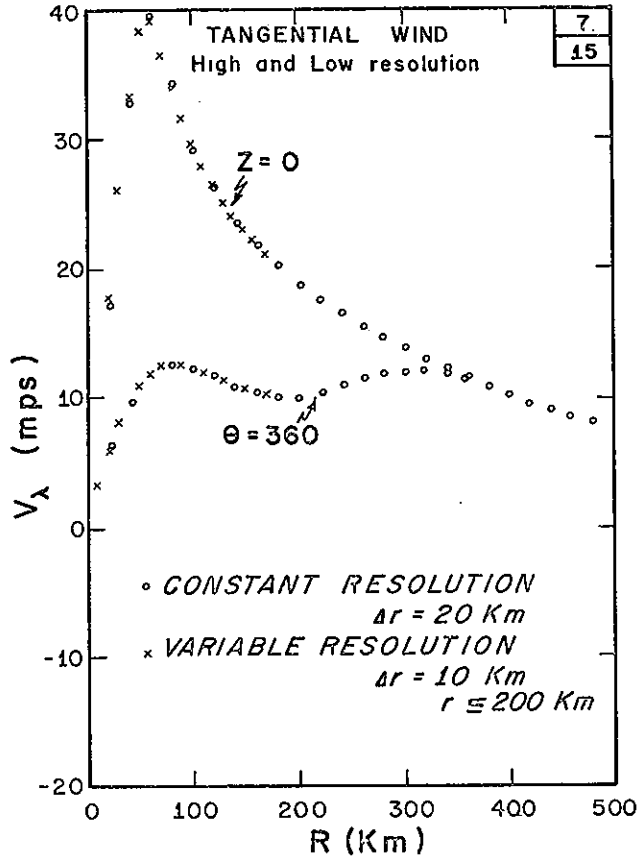


Figure 52. Tangential wind profiles in Experiments 7 and 15

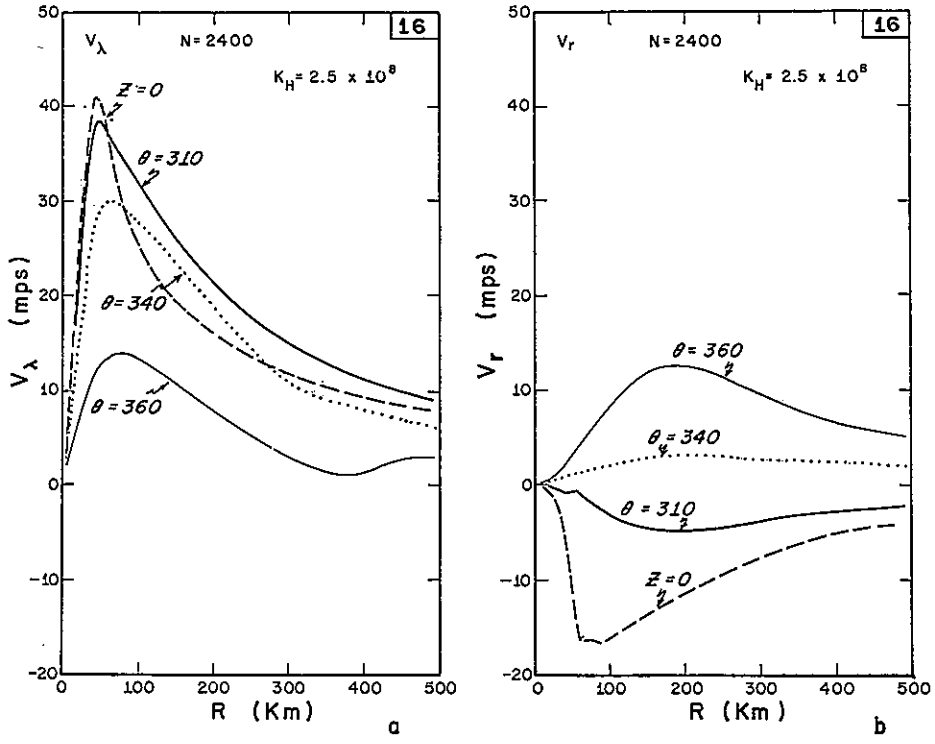


Figure 53. Tangential and radial wind profiles in Experiment 16

are about 2 percent, appear insignificant in view of the 138 percent increase in computational time.

The relatively small differences indicate that the heating function is adequately resolved by the 20 km resolution and support the results of all the 20 km experiments. If the radial variation of the heating function profile were altered by increasing the resolution, one would expect greater differences between the two experiments.

### 4.5 High Resolution Experiment with Reduced Horizontal Mixing: Experiment 16

After the preliminary series of experiments, a value for $K_H$ of $5 \times 10^8$ $cm^2 sec^{-1}$ was used in subsequent experiments. This value is considered somewhat large, but in separate experiments with 20 km resolution (app. A) non-linear instability develops for smaller values. However, finer grids more accurately resolve the shorter wavelengths, thus non-linear instability depends on grid size as well as internal mixing. To investigate the effect of decreasing the horizontal mixing coefficient from $5 \times 10^8$ to $2.5 \times 10^8$ $cm^2 sec^{-1}$, the variable grid of Experiment 15 with 10 km resolution near the center and the heating function of Experiment 7 is utilized.

4.5.1 Momentum and Temperature Structures

Figure 53 shows the slowly varying tangential and radial wind profiles for Experiment 16 which should be compared to those for Experiment 7 (fig. 28). The maximum tangential wind increases from 33 to 41 m/sec in Experiment 16 and the radius of maximum wind shifts inward from 60 to 40 km. Maximum inflow increases from 15 to 17 m/sec. The irregularity in the radial wind profile at 70 km indicates that the resolution in this region is insufficient to adequately resolve the extremum. In the boundary layer experiments (app. A), this type of oscillation developed before the onset of non-linear instability. In Experiment 16, however, the interactions with the mass and momentum distributions prevent this oscillation from amplifying. The temperature structure shows a more concentrated warm core in Experiment 16 (fig. 54) than in Experiment 7 (fig. 43), with a maximum temperature increase of $3^{o}C$.

The circulation in Experiment 16 is the strongest of all the experiments and compares realistically with empirical results. Figures 55 and 56 show cross sections of the tangential and radial wind. The tangential circulation is stronger and more concentrated near the center than in Experiment 7 (fig. 29). The weak upper level anticyclone at 500 km in Experiment 7 is not present because the cyclonic

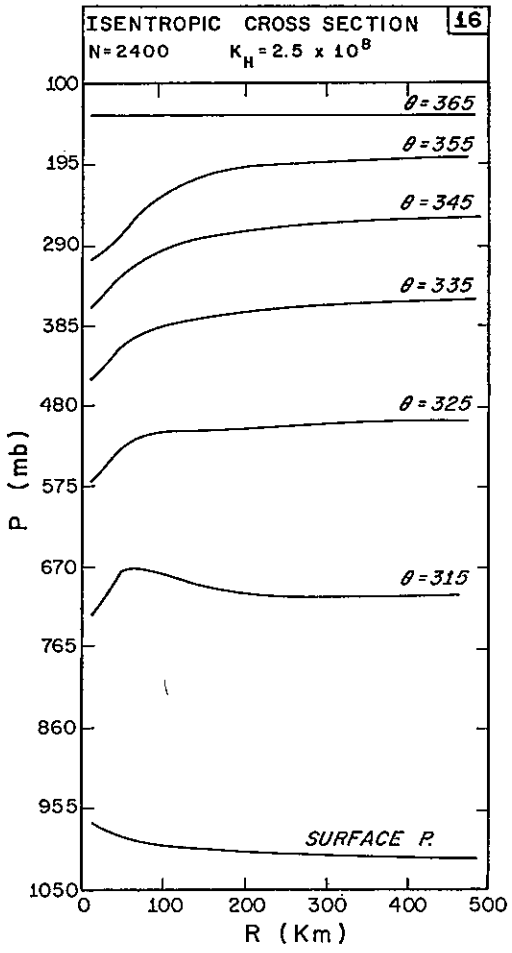


Figure 54. Isentropic cross section in Experiment 16

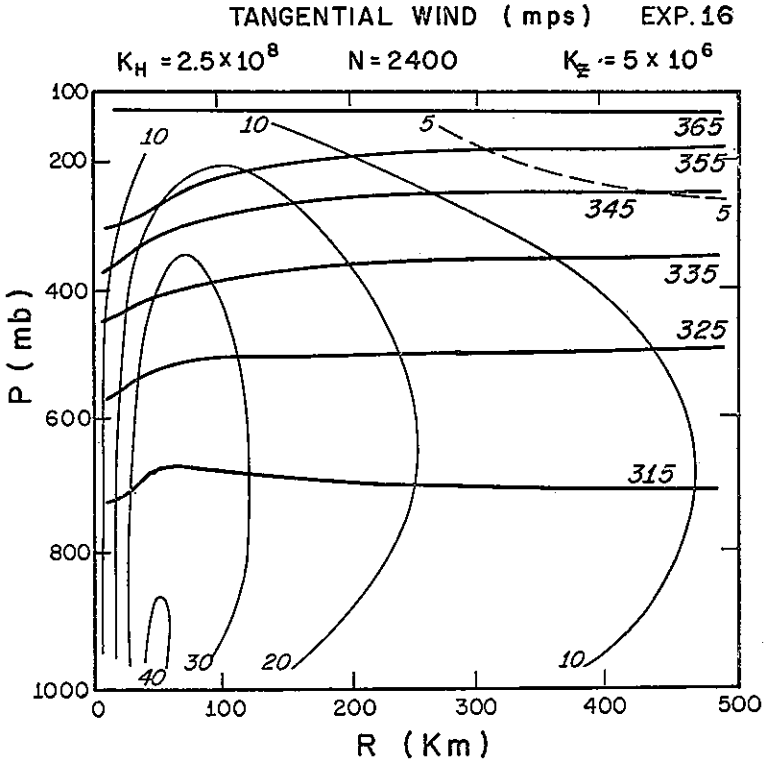


Figure 55. Tangential wind cross section in Experiment 16

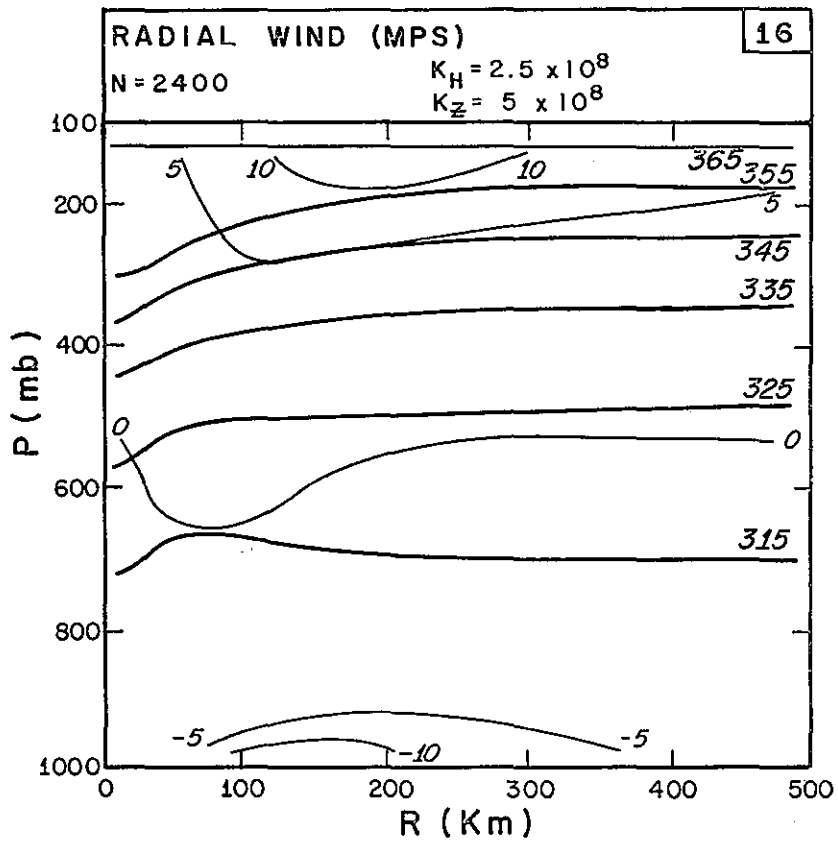


Figure 56. Radial wind cross section in Experiment 16

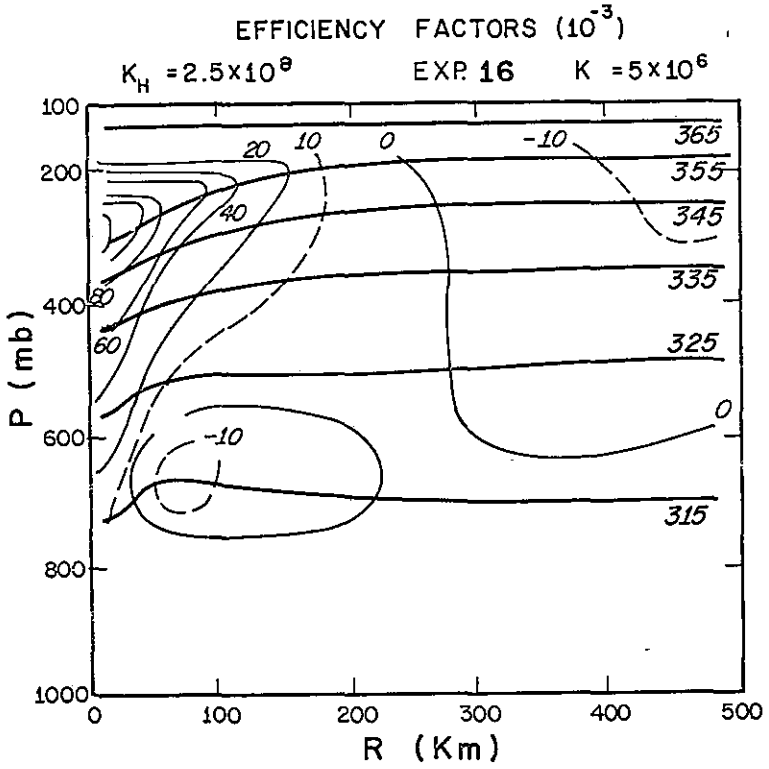


Figure 57. Isentropic and efficiency factor cross section in Experiment 16

circulation in the upper levels near the center is stronger in Experiment 16, so that the radius at which the relative circulation becomes anticyclonic is greater. This result, and the strong dependency of the upper level outflow on the horizontal heating distribution found earlier, suggests that relatively weak storms with large diameters should be accompanied by stronger upper level anticyclones than smaller, more intense storms.

### 4.5.2 Energy Budget

The efficiency factor cross section for Experiment 40 (fig. 57) shows positive efficiency factors in the middle and upper troposphere extending from the center to 300 km. Negative efficiency factors occur in the lower levels near the center and in the upper levels beyond 300 km. In figure 58, almost all the generation occurs inside 200 km and above 600 mb.

The energy budget shown in figure 59 and the total budget summarized in table 2 are quite similar to the results from Experiment 7 (fig. 33). As expected, the total frictional dissipation is reduced because the horizontal mixing is less in Experiment 16. Thus the steady-state condition implies that the total generation and conversion of available energy will also be less, even though the maximum winds are higher.

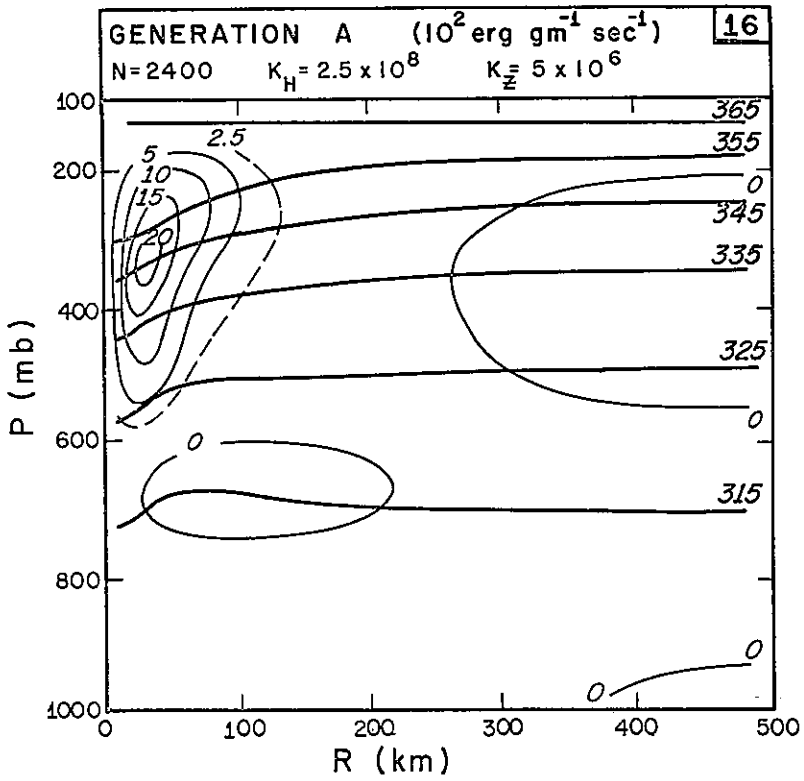


Figure 58. Generation of available potential energy in Experiment 16

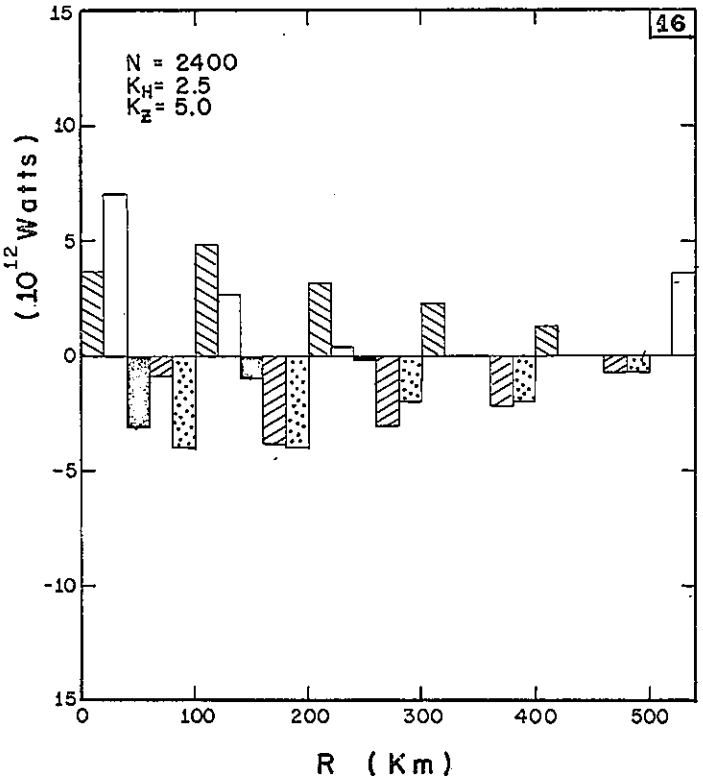


Figure 59. Energy budget for Experiment 16 (see fig. 33 for key).

## 4.6 Comparison of Numerical and Empirical Pressure and Wind Relationship

Empirical evidence (Colón, 1963) indicates a close relationship between central pressure and maximum wind speed. Figure 60 shows the model results from five experiments superimposed on Colón's data. Central pressure in the model is defined as the pressure at the first prediction point for pressure, which is either 5 or 10 km. All points from the model experiments lie within a region that bounds the empirical data.

The relationship between central pressure and radius of maximum wind is another aspect of the model to be compared with Colón's (1963) data (fig. 61). Colón discusses two types of storms. The "Daisy type," represented by dots in figure 61, is small and shows little relationship between central pressure and radius of maximum wind. The "Helene type" storm, represented by x's in figure 61, is larger and shows an increasing radius of maximum wind with increasing central pressure. From figure 61, we see that storms produced by this model appear to fit the "Helene type."

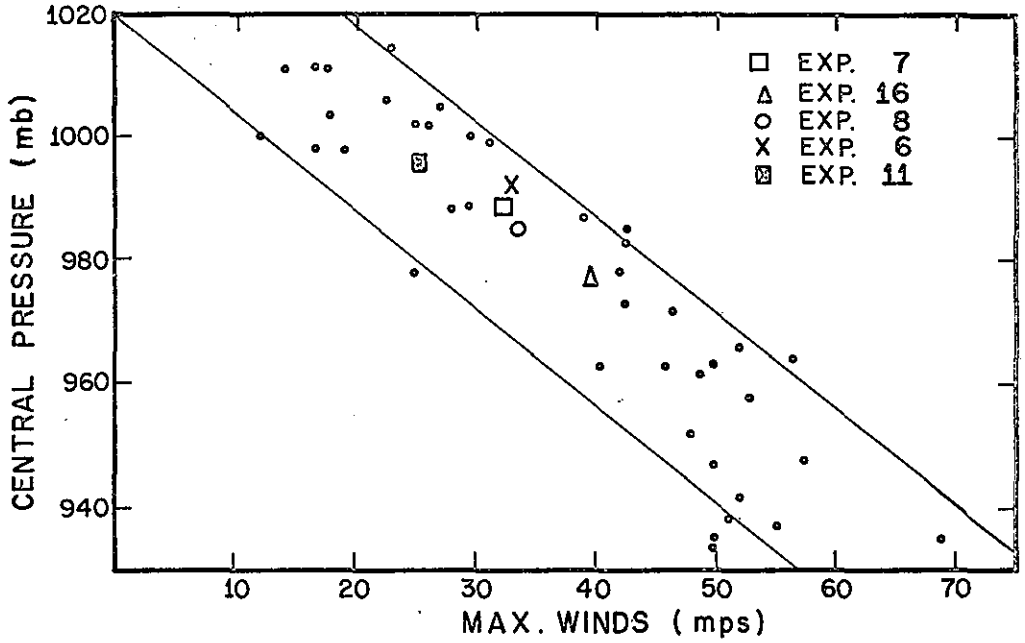


Figure 60. Scatter diagram of maximum surface winds versus central pressure for empirical data (Colón, 1963) and model Experiments 6, 7, 8, 11, and 16.

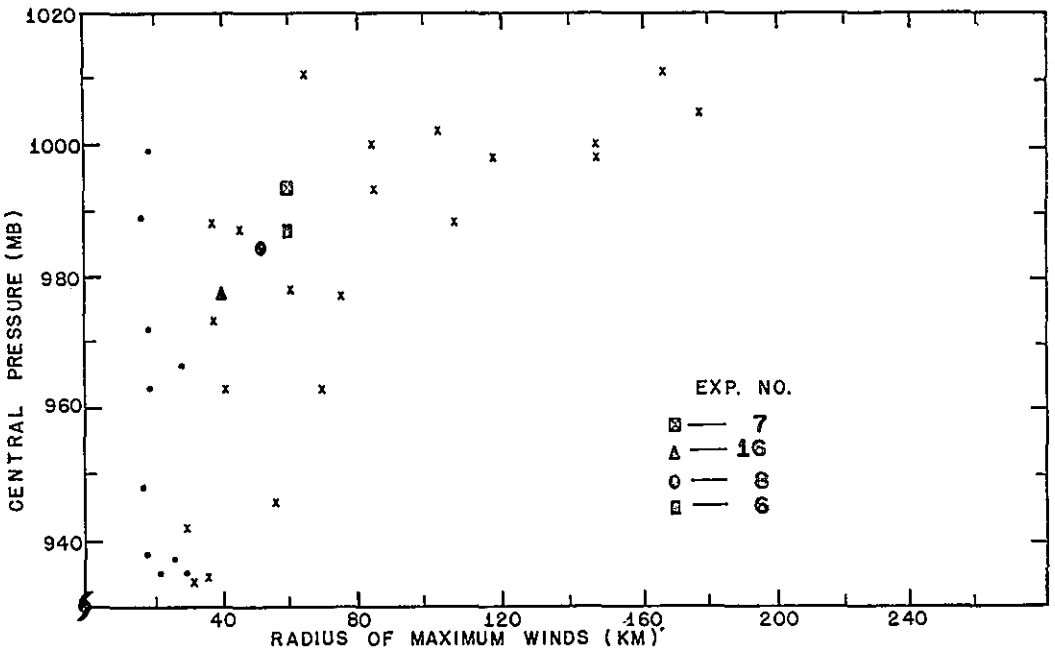


Figure 61. Scatter diagram of radius of maximum surface winds versus central pressure for empirical data (Colón, 1963) and model Experiments 6, 7, 8, and 16.

The degree of gradient balance throughout the storm system has received attention from investigators, e.g., Hawkins and Rubsam (1968). Their results show that the inner region is fairly close to gradient balance. In these experiments, except for the winds near the surface which are sub-gradient by 20 to 40 percent and in the outflow layer where radial advection is important, gradient balance is closely approximated. Models with low vertical resolution may have outflow layers closer to gradient balance, because horizontal advection in a deeper outflow layer will be much weaker.

## 5. CONCLUSIONS AND SUGGESTIONS FOR FUTURE RESEARCH

A diagnostic model in isentropic coordinates has been developed to study the energetics and dynamics of the steady-state, mature tropical cyclone. Realistic, slowly varying solutions for the mass and momentum fields are obtained by an iterative technique for the thermal forcing specified by several heating distributions. The principle conclusions are:

(1) The magnitude and distance of the maximum wind from the center is determined primarily by the heating inside 100 km. Large variations in heating beyond 100 km have little effect on the maximum wind but produce considerable changes in the outflow intensity. Because angular momentum tends to be conserved in the outflow layer, the size and intensity of the upper level anticyclone is also closely related to the heating at large distances from the center.

(2) In experiments in which the vertical variation of heating is proportional to the condensation of water vapor along a moist adiabat, the temperature structure shows an unrealistically low warm core and a deep, weak outflow layer. A vertical distribution that releases a higher proportion of heat in the upper troposphere gives more realistic results.

(3) Radiational cooling in clear air is calculated for several moisture distributions in the tropics using Sasamori's

(1968) model. Infrared cooling beyond 300 km causes a 1.5 m/sec increase in maximum wind speed and a 6 percent increase in generation of available potential energy. In this model, the total heat loss by radiation on a scale of 1000 km is about one half to a third of the total heat gain.

(4) In experiments with a constant horizontal eddy coefficient and a vertical mixing coefficient that decreases linearly with height, values of $K_H$ greater than $5 \times 10^8$ $cm^2 sec^{-1}$ result in unreasonably diffuse storms and values of $K_z$ less than $1 \times 10^6$ $cm^2 sec^{-1}$ produce storms with too much vertical shear. Most reasonable results are obtained for $K_H$ equal to 2.5 and $5 \times 10^8$ $cm^2 sec^{-1}$ and $K_z$ equal to $5 \times 10^6$ $cm^2 sec^{-1}$.

(5) In the slowly varying states, the generation and boundary flux of available potential energy, conversion to kinetic energy, and dissipation of kinetic energy by surface and internal friction are balanced. Paradoxically, therefore, experiments with the most internal friction contain the most kinetic energy. The relationship between low-level inflow, high-level outflow, and the warm core structure produce a positive boundary contribution to the available potential energy budget. On a scale of 500 km, this boundary term is nearly as large as the generation term in some experiments. On a scale of 1000 km, however, the generation is an order of magnitude greater.

(6) In the computational experiments, it is established that a 500 km domain and 20 km resolution are satisfactory for the latent heating functions studied. A variable grid is utilized in some experiments to economically gain higher resolution near the center. For a 40 percent gain in computational time, differences in maximum wind are less than 0.1 percent using the variable grid.

(7) In a separate series of experiments (app. A), the steady-state vertical velocities at the top of the boundary layer are computed for a constant pressure gradient. Results are highly dependent on the amount of explicit mixing and on the finite difference scheme used. The upstream differencing technique with no explicit diffusion produces results similar to those from centered differencing using a constant horizontal mixing coefficient of $10 \times 10^8$ $cm^2$ $sec^{-1}$.

(8) The iterative technique for obtaining steady-state solutions is a powerful numerical technique that has relatively few restrictions. Although the steady-state mass and momentum fields are determined from prescribed heating functions, the method could easily be applied with different dependent and independent variables. For example, the momentum and heating distributions could be obtained for a time invariant mass (temperature) distribution.

(9) Isentropic coordinates may be effectively used in numerical models and are particularly effective in studying adiabatic and diabatic effects.

Although the results presented have shown that the size and intensity of the tropical cyclone is directly linked to thermal forcing, the question of what determines the heating profiles has not been investigated. Large-scale synoptic features such as sea and environment temperatures, and horizontal and vertical shears are all important in determing the distribution of convection which leads to the development and maintenance of the tropical storm. Theoretical investigation of these properties will require more sophisticated numerical models to describe the delicate balance of for in the early stages of hurricane development.

Future research should be directed toward developing three dimensional models to study the role of asymmetries in the the hurricane. A better understanding of such physical processes as cloud-scale and large-scale latent heating, momentum transport by cumulus clouds, and sea-air interactions are necessary for more realistic hurricane models.

## 6. ACKNOWLEDGEMENTS

This work is essentially the author's Doctorate thesis from the University of Wisconsin. The author extends his sincere thanks to his advisor, Dr. Donald R. Johnson, for his continuing interest, helpful suggestions, and many profitable discussions throughout the course of this research.

The author also wishes to thank Dr. Stanley L. Rosenthal, National Hurricane Research Laboratory (NHRL), for his many helpful ideas at various stages of this research. The author is also grateful to Dr. R. Cecil Gentry, Director of NHRL, for the opportunity to work at NHRL and use its computing facilities.

Thanks are also due to the author's reading committee, Professor Werner Schwerdtfeger and Dr. John Young for their helpful suggestions.

# APPENDIX A - Numerical Experiments to Estimate Boundary Layer Vertical Motion

## A1. INTRODUCTION

Because of frictional convergence in the boundary layer and the condition that the mixing ratio decreases rapidly with height, the major water vapor convergence in the tropical cyclone occurs in the lower troposphere. It is important, therefore to accurately estimate the frictionally induced vertical motion at the top of the planetary boundary layer. Approximate expressions relating this vertical motion to the mean steady-state tangential wind have been given by several investigators, e.g., Syōno (1950, 1951), Charney and Eliassen (1964), and Ogura (1964). In this appendix a numerical technique is used to evaluate the vertical velocity under a steady-state pressure gradient force. Using the Matsuno (1966) simulated backward difference method, the effect of lateral mixing on the steady-state solution is studied by comparing results from constant and variable, non-linear eddy coefficients with horizontal resolutions of 20, 10, and 5 km. Finally, the steady-state vertical velocities obtained by this method are compared with those calculated from the approximate formulation (Ogura, 1964)

$$\omega_t = -\frac{g}{r}\frac{\partial r \zeta_a / f_a}{\partial r} \quad . \qquad \text{(A-1)}$$

Besides yielding useful information on the vertical motion which may be used as boundary conditions in diagnostic models such as Barrientos (1964) or Anthes (1970), these results from a relatively simple model are useful in interpreting results from the more complex diagnostic hurricane model.

## A2. BASIC EQUATIONS

On the assumption of axisymmetry and the neglect of vertical advection, the equations of motion for the tangential and radial winds are

$$\frac{\partial rv_\lambda}{\partial t} = -v_r \frac{\partial rv_\lambda}{\partial r} - frv_r + r\left\{ -\frac{C_D \rho \zeta |V| v_\lambda}{\Delta P} + \frac{1}{r^2}\frac{\partial\left[K_H r^3 \frac{\partial v_\lambda / r}{\partial r}\right]}{\partial r}\right\} \tag{A-2}$$

$$\frac{\partial v_r}{\partial t} = -v_r \frac{\partial v_r}{\partial r} + fv_\lambda + \frac{v_\lambda^2}{r} - \frac{\partial \phi}{\partial r} - \frac{C_D \rho \zeta |V| v_r}{\Delta P} + \frac{1}{r}\frac{\partial\left[K_H r^3 \frac{\partial v_r / r}{\partial r}\right]}{\partial r} \tag{A-3}$$

The last two terms in (A-2) and A-3 represent the surface drag and the horizontal mixing. The symbol notation is consistent with the prior notation. Equations (A-2) and (A-3) are solved using the Matsuno iterative technique described earlier for the steady-state values of $v_\lambda$ and $v_r$ for a constant pressure gradient force. The tangential and radial winds are forecast for the center of the boundary layer of constant depth, $\Delta P$. The "vertical motion" at the top of the

boundary layer obtained from the finite difference form of the continuity equation, is

$$\left(\frac{\omega_t - \omega_o}{\Delta P}\right)_{j+\frac{1}{2}} = - \frac{(rv_r)_{j+1} - (rv_r)_j}{r_{j+\frac{1}{2}}\,(r_{j+1} - r_j)} \quad , \qquad \text{(A-4)}$$

where j and $j+\frac{1}{2}$ refer to the horizontal grid. The boundary conditions are zero divergence and relative vorticity at 500 km and $\omega_o$ equal to zero at the earth's surface. The initial conditions (first guess) are a tangential wind in gradient balance and zero radial velocity. The gradient wind corresponding to the constant pressure gradient force is shown in figure A1.

## A3. CENTERED DIFFERENCING AND CONSTANT MIXING COEFFICIENT

The first series of experiments assumes various constant horizontal mixing coefficients and uses centered differences for the advective terms in (A-2) and (A-3). Figure A1 shows the steady-state radial profiles of $v_\lambda$ , $v_r$ and $\omega_t$ for a horizontal resolution of 20 km, and values of $K_H$ ranging from 10 to 100 x $10^8$ $cm^2$ $sec^{-1}$. These values are higher than those summarized in table 2 (page 36). However, for the 20 km resolution and centered differencing, smaller values of $K_H$ resulted in oscillations which preceeded the development of non-linear instability (Phillips, 1959).

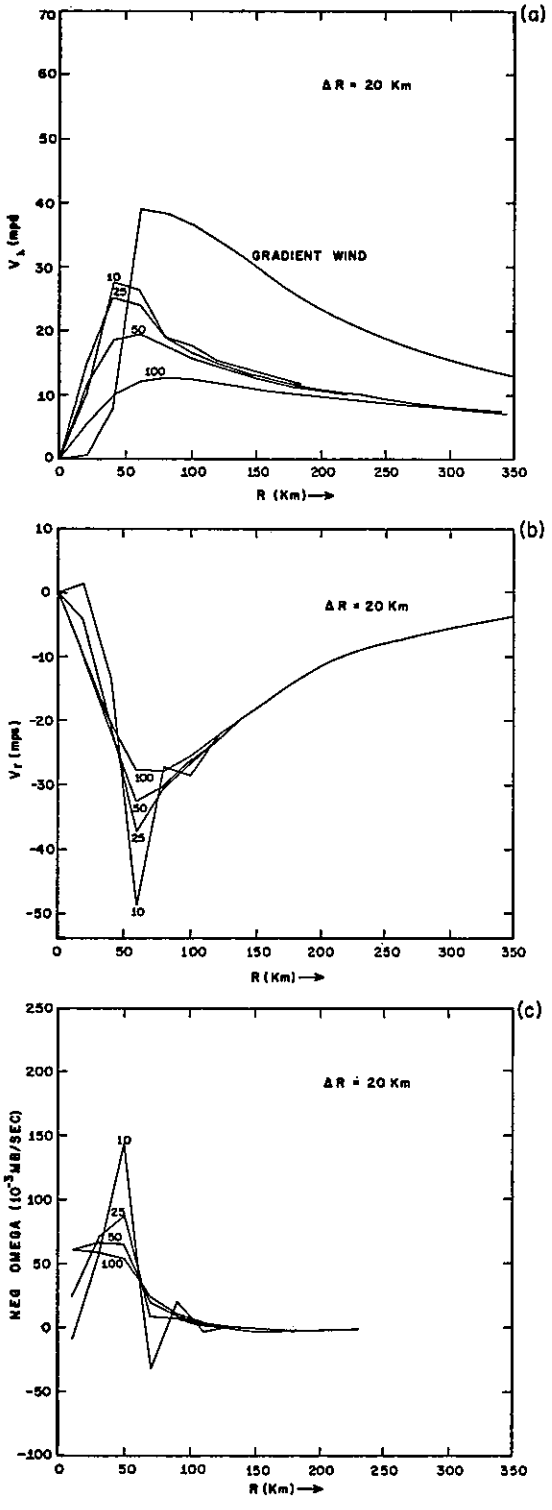


Figure A-1. Steady-state tangential and radial winds and vertical motion for various mixing coefficients ($10^8 cm^2 sec^{-1}$) and centered differencing (Δ r=20 km)

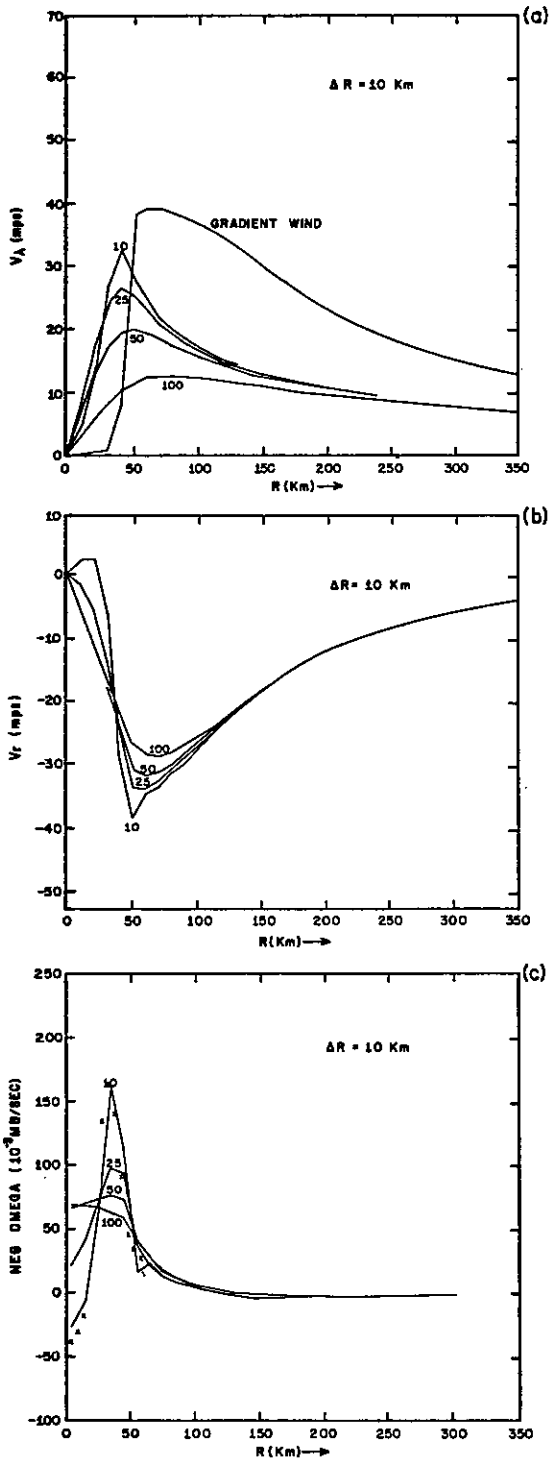


Figure A-2. Steady-state tangential and radial winds and vertical motion for various mixing coefficients ($10^8 cm^2 sec^{-1}$) and centered differencing (Δ r=10 km)

Several features in the tangential wind profile (fig. A1a) are noteworthy. For all values of $K_H$, the tangential wind beyond the radius of maximum wind is sub-gradient by about 50 percent, due primarily to surface friction. The effect of the lateral mixing is important only in the vicinity of the maximum wind. Beyond 100 km the results are relatively insensitive to variations in $K_H$. The radius of the maximum wind shifts inward by 20 km for the smaller values of $K_H$.

It is interesting to note that the radial and tangential components are the same order of magnitude; in fact, the inflow angle (angle of departure from gradient balance) is greater than $50^\circ$ in the inner region of the storm. Rosenthal (1969) also found inflow angles greater than $45^\circ$ in his hurricane model. While this magnitude is larger than magnitudes found in empirical studies, Rosenthal notes that most observations are from above the boundary layer.

The effect of varying the lateral mixing on the radial winds is also significant. The maximum inflow varies from 49 m/sec for $K_H$ equal to $10 \times 10^8$ to 28 m/sec for $K_H$ equal to $100 \times 10^8$ $cm^2 sec^{-1}$. The initiation of non-linear instability is indicated by the oscillations in the $v_r$ profile for $K_H$ equal to $10 \times 10^8$ $cm^2 sec^{-1}$. These are space oscillations and are analogous to standing waves, because the truncation

inherent in the Matsuno technique damps the time oscillations.

Because $\dot{\omega}_t$ is calculated from the differences of $v_r$, the oscillations are most pronounced in the vertical velocity profile shown in figure A1c. For very large mixing coefficients, the upward motion occurs in a broad maximum extending inward to 10 km. As $K_H$ decreases, however, a distinct maximum of rising motion occurs at about 50 km. The maximum upward velocity is approximately 150 cm/sec for $K_H$ equal to $10 \times 10^8$ $cm^2 sec^{-1}$. At 10 km sinking motion is observed for $K_H$ equal to $10 \times 10^8$ $cm^2 sec^{-1}$. The mean subsidence beyond 150 km is about 2 cm/sec.

In the centered differencing experiments with 20 km resolution, a constant mixing coefficient equal to or exceeding $25 \times 10^8$ $cm^2 sec^{-1}$ was required to maintain smooth profiles for the intense pressure gradient. This value is large compared to earlier estimates (table 2, page 36). Results from the succeeding experiments show that this difficulty is resolved by either increasing the horizontal resolution, using non-linear mixing coefficients, or using upstream differencing.

Figure A2 shows the radial profile of $v_\lambda$, $v_r$, and $\dot{\omega}_t$ for various values of constant $K_H$ and a horizontal resolution of 10 km. The higher resolution is adequate to describe the

sharp extrema in the profiles for the smaller values of $K_H$. The differences between the 10 and 20 km resolution experiments are most pronounced in the radial and vertical velocity profiles. For $K_H$ equal to 10 x $10^8$ $cm^2 sec^{-1}$, $v_r$ is reduced from 49 to 39 m/sec at 60 km and the oscillations are greatly reduced.

The vertical motion profile in the higher resolution experiment is also more satisfactory. The radius of maximum upward motion shifts inward from 50 to 35 km for $K_H$ equal to 10 x $10^8$ $cm^2$ sec-1 and the oscillations are less pronounced. The subsidence maximum of about 25 cm/sec near the center is better resolved.

To investigate the effect of increasing the resolution still further, one experiment was completed with a horizontal resolution of 5 km and $K_H$ equal to 10 x $10^8$ $cm^2 sec^{-1}$. The $\omega_t$ profile for this experiment is indicated in figure A2c by the symbol x. Differences between the $\omega_t$ values from the 5 and the 10 km resolution experiments are small and do not justify the four-fold increase in computational time.

## A4. UPSTREAM DIFFERENCING

The forward-time, one-sided (upstream) space differencing scheme is frequently used in numerical models because of

its speed, simplicity, and stability. However, the truncation error of this scheme causes artifical damping, particularly of the short wave-lengths (Molenkamp, 1968).

Figure A3 shows the results from three experiments using upstream differencing. In contrast to the experiments with centered differencing, there is no evidence of oscillations or non-linear instability. An estimate of the damping is made by comparing two experiments, one with no explicit damping ($K_H$ equal to zero) and one with explicit as well as artificial damping ($K_H$ equal to $10 \times 10^8$ $cm^2$ $sec^{-1}$). The maximum tangential and radial winds differ by only 1 and 1.5 m/sec, respectively. The shapes of the vertical motion maxima are somewhat different, but the magnitudes are quite similar. In both the 20 km and 10 km resolution experiments, the tangential and radial wind profiles from the upstream differencing experiments are most similar to those from the centered differencing experiments with $K_H$ equal to $10 \times 10^8$ $cm^2 sec^{-1}$ (compare figs. A1, A2 and A3).

Although the profiles for both the one-sided and centered differencing experiments for $K_H$ equal $10 \times 10^8$ $cm^2 sec^{-1}$ and $\Delta r$ equal to 10 km are similar, there is an important difference. In the experiments with explicit diffusion, a distinct region of sinking motion occurs near the center. This subsidence is not observed in the upstream

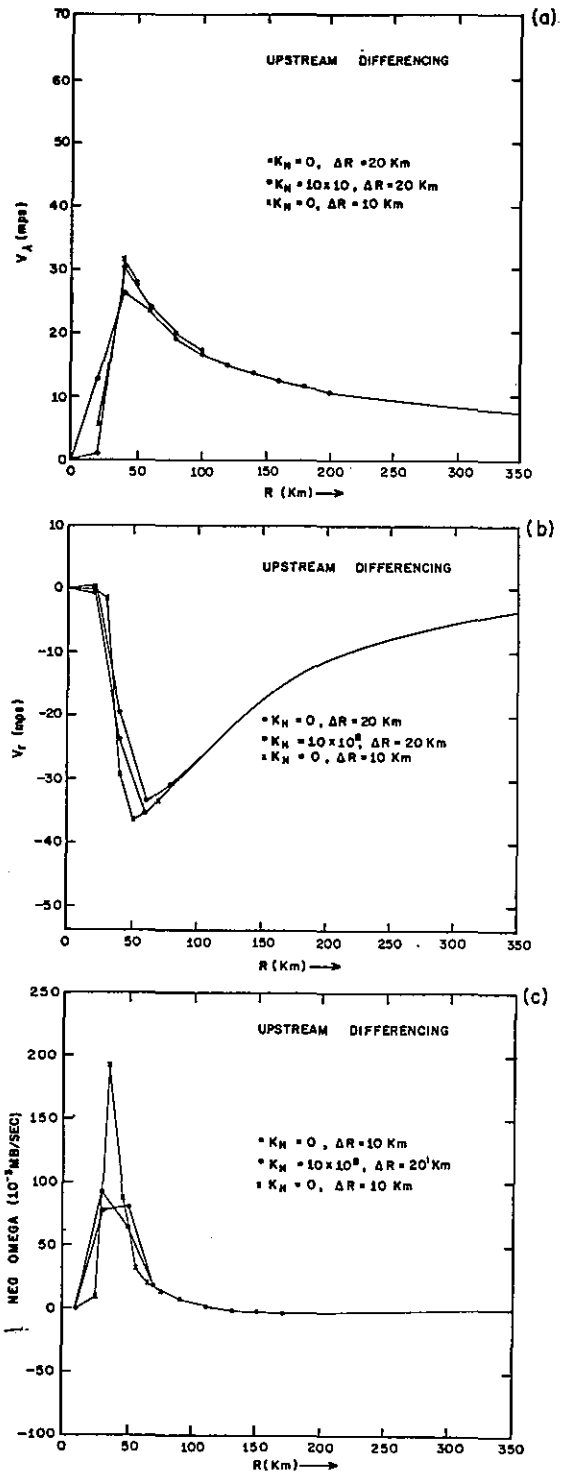


Figure A-3. Steady-state tangential and radial winds and vertical motion for various mixing coefficients ($10^8 cm^2 sec^{-1}$) and upstream differencing.

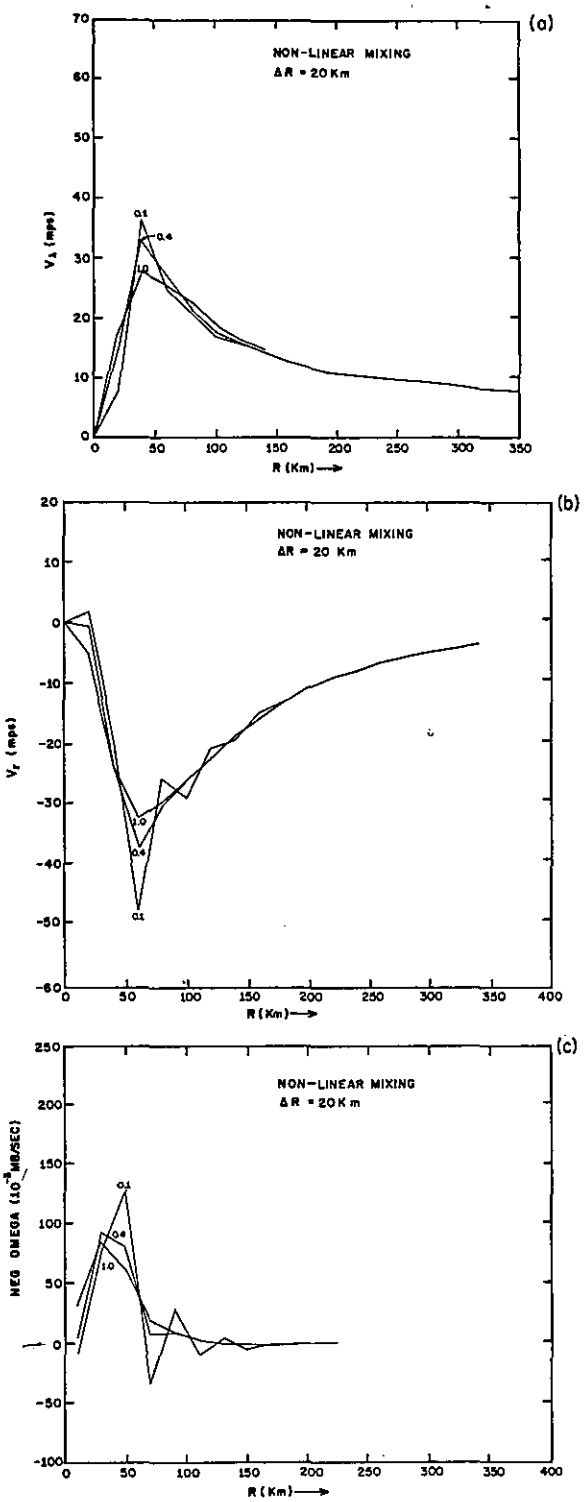


Figure A-4. Steady-state tangential and radial winds and vertical motion for various non-linear mixing coefficients and centered differencing ($\Delta$ r=20 km)

differencing experiments. The implicit diffusion of upstream differencing depends on truncation in the advection terms. Inside the radius of maximum wind the radial advection is small, so there is little implicit mixing even though gradients are large. If the horizontal mixing process is important in the eye formation, it is necessary to include explicit mixing in this region.

Kuo (1959) attributed subsidence inside the eye of the hurricane to the effect of horizontal eddies. These eddies cause a net mass transport into the convection in the eyewall and subsidence results from mass continuity requirements. The reasons for the subsidence in these experiments, however, must be somewhat different, because vertical advection has been neglected. Apparently, for a range of values of $K_H$, tangential momentum is mixed into the "eye" causing an excess of centripetal over pressure gradient force and an outward flow. In the experiments with upstream differencing and no explicit mixing, the advection is small inside the radius of maximum tangential wind. Very little mixing occurs and no subsidence is observed. For very large mixing, the tangential wind maximum is reduced and the mixing of radial momentum is sufficient to allow inflow all the way to the center.

## A5. CENTERED DIFFERENCING AND NON-LINEAR HORIZONTAL MIXING

Because the mixing in upstream differencing depends on the truncation error, it is important to use a conservative finite difference scheme and include a known amount of explicit mixing. Non-linear mixing coefficients have been successfully used in numerical models to damp the extremely short waves without unduly damping meteorologically significant waves. In this section steady-state solutions are computed using centered differencing and non-linear mixing coefficients.

The non-linear lateral diffusion for sub-grid scale mixing is modelled after Smagorinsky et al., (1965). For cylindrical coordinates (Rosenthal, 1969, personal communication) and the assumption of symmetry, the mixing coefficient is

$$K_H = k_o^2 \triangle r^2 |D| \quad , \tag{A-5}$$

where the magnitude of deformation is

$$|D| = r\left\{\left(\frac{\partial v_{r/r}}{\partial r}\right)^2 + \left(\frac{\partial v_{\lambda/r}}{\partial r}\right)^2\right\}^{\frac{1}{2}} \tag{A-6}$$

The non-dimensional parameter, $k_o$, is of order unity and is analogous to the Karman constant.

Figures A4 and A5 show the $v_\lambda$ , $v_r$, and $\omega_t$ profiles for several values of $k_o$ ranging from 0.33 to 1.0 and for resolutions of 20 and 10 km. The profiles for $k_o$ equal to 0.33 display large oscillations in the radial and vertical motion profiles and are unsatisfactory. The profiles for $k_o$ equal to 0.64 show smaller amplitude oscillations, while the profiles for $k_o$ equal to 1.0 are smooth. Significantly, the mean shapes and amplitudes of the profiles are not drastically changed for all values of $k_o$. In contrast, the extrema in the profiles for the constant coefficient experiments are greatly reduced as $K_H$ is increased.

The vertical motion profiles for the non-linear mixing experiment with $k_o$ equal to 1.0 and for the constant coefficient experiment with $K_H$ equal to $10 \times 10^8$ $cm^2 sec^{-1}$ are quite similar. In both experiments subsidence occurs inside 20 km, upward motion of about 150 cm/sec occurs at 35 km, and subsidence of 1-2 cm/sec occurs beyond 115 km.

## A6. COMPARISON OF ITERATIVE WITH APPROXIMATE VERTICAL VELOCITIES

Equation (A1) has been used in studies of tropical cyclones to estimate the vertical motion at the top of the boundary layer, e.g., Ogura (1964) and Anthes and Johnson (1968). However, when the absolute vorticity, $\zeta_a$ , which appears in the denominator tends to zero, the approximation

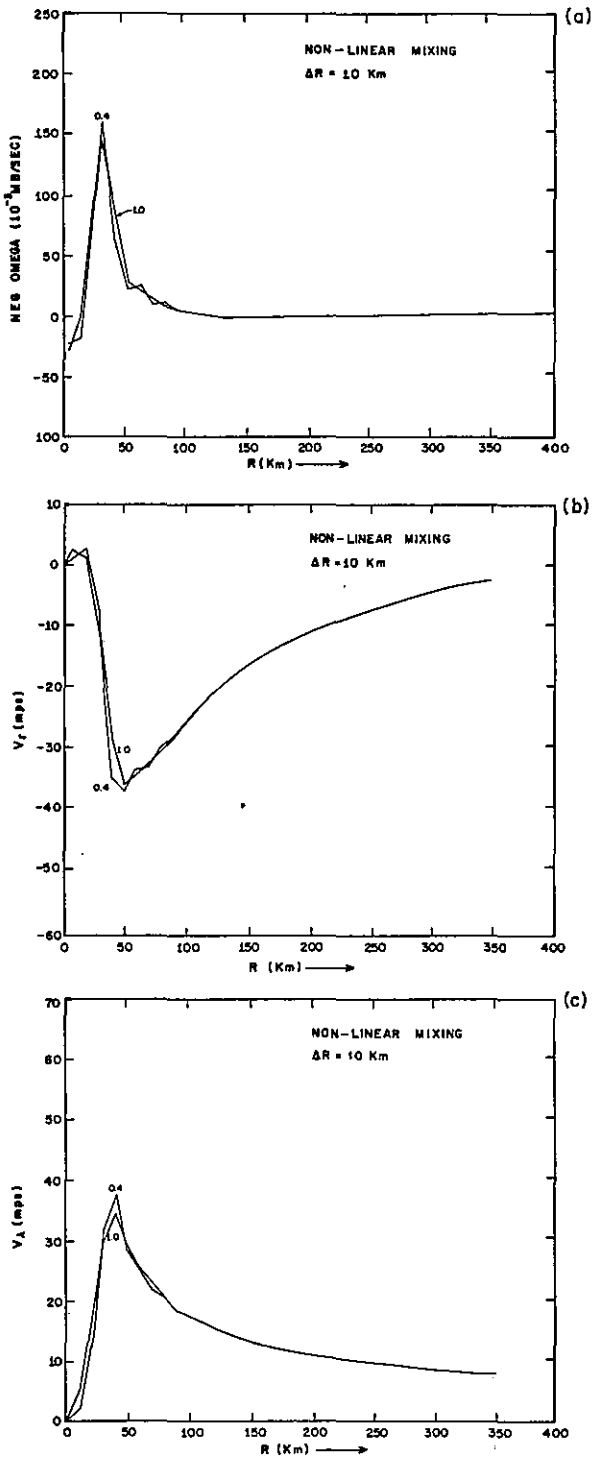


Figure A-5. Steady-state tangential and radial winds and vertical motion for various non-linear mixing coefficients and centered differencing ($\Delta$ r=10 km)

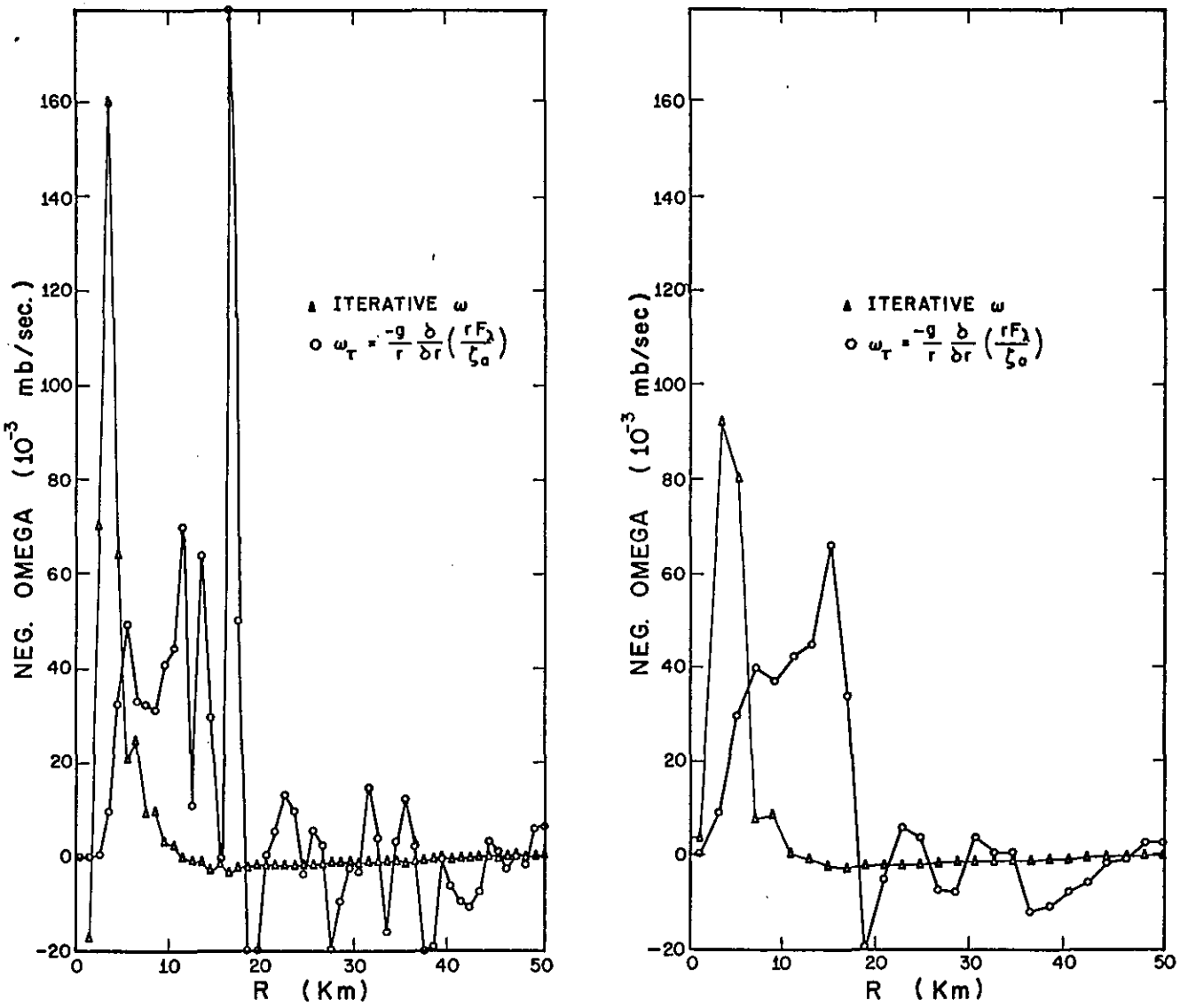


Figure A-6. Iterative and approximate vertical velocities ($\omega$) for 20 km (a) and 10 km (b) resolution

is invalid. Figure A6 compares the approximate vertical velocities using the gradient wind to evaluate $\zeta_a$ and $\gamma_a$ in (A-1) and those computed iteratively from the non-linear viscosity experiment with $k_o$ equal to 0.64. Although the approximate formula yields rising motion of a reasonable magnitude, the radius of maximum updraft is considerably larger than that in the iterative solution. More significant are the large oscillations beyond 200 km in the approximate profile. These oscillations are noise which result from the sensitivity of (A-1) to minor variations in $\zeta_a$ when $\zeta_a$ is small. Therefore this approximation should be used with caution.

## A7. SUMMARY

In this appendix an iterative technique was used to estimate the steady-state vertical motion at the top of the boundary layer under a constant pressure gradient force. The following conclusions are summarized:

(1) For centered space differencing, constant mixing coefficients of 25 and 10 x $10^8$ $cm^2 sec^{-1}$ are required to control short wave oscillations that lead to non-linear instability for horizontal resolutions of 20 and 10 km, respectively.

(2) A significant difference between the 20 and 10 km resolution experiments was observed, but there was relatively

little difference between the 10 and 5 km resolution experiments.

(3) In the constant mixing coefficient experiments subsidence occurs inside the radius of maximum wind for $K_H$ equal to $10 \times 10^8$ $cm^2 sec^{-1}$. For higher values of $K_H$ the subsidence is not observed.

(4) In experiments with upstream space differencing, truncation error provides artificial damping that completely controls short wave oscillations and non-linear instability, even with no explicit mixing.

(5) Subsidence occurs near the center in experiments with explicit mixing but not in those without explicit mixing.

(6) Several experiments with a non-linear mixing coefficient gave satisfactory results by effectively eliminating the non-linear instability without over-damping the meteorologically significant extrema.

(7) Vertical motion profiles computed with the iterative technique show little resemblance to the profiles computed from Ogura's (1964) approximate expression. In the region where the iterative technique yields a smooth profile with weak subsidence of about 2 cm/sec, the approximate expression yields a rapidly oscillating profile of vertical motion with an amplitude of about 1 m/sec.

## APPENDIX B - STABILITY ANALYSIS OF FINITE DIFFERENCE SCHEME FOR ISENTROPIC MODEL

Because the computational stability theory for the complex set of non-linear equations has not been developed, it is necessary to derive separate conditions on various combinations of linearized terms in the model equations. Experience indicates that if one or more of the linear stability requirements is violated, the complete set of non-linear equations will usually be unstable. Therefore, the time step, $\Delta t$, is chosen to satisfy the most stringent linear stability requirement. The analysis for this requirement is presented in this appendix, and is determined from the combination of the continuity equation and the radial equation of motion. The simplified form of these equations are

$$\frac{\partial \frac{\partial P}{\partial \theta}}{\partial t} = -\frac{1}{r}\,\frac{\partial r v_r \frac{\partial P}{\partial \theta}}{\partial r} \quad , \tag{B-1}$$

$$\frac{\partial v_r}{\partial t} = -\frac{1}{\rho}\,\frac{\partial P}{\partial r} \quad , \tag{B-2}$$

where P is the surface pressure. An integration over the depth of the model and the neglect of the 1/r term in (B-1) yields

$$\frac{\partial v_r}{\partial t} = -\frac{1}{\bar{\rho}}\,\frac{\partial P}{\partial r} \quad , \tag{B-3}$$

$$\frac{\partial P}{\partial t} = -\frac{}{\Delta P}\,\frac{\partial v_r}{\partial r} \quad , \tag{B-4}$$

where $\overline{\Delta P}$ is defined to be the mean surface pressure, $\overline{P}$, minus the pressure of the uppermost isentropic surface, $P_t$. In the model, $\frac{\partial P_t}{\partial t}$ is zero.

Now denote values of radial velocity and pressure at step n by $v_r^n$ and $P^n$, respectively. The first guesses of $v_r^{n+1}$ and $P^{n+1}$ (designated by $^*$ ) by the Matsuno technique are

$$V^*_{r_j} = v^n_{r_j} - \frac{\Delta t}{\bar{\rho}\, 2\Delta r}\left( P^n_{j+1} - P^n_{j-1}\right) \quad , \tag{B-5}$$

$$P^*_j = P^*_j - \frac{\Delta t}{2\Delta r}\,\overline{\Delta P}\,\left(V^n_{r_{j+1}} - V^n_{r_{j-1}}\right) \quad , \tag{B-6}$$

and the final estimates are

$$V^{n+1}_{r_j} = V^n_{r_j} - \frac{\Delta t}{\bar{\rho}\, 2\Delta r}\,\left(P^*_{j+1} - P^*_{j-1}\right) \quad , \tag{B-7}$$

$$P^{n+1}_j = P^n_j - \frac{\Delta t}{2\Delta r}\,\overline{\Delta P}\,\left(V^*_{r_{j+1}} - V^*_{r_{j-1}}\right) . \tag{B-8}$$

From the substitution of (B-5) and (B-6) into (B-7) and (B-8), one obtains

$$V^{n+1}_{r_j} = v^n_{r_j} - \frac{\Delta t}{\bar{\rho}\, 2\Delta r}\left[ P^n_{j+1} - P^n_{j-1} - \frac{\Delta t\ \overline{\Delta P}}{2\Delta r}\left(v^n_{r_{j+2}} + v^n_{r_{j-2}} - 2v^n_{r_j}\right)\right] \tag{B-9}$$

$$P_j^{n+1} = P_j^n - \frac{\Delta t\ \overline{\Delta p}}{2\Delta r}\left[V_{r_{j+1}}^n - V_{r_{j-1}}^n - \frac{\Delta t}{\bar{\rho}\,2\Delta r}\,(P_{j+2}^n + P_{j-2}^n - 2P_j^n)\right]. \tag{B-10}$$

On the assumption of the harmonic solution $e^{ikr}$, where k is the wave number, the radial velocity and pressure dependence between adjacent gridpoints are

$$v_{r_{j+1}}^n = V_r^n\, e^{ik(j\Delta r)} \qquad p_{j+1}^n = p^n\, e^{ikj\Delta r} \tag{B-11}$$

$$v_{r_j}^n = V_r^n\, e^{ik(j-1)\Delta r} \qquad p_j^n = p^n\, e^{ik(j-1)\Delta r}$$

$$V_{r_{j-1}}^n = V_r^n\, e^{ik(j-2)\Delta r} \qquad p_{j-1}^n = p^n\, e^{ik(j-2)\Delta r}$$

In (B-11) $V_r^n$ and $p^n$ are the amplitudes. Upon substitution of the four identities,

$$V_{r_{j+1}}^n - v_{r_{j-1}}^n = V_r^n\ 2\,i\,\sin k\Delta r\ , \tag{B-12}$$

$$P_{j+1}^n - P_{j-1}^n = P^n\ 2i\sin k\Delta r\ , \tag{B-13}$$

$$V_{r_{j+2}}^n + v_{r_{j-2}}^n - 2v_{r_j}^n = V_r^n\,(2\cos k2\Delta r - 2)\ , \tag{B-14}$$

and

$$P_{j+2}^n + P_{j-2}^n - 2P_j^n = P^n(2\cos k2\Delta r - 2)\ , \tag{B-15}$$

(B-9) and (B-10) become

$$V_r^{n+1} = v_r^n - \frac{\Delta t}{\bar{\rho} 2\Delta r}\left[ P^n \, 2i\sin k\Delta r - \frac{\Delta t \, \overline{\Delta p}}{\Delta r} V_r^n(\cos k2\Delta r - 1)\right] , \tag{B-16}$$

$$P^{n+1} = P^n - \frac{\Delta t \, \overline{\Delta p}}{2\Delta r}\left[V_r^n \, 2i\sin k\Delta r - \frac{\Delta t}{\bar{\rho}\Delta r} P^n(\cos k2\Delta r - 1)\right]. \tag{B-17}$$

For notational simplicity, define

$$\gamma \equiv \frac{\Delta t}{\Delta r}(\cos k2\Delta r - 1) , \tag{B-18}$$

$$\alpha \equiv \frac{\Delta t}{\Delta r} \sin k\Delta r , \tag{B-19}$$

and

$$\omega \equiv \frac{\Delta t \, \overline{\Delta p}}{\bar{\rho} 2\Delta r} \gamma . \tag{B-20}$$

With these definitions and some rearrangement, (B-16) and (B-17) become

$$V_r^{n+1} = (1 + \omega) V_r^n - \frac{i\alpha}{\bar{\rho}} P^n , \tag{B-21}$$

$$P^{n+1} = -i\alpha \overline{\Delta P} \; V_r^n + (1 + \omega) P^n . \tag{B-22}$$

The amplification matrix, M, of this set of equations is

$$M = \begin{pmatrix} (1+\omega) & \frac{-i\alpha}{\beta} \\ -i\alpha\overline{\Delta p} & (1+\omega) \end{pmatrix} . \qquad \text{(B-23)}$$

The criterion for linear computational stability is that both eigenvalues of M be less than or equal to 1. The eigenvalues, $\lambda_1$, and $\lambda_2$, are found by solving

$$\det \begin{pmatrix} a-\lambda & b \\ c & a-\lambda \end{pmatrix} = 0 \quad , \qquad \text{(B-24)}$$

where

$$\begin{aligned} a &\equiv (1+\omega) \\ b &\equiv \frac{-i\alpha}{\beta} \\ c &\equiv -i\alpha\overline{\Delta p} \end{aligned} \quad . \qquad \text{(B-25)}$$

The eigenvalues are

$$\lambda = \tfrac{1}{2}\left[\, 2a \quad \pm\sqrt{4bc} \,\right] . \qquad \text{(B-26)}$$

Upon the substitution for a, b, and c, the eigenvalues become

$$\lambda = 1 + \omega \pm i\alpha\sqrt{\overline{\Delta p}/\beta} \, , \qquad \text{(B-27)}$$

where the magnitude of the eigenvalues are

$$|\lambda| = \left[(1+\omega)^2 + \alpha^2 \frac{\overline{\Delta p}}{\beta}\right]^{\frac{1}{2}} . \qquad \text{(B-28)}$$

From the trigonometric identities

$$\gamma = \frac{\Delta t}{\Delta r}\,(\cos k2\Delta r - 1)$$

$$\gamma = \frac{\Delta t}{\Delta r}\,(-2\sin^2 k\Delta r) \quad , \tag{B-29}$$

and the definition

$$\omega = -\left(\frac{\Delta t}{\Delta r}\right)^2 \frac{\overline{\Delta p}}{\bar{\rho}} \sin^2 k\Delta r = -\frac{\overline{\Delta p}}{\bar{\rho}}\,\alpha^2 \quad , \tag{B-30}$$

the magnitude of the eigenvalues is

$$|\lambda| = \left[1 + \omega + \omega^2\right] \quad . \tag{B-31}$$

Now $|\lambda| \leq 1$ provided

$$\omega \leq 0 \tag{B-32}$$

and

$$|\omega| \leq 1 \quad . \tag{B-33}$$

Because $\omega = -\left(\frac{\Delta t}{\Delta r}\right)^2 \sin^2 k\,\Delta t$, the condition of (B-32) is satisfied. The second condition, (B-33), is satisfied provided that

$$\left(\frac{\Delta t}{\Delta r}\right)^2 \frac{\overline{\Delta p}}{\bar{\rho}} \leq 1 \tag{B-34}$$

or

$$\frac{\Delta t}{\Delta r}\sqrt{\overline{\Delta p}/\bar{\rho}} \leq 1 \quad . \tag{B-35}$$

The inequality (B-35) must be satisfied to insure computational stability. This is the most stringent condition obtained from the linear analysis of the equations of the

isentropic model. The relationship of this condition to the speed of the external gravity wave is obtained through the hydrostatic equation

$$\frac{\overline{\Delta p}}{\overline{\rho}} = g H , \qquad \text{(B-36)}$$

where H is the mean depth of the model atmosphere.

# APPENDIX C - Infrared Radiative Cooling for a Tropical Atmosphere

## C1. INTRODUCTION

Because of the small magnitude of the diabatic cooling by the divergence of infrared radiation and the uncertanties in the heating and mixing parameterization in the isentropic model, the estimation of an infrared cooling profile with high resolution is not required. However, profiles of infrared cooling from several temperature and moisture distributions are presented to illustrate ranges of cooling for various tropical conditions and to justify the use of a mean cooling rate. The basic temperature and moisture distribution is Jordan's mean hurricane season sounding (1958), which will be considered representative of the nearly cloud-free region surrounding the storm.

## C2. COMPUTATIONAL PROCEDURE

In Sasamori's (1968) model the absorptivities for water vapor ($H_2O$), carbon dioxide ($CO_2$), and ozone ($O_3$) that are complicated functions of path length and temperature, are approximated by empirical formulas. However, in these experiments where only the troposphere is considered, the effect of ozone is neglected. Sasamori's (1968) model is now summarized to study profiles of cooling in the tropical atmosphere.

The net flux of radiation through a unit area is a function of the amount of absorbing gas above and below the layer, as well as the vertical temperature profile. The mean absorptivity, R, is

$$R(u,T) = \int_0^\infty \left[1 - \tau(u)\right] \frac{dB_\nu}{dT} \, d\nu \quad , \qquad (C-1)$$

where $B_\nu$ is Planck's radiation function, and T is temperature. The effective path length, u, is approximately

$$u \approx g^{-1} \int_{p_1}^{p_2} q \, \frac{P}{P_o} \, dp \qquad (C-2)$$

with q the mixing ratio and $p_o$ equal to 1000 mb.

At any level, z, the downward and upward fluxes are

$$F\downarrow (z) = \int_{T_o}^{T(z)} R\left\{ u(T') - u\left[T(z')\right] , T'\right\} dT' \qquad (C-3)$$

and

$$F\uparrow (z) = \sigma T_o^{\,4} + \int_{T_o}^{T(z)} R\left\{ u\left[T(z)\right] - u(T'), T'\right\} dT' \qquad (C-4)$$

with $\sigma$ equal to Stefan's constant ($8.13 \times 10^{-11}$ cal $cm^{-2}$ $K^{-4}$ $min^{-1}$), $T_o$ the surface temperature, and T' the variable of integration corresponding to temperature.

The radiative temperature change calculated from the net vertical flux divergence is

$$\frac{\partial T}{\partial t_R} = -\frac{1}{\rho C_p} \frac{\partial (F\uparrow - F\downarrow)}{\partial z} \quad .$$

Sasamori transforms R(u,T) to a normalized absorptivity given by

$$\bar{A}(u,T) = \frac{R(u,T)}{4\sigma T^3} = \frac{\int_0^\infty [1 - \gamma(u)] \frac{dB_\nu}{dT} d\nu}{\int_0^\infty \frac{dB_\nu}{dT} d\nu} . \qquad \text{(C-6)}$$

With this transformation, the downward and upward fluxes are

$$F\downarrow(z) = 4\sigma \int_0^{T(z)} \bar{A}\left\{u(T') - u(T(z)),\ T'\right\} T'^3\, dT' , \qquad \text{(C-7)}$$

$$F\uparrow(z) = \sigma T_0^4 + 4\sigma \int_0^{T(z)} \bar{A}\left\{u\left[T(z)\right] - u(T'),\ T'\right\} T'^3\, dT' . \qquad \text{(C-8)}$$

Sasamori notes that the mean absorptivity is nearly constant with temperature in the range +30 to -50°C, but decreases with decreasing temperature at extremely low temperatures. For this reason, the integrals in (C-7) and (C-8) are separated into two parts. For example, (C-7) is written

$$F\downarrow(z) = 4\sigma \int_{T_{z_1}}^{T_z} \bar{A}\left\{u(T') - u\left[T(z)\right],\ T'\right\} T'^3\, dT' \qquad \text{(C-9)}$$
$$+ 4\sigma \int_0^{T_{z_1}} \bar{A}\left\{u\left[T(z_1)\right] - u\left[T(z)\right],\ T'\right\} T'^3\, dT' ,$$

where $z_1$ is the height of the level above which the path length changes very little. Disregarding the direct dependency of A(u,T') on T' in the first integral and taking $u(T_{z1}) - u(T_z)$ constant with T' (by definition of $z_1$) in the second integral, (C-9) becomes

$$F\downarrow(z) = 4\sigma \int_{T_{z_1}}^{T_z} \bar{A}_o \left\{ u(T') - u\left[T(z)\right] \right\} T'^3 \, dT' \qquad \text{(C-10)}$$

$$+ \sigma T_{z_1}^4 \bar{A} \left\{ u\left[T(z_1)\right] - u\left[T(z)\right], T(z_1) \right\} .$$

$\bar{A}_o$ (u) is the average absorption for the temperature range +30 to -50°C and $\bar{A}$ (u,T) is the mean absorptivity which varies with temperature. $\bar{A}_o$ (u) and $\bar{A}$(u,T), approximated by empirical formulas, are

$$\bar{A}_o(u) = \begin{cases} 0.846(\Delta u + 3.59 \times 10^{-5})^{0.243} - .069 & \Delta u < 0.01 \text{ gm} \\ 0.240 \log_{10}(\Delta u + 0.01) + 0.622 & 0.01 \text{ gm} < \Delta u \end{cases} \qquad \text{(C-11)}$$

$$\bar{A}(u,T) = 8.34\, T^{\left[0.353 \log_{10} u - 0.44\right]} \times u^{\left[-0.03455 \log_{10} u - 0.705\right]} \qquad \text{(C-12)}$$

## C3. EXPERIMENTAL RESULTS

Height coordinates with 21 levels are utilized to provide high resolution ($\Delta z$ = 1 km) for investigating the effects of different moisture distributions. In experiments with a resolution of 2 km the mean cooling profiles are virtually unchanged. Thus, the vertical resolution needed to describe the essential features of cooling in a clear atmosphere is considerably less than 1 km. The vertical integrals are evaluated by the trapezoidal rule and $z_1$ is assumed to be 20 km.

Figure C1 shows the upward, downward, and net fluxes from

Jordan's mean hurricane sounding and the corresponding cooling rates caused by water vapor and carbon dioxide. The cooling effect from $CO_2$ is negligible compared to that from $H_2O$. A nearly constant cooling rate of $2^{\circ}C$ per day occurs from the surface to 10 km. From 10 km to the tropopause the cooling rate decreases, reaching a minimum of $0.1^{\circ}$ per day near 16 km. Large cooling rates occur above the tropopause.

The next series of experiments is designed to investigate the dependency of the infrared cooling rates on the moisture distribution. The first two comparisons show the effect of nearly saturated layer, one close to the surface and the other high in the troposphere. Figure C2 shows the cooling profile that results from a 95 percent relative humidity in the layer from the surface to 3 km and another profile which results from a 95 percent relative humidity in the layer between 10 and 14 km. For the other layers the temperature and moisture distributions are those of the mean hurricane sounding. Cooling is slightly increased above and decreased below the moist layers. Figure C3 shows the cooling rates that result from the mean hurricane season temperature sounding and two relative humidity profiles of 70 and 10 percent. Differences are again small with slightly lower cooling rates occurring in the drier air.

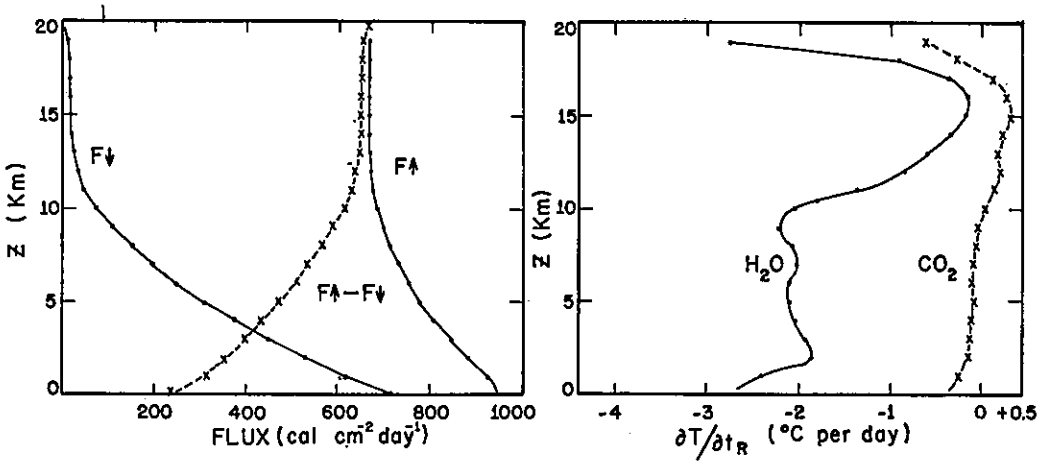


Figure C-1. (a) Upward, downward, and net infrared flux for mean tropical sounding, (b) Rates of temperature change due to infrared flux divergence

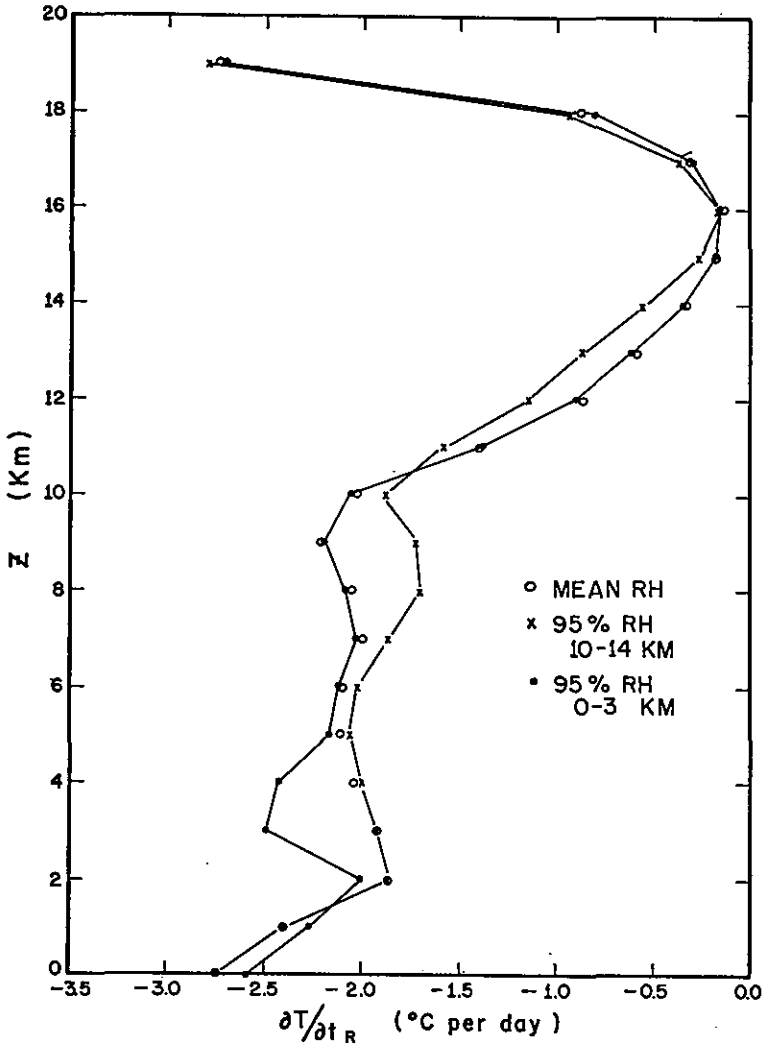


Figure C-2. Temperature change rates for various relative humidity distributions in tropics

The relatively small dependency of the cooling rate on the moisture distributions justifies using the mean cooling rate in the hurricane model. Because the temperature in the hurricane environment is slowly varying, it is permissible to use the same cooling rate for several hours in numerical models of hurricanes. By such an approximation, the added storage and computational time are negligible. In this hurricane radiation experiment, the representative mean cooling profile (fig. C4) is nearly constant at 2°C per day below 400 mb and decreases to 0°C per day from 400 to 135 mb. It should be noted that the effect of clouds on infrared cooling is large, hence this rate is valid only in the cloud-free region of the hurricane environment.

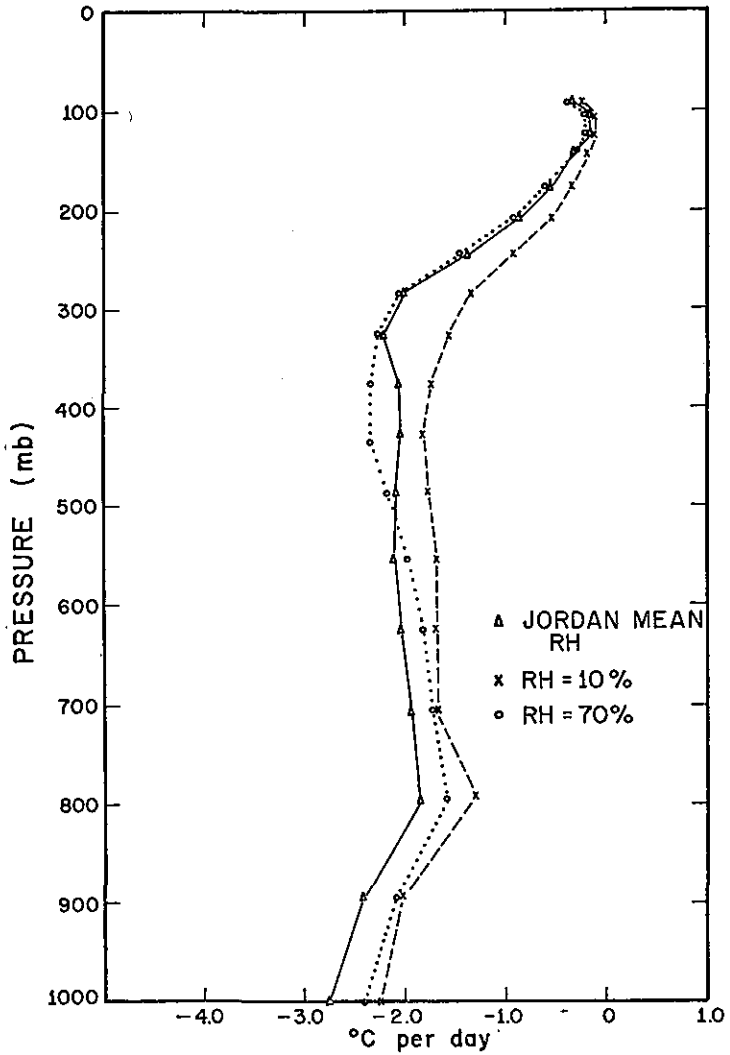


Figure C-3. Rates of temperature change for various relative humidity distributions in tropics

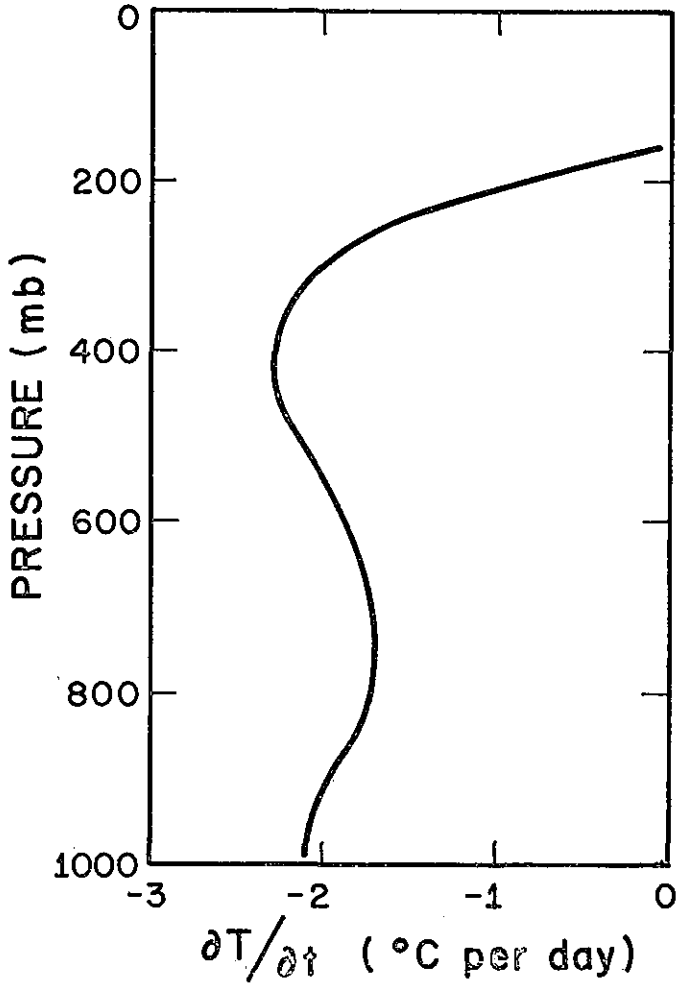


Figure C-4. Rate of temperature change due to infrared flux divergence used in hurricane cooling Experiment 13

## REFERENCES


Anthes, R. A. (1969). Numerical experiments on ring convection and effect of variable resolution on cellular convection. Technical Memorandum ERLTM-NHRL 86. (ESSA, 18 pp.).

Anthes, R. A. (1970). The role of large-scale asymmetries and internal mixing in computing meridional circulations associated with the steady-state hurricane, Mon. Wea. Rev., 1970. (To be published).

Anthes, R. A. and D. R. Johnson (1968). Generation of available potential energy in Hurricane Hilda (1968). Mon. Wea. Rev., 96, 291-302.

Barrientos, C. S. (1964). Computations of transverse circulation in a steady-state, symmetric hurricane. J. Appl. Meteorol., 3, 685-692.

Bullock, B. R. and D. R. Johnson (1969). The generation of available potential energy by latent heat release in a mid-latitude cyclone. Annual Report, ESSA Grant E-8-69 (G), Department of Meteorology, University of Wisconsin, Madison, Wisconsin.

Charney, J. G. (1963). A note on large-scale motions in the tropics. J. Atmos. Sci., 26, 607-609.

Charney, J. G. and A. Eliassen (1964). On the growth of the hurricane depression. J. Atmos. Sci., 21, 68-75.

Cline, I. M. (1926). Tropical Cyclones, New York, The Macmillan Company, 301 pp.

Colón, J. A. (1963). On the evolution of the wind field during the life cycle of tropical cyclones, National Hurricane Research Project Report No. 65, U.S. Weather Bureau, 36 pp.

Dutton, J. and D. R. Johnson, (1967). The theory of available potential energy and a variational approach to atmospheric energetics. Advances in Geophysics, 12, 333-436.

Eliassen, A. and E. Raustein (1968). A numerical integration experiment with a model atmosphere based on isentropic surfaces. Meteorologiske Annaler, Bd. 5, No. 2, 45-63.

Estoque, M. and J. Partagas (1968). Hurricane studies: part II, Institute of Atmospheric Science, Paper No. 2, University of Miami, Coral Gables, Florida, 28-65.

Gall, R. L. and D. R. Johnson (1969). The generation of available potential energy by sensible heating: a case study. Annual Report, ESSA Grant E-8-69(G), Department of Meteorology, University of Wisconsin, Madison, Wisconsin.

Gentry, R. C. (1964). A study of hurricane rainbands. National Hurricane Research Project Report No. 69, U.S. Weather Bureau, Miami, Florida, 85 pp.

Gray, W. M. (1967). The mutual variation of wind, shear and baroclinicity in the cumulus convective atmosphere of the hurricane, Mon. Wea. Rev., 95, 55-73.

Haque, S. M. A. (1952). The initiation of cyclonic circulation in a vertically unstable stagnant air mass, Quart. Jour. Roy. Meteorol. Soc., 78, 394-406.

Hawkins, H. F. and D. T. Rubsam (1968). Hurricane Hilda, 1964; II. Structure and budgets of the hurricane on October 1, 1964. Mon. Wea. Rev., 96, 617-636.

Hughes, L. A. (1952). On the low level wind structure of tropical storms, J. Meteorol., 9, 422-428.

Johnson, D. R. (1969). The available potential energy of storms, Annual Report, ESSA Grant E-8-69(G), Department of Meteorology, University of Wisconsin, Madison, Wisconsin.

Johnson, D. R. and J. Dutton (1970). (Unpublished manuscript).

Jordan, C. L. (1958). Mean soundings for the West Indies area. J. Meteorol., 15, 91-97.

Kasahara, A. (1961). A numerical experiment on the development of a tropical cyclone, J. Meteorol., 18, 259-282.

Krishnamurti, T. N. (1961). On the vertical velocity field in a steady symmetric hurricane. Tellus, 13, 171-180.

Krishnamurti, T. N. (1962). Some numerical calculations of the vertical velocity field in hurricanes. Tellus, 14, 195-211.

Kuo, H. L. (1959). Dynamics of convective vortices and eye formation, The Atmosphere and the Sea in Motion. (New York, Rockefeller Institute Press and London, Oxford University Press, 413-424).

Kuo, H. L. (1961). Convection in a conditionally unstable atmosphere. Tellus, 13, 441-59.

Kuo, H. L. (1965). On the formation and intensification of tropical cyclones through latent heat release by cumulus convection. J. Atmos. Sci., 22, 40-63.

Lilly , D. K. (1960). On the theory of disturbances in a conditionally unstable atmosphere, Mon. Wea. Rev., 88, 1-17.

Lorenz, E. (1955). Available potential energy and the maintenance of the general circulation. Tellus, 7, 157-167.

Malkus, J. S. and H. Riehl (1960). On the dynamics and energy transformations in steady-state hurricanes. Tellus, 12, 1-20.

Margules, M. (1903). Uber die Energie der Stürme, Jahrb. Zentr. Aust. Meteorol. 1-26. (translation by C. Abbe (1910) in Smithsonian Inst. Misc. Coll., 51, 553-595.

Matsuno, T., (1966). Numerical integrations of the primitive equations by a simulated backward difference method. J. Meteorol. Soc. Japan, 44, 76-84.

Miller, B. I. (1958). On the maximum intensity of hurricanes. J. Meteorol, 15, 184-195.

Miller, B. I. (1962). On the momentum and energy balance of Hurricane Helene (1958), National Hurricane Research Project Report No. 53, U.S. Weather Bureau, Miami, Florida, 19 pp.

Miller, B. I. (1964). A study of the filling of hurricane Donna (1960) over land. Mon. Wea. Rev., 92, 389-406.

Molenkamp, C. R. (1968). Accuracy of finite difference methods applied to the advection equation, J. Appl. Meteorol. 7, 160-167.

Ogura, Y. (1963). The evolution of a moist convective element in a shallow conditionally unstable atmosphere: a numerical calculation. J. Atmos. Sci., 20, 407-424.

Ogura, Y. (1964). Frictionally controlled, thermally driven circulations in a circular vortex with applications to tropical cyclones. J. Atmos. Sci., 21, 610-621.

Ooyama, K. (1969). Numerical simulation of the life cycle of tropical cyclones. J. Atmos. Sci., 26, 3-40.

Palmén, E. (1948). On the formation and structure of tropical hurricanes. Geophysica, (Helsinki), 3, 26-38.

Palmén, E. and C. Jordan (1955). Note on the release of kinetic energy in tropical cyclones. Tellus, 7, 186-188.

Palmén, E. and H. Riehl (1957). Budget of angular momentum and kinetic energy in tropical cyclones. J. Meteorol., 14, 150-159.

Phillips, N. A. (1959). An example of non-linear computational instability, The Atmosphere and the Sea in Motion. (New York, Rockefeller Institute Press and London, Oxford University Press, 501-504).

Redfield, W. C. (1831). Remarks on the prevailing storms of the Atlantic coast of the North American States. American Journal of Science, 20, 17-51.

Reid, W. (1841). The Law of Storms, (London, John Weale, Library of Civil, Military, and Mechanical Engineering, 59, High Holborn, 556 pp.).

Riehl, H. and J. S. Malkus (1958). On the heat balance of the equatorial trough zone. Geophysica, 6, 503-538.

Riehl, H. and J. S. Malkus (1961). Some aspects of hurricane Daisy, 1958. Tellus, 13, 181-213.

Rosenthal, S. L. (1964). Some attempts to simulate the development of tropical cyclones by numerical methods. Mon. Wea. Rev., 92, 1-21.

Rosenthal, S. L. (1969). Numerical experiments with a multi-level primitive equation model designed to simulate the development of tropical cyclones: Experiment 1. Technical Memorandum ERLTM-NHRL 82, U.S. Department of Commerce, ESSA, Miami, Florida, (Unpublished report), 33 pp.

Rosenthal, S. L. and W. J. Koss (1968). Linear analysis of a tropical cyclone model with increased vertical resolution, Mon. Wea. Rev., 96, 858-865.

Sasamori, T. (1968). The radiative cooling calculation for application to general circulation experiments. J. Appl. Meteorol., 7, 721-729.

Smith, P. J. and L. H. Horn (1969). A computational study of the energetics of a limited region of the atmosphere. Tellus, 21, 193-201.

Smagorinsky, J., S. Manabe and L. Holloway (1965). Numerical results from a nine-level general circulation model of the atmosphere. Mon. Wea. Rev., 93, 727-768.

Stormfury (1969). Project STORMFURY, Annual Report 1968, ESSA, National Hurricane Research Laboratory, Miami, Florida, 40 pp.

Syōno, S. (1950). On the vortical rain. Geophys. Notes, Tokyo University, 3, No. 25, 3 pp.

Syōno, S. (1951). On the structure of atmospheric vortices. J. Meteorol., 8, 103-110.

Syōno, S. (1962). A numerical experiment of the formation of tropical cyclones. Proc. Int. Symp. on Num. Wea. Pred., Tokyo, 405-418.

Yamasaki, M. (1968a). Numerical simulation of tropical cyclone development with the use of primitive equations. J. Meteorol. Soc. Japan, 46, 178-201.

Yamasaki, M. (1968b). A tropical cyclone model with parameterized vertical partition of released latent heat. J. Meteorol. Soc. Japan, 46, 202-214.

Yanai, M. (1964). Formation of tropical cyclones. Rev. Geophys., 2, 367-414.



GPO 857-997